CZECH TECHNICAL UNIVERSITY IN PRAGUE

Faculty of Nuclear Sciences and Physical Engineering

Department of Physics

Bachelor thesis

Signal extraction in J/ψ photoproduction in the ALICE experiment

Tomáš Herman

Supervisor: doc. Jesús Guillermo Contreras Nuño, Ph.D.

Prague, 2017

ČESKÉ VYSOKÉ UČENÍ TECHNICKÉ
V PRAZE
Fakulta jaderná a fyzikálně inženýrská
Katedra fyziky

Bakalářská práce

Extrakce signálu z fotoprodukce mesonu J/ψ v experimentu ALICE

Tomáš Herman

Vedoucí práce: doc. Jesús Guillermo Contreras Nuño, Ph.D.

Praha, 2017

ČESKÉ VYSOKÉ UČENÍ TECHNICKÉ V PRAZE
FAKULTA JADERNÁ A FYZIKÁLNĚ INŽENÝRSKÁ
PRAHA 1 - STARÉ MĚSTO, BŘEHOVÁ 7 - PSČ 115 19

Katedra: fyziky *Akademický rok:* 2016/2017

ZADÁNÍ BAKALÁŘSKÉ PRÁCE

Student: Tomáš Herman

Studijní program: Aplikace přírodních věd

Obor: Experimentální jaderná a částicová fyzika

Název práce: (česky) Extrakce signálu z fotoprodukce mesonu J/Psi v experimentu ALICE

Název práce: (anglicky) Signal extraction in J/Psi photoproduction in the ALICE experiment

Pokyny pro vypracování:

1. Zpracujte rešerši těchto témat:
   a) QCD, saturace a stínění
   b) Experimenty LHC a ALICE
   c) J/Psi fotoprodukce v experimentu ALICE
2. Namodelujte distribuce invariantní hmotnosti mesonu J/Psi.

Doporučená literatura:

[1] J. G. Contreras, J. D. Tapia Takaki: Ultra-peripheral heavy-ion collisions at the LHC, Int. J. Mod. Phys. A 30, 1542012 (2015)

[2] N. Armesto: Nuclear shadowing, J. Phys. G 32, R367-R394 (2006)

[3] G. D. Coughlan, J. E. Dodd, B. M. Gripaios: The Ideas of Particle Physics: An Introduction for Scientists, Cambridge University Press, 2006

Jméno a pracoviště vedoucího bakalářské práce:

doc. Jesús Guillermo Contreras Nuño, Ph.D., Katedra fyziky, Fakuklta jaderná a fyzikálně inženýrská, ČVUT v Praze

Datum zadání bakalářské práce: 20.10.2016

Termín odevzdání bakalářské práce: 10.07.2017

Doba platnosti zadání je dva roky od data zadání.

VZ

vedoucí katedry ČESKÉ VYSOKÉ UČENÍ TECHNICKÉ V PRAZE Fakulta jaderná a fyzikálně inženýrská -1- *děkan*

V Praze dne 20.10.2016

Prohlášení:

Prohlašuji, že jsem svou bakalářskou práci vypracoval samostatně a použil jsem pouze podklady (literaturu, software, atd.) uvedené v přiloženém seznamu.

Nemám závažný důvod proti použití tohoto školního díla ve smyslu § 60 Zákona č.121/2000 Sb., o právu autorském, o právech souvisejících s právem autorským a o změně některých zákonů (autorský zákon).

V Praze dne ....

Tomáš Herman

Acknowledgments

I would like to express my gratitude to my supervisor doc. Jesús Guillermo Contreras Nuño, Ph.D. for his guidance, for his patience, valuable advice and constructive comments, for his countless explanations and language corrections. I would also like to thank my friends who supported me both personally and provided valuable advice for my work. A special thanks goes to my dear parents, my beloved girlfriend Pavlínka and my entire family for their undying support.

Title:
Signal extraction in J/ψ photoproduction in the ALICE experiment

Author: Tomáš Herman

Specialization: Experimental Physics and Particle Physics

Sort of project: Bachelor thesis

Supervisor: doc. Jesús Guillermo Contreras Nuño, Ph.D., Department of Physics, Faculty of Nuclear Sciences and Physical Engineering, Czech Technical University in Prague

Consultant: ———

Abstract: The behavior of the gluon distribution functions in protons and nuclei at low Bjorken x can be studied with ALICE at the LHC using exclusive photoproduction of J/ψ. When the J/ψs are measured in the dilepton decay channel, the yield is extracted by modeling the invariant mass distribution of the decay products. The most frequently used model is called Crystal Ball. Recently, a new model, called GuassExp, has been proposed. This model is allegedly better suited for analysis of high energetic peaks with radiation tails. Performance of these two models is tested on both Monte Carlo and real data, to establish which one of them is superior. The analyzed data are from Pb-Pb ultra-peripheral collisions at $\sqrt{s_{NN}} = 5.02$ TeV measured with the ALICE muon spectrometer. Signal extraction is one of the largest contributors to the total systematic uncertainty of the photoproduction measurement. The hope is that the new model may help in reducing the systematic uncertainty from signal extraction.

Key words: ultra-peripheral collisions, J/ψ, signal extraction, Crystal Ball, GaussExp

Název práce:
Extrakce signálu z fotoprodukce mesonu J/ψ v experimentu ALICE

Autor: Tomáš Herman

Obor: Experimentální jaderná a částicová fyzika

Druh práce: Bakalářská práce

Vedoucí práce: doc. Jesús Guillermo Contreras Nuño, Ph.D., Katedra fyziky, Fakulta jaderná a fyzikálně inženýrská, České vysoké učení technické v Praze

Konzultant: ———

Abstrakt: Chování gluonových distribučních funkcí v protonech a jádrech při malém Bjorkenově x může být studováno v rámci ALICE v LHC za využití exkluzivní fotoprodukce J/ψ. Když jsou J/ψ měřena v dileptonovém rozpadovém kanále, je jejich výtěžek extrahován pomocí modelování spektra invariantní hmotnosti rozpadových produktů. Nejčastěji používaný model se nazývá Crystal Ball. Nedávno byl ale navržen nový model jménem GaussExp, který je údajně vhodnější pro analýzu vysokoenergetických signálů deformovaných radiačními efekty. Výkon obou modelů je testován jak na Monte Carlo tak na skutečných datech, aby bylo určeno, který z nich je kvalitnější. Analyzovaná data jsou z Pb-Pb ultra-periferálních srážek při energii $\sqrt{s_{NN}} = 5.02$ TeV změřených pomocí mionového spektrometru na ALICE. Extrakce signálu je jedním z hlavních příspěvků do celkové systematické nejistoty při měření fotoprodukce. Naděje je, že by tento nový model mohl dopomoci ke snížení systematické nejistoty z extrakce signálu.

Klíčová slova: ultra-periferální srážky, J/ψ, extrakce signálu, Crystal Ball, GaussExp

Contents

List of Figures

List of Tables

Preface

The modern research in particle physics has lead us to places beyond imagination, nevertheless we are able to describe them with quantum chromodynamics (QCD). Quantum chromodynamics is a theory describing the behavior of quarks and gluons, building blocks of protons and neutrons. The structure of a proton can be described by parton (quark or gluon) distribution functions (PDFs). Parton distribution functions can be in leading order interpreted as the number of the given parton in the proton. Under standard conditions a proton is made out of two up quarks and one down quark. However, in the region of low Bjorken x proton is predominantly made out of gluons. With decreasing x the number of gluons is rising. This can be interpreted as the ability to distinguish fast quantum subprocesses involving splitting of gluons. But the number of gluons cannot rise indefinitely. At some point they will recombine and split at the same rate. This phenomenon is called gluon saturation and it is not fully understood. All the above concepts are described in Chapter 1 and Chapter 2.

In Chapter 3 ultra-peripheral collisions (UPC), a powerful tool to explore the gluon saturation, are discussed. Ultra-peripheral collisions are events where the two colliding particles are so far from each other that the hadronic interaction is suppressed to minimum and they interact only via virtual photons.

The ALICE experiment at the CERN LHC is described in Chapter 4, because it allow us to measure photoproduction in UPC for energies never reached before. This thesis in particular is focused on J/ψ meson photoproduction in the forward-rapidity region.

Two papers from previous research on ultra-peripheral collisions are presented in Chapter 5. A crucial part of the photoproduction analysis is signal extraction from the invariant mass distribution. However, the signal extraction is also a major contributor to the total systematic uncertainty of the measurement.

The most commonly used function for signal extraction is called Crystal Ball. Recently, a new model, called GuassExp, has been proposed. This model is allegedly better suited for describing high energetic peaks with radiation tails. The performance of both models has been tested on Monte Carlo and real data. Results of this comparison are presented in Chapter 6.

Chapter 1

Introduction to particle physics

1.1 The Standard Model

The Standard Model is a unification of theories which currently provides the best description of matter and forces in our universe. The approach that is used is to look at our world as if it were composed of fields. Each type of interaction has its own associated field and particles are only quanta of these fields, or merely excitations of these field, therefore can be described by wave functions. We can categorize these particles in many ways by different criteria. One way of doing this, is to divide them into two groups by their spin.

1.1.1 Bosons

Bosons are particles with integer spin. The elementary bosons are photons, $W^{\pm}$ and Z bosons, gluons, Higgs boson and the hypothetical graviton.

These particles are associated with the four forces in the universe. Photon is the force carrier particle of the electromagnetic field, which describes the behavior of electrically charged objects. The weak force, which is responsible for the decay of many unstable particles, is mediated by the $W^{\pm}$ and Z bosons. Gluons transfer the strong force, which governs the processes involving quarks and gluons themselves. If discovered the graviton will be the force carrier particle of the gravitational field, which attracts all bodies with energy. And last, but definitely not least, is the Higgs boson which is the mediator of the Higgs field responsible for the rest mass of all elementary particles in the Standard Model. All of these forces are different, but all are equally important as the world as we know it would not exist without them.

Electromagnetic force

As mentioned above the electromagnetic force affects all electrically charged particles, it has infinite range and the relative strength given by its coupling constant (discussed in Sec. 2.2) for low-energy interactions is $\alpha_{\mathrm{em}} = \frac{1}{137}$. The electromagnetic force is responsible, inter alia, for all chemical bonds and processes, for binding electrons in atomic nuclei and when we touch something we feel the electrons in our hand to repel from the electrons in the object we touch.

Strong force

The strong force has limited range up to distances around 10^{-15} m, its relative strength for low-energy interactions is $\alpha_{\mathrm{s}} \approx 1$ and as mentioned above it affects all quarks and gluons, which are particles with color charge (discussed in Sec. 2.1). The strong force is responsible for the fact that positively charged protons hold together in nuclei and do not fly apart due to the electromagnetic repulsion. This shows that the strong force is stronger than the electromagnetic force, hence the name strong. It is also responsible for the fact that protons and neutrons, which are composed of quarks, hold together, this will be further discussed later in Chapter 2.

Weak force

The weak force has also limited range to distances around 10^{-17} m and its relative strength for low-energy interactions is around $\alpha_{\mathrm{w}} \approx 10^{-7}$, therefore the name weak. The weak force affects all particles with weak charge and as mentioned above it is responsible for many types of decays. It is the only force which enables not conserving certain quantum numbers and it is the only force which violates certain symmetries. These properties make it very unique in this sense.

Gravitational force

The gravitational force has infinite range and relative strength for low-energy interactions $\alpha_{\mathrm{G}} \approx 10^{-39}$, making it the weakest of the elementary forces. It affects all particles with mass and even though we do not feel the gravitational attraction between us and other similarly sized objects, the gravitational force is what holds us on our planet Earth and it also governs the movement of stellar objects in our universe.

However, the Standard Model does not describe the gravitational force. Quantum theory of gravity, describing the behavior of gravitational force at very small scales, is one of the biggest challenges of current physics. But thankfully the gravitational force is very weak, when compared to other forces, therefore its effect can be neglected for particle experiments.

Unification of forces

The trend in modern physics is to find elegant and simple equations which would explain everything that we can observe. The unification of forces started in the eighteenth century when scientists realized that the electric and magnetic force are different manifestations of the same electromagnetic force. In the twentieth century it was proven that electromagnetic and weak force were also connected to one force, called electroweak. The electroweak force and the strong force are the main components of the Standard Model, which is currently the best attempt for the elegant and simple equation describing everything. However it is obvious that is just an attempt because the Standard Model is far from explaining all the effects we can observe around us.

1.1.2 Fermions

Fermions are particles with half integer spin. The elementary fermions, which with the technology at hand seem point like to us, are quarks and leptons. Quarks, leptons and their antiparticles compose all the variety of matter and antimatter particles known to us.

Leptons

There is a total of six leptons. With negative electric charge there are electron, muon, tau and corresponding to them without any electric charge are electron neutrino, muon neutrino and tau neutrino. Because neutrinos do not carry electric charge they do not interact through the electromagnetic force, they interact only via the weak force. For this reason and their very low rest mass, they almost do not interact with other matter which makes them very hard to detect.

Quarks

There is a total of six quarks, they are named up, down, charm, strange, top and bottom. Quarks interact through all four fundamental forces. More on quarks and their behavior in Chapter 2.

All of the elementary particles (except graviton) with their basic properties (mass, charge and spin) can be seen in Fig. 1.1.

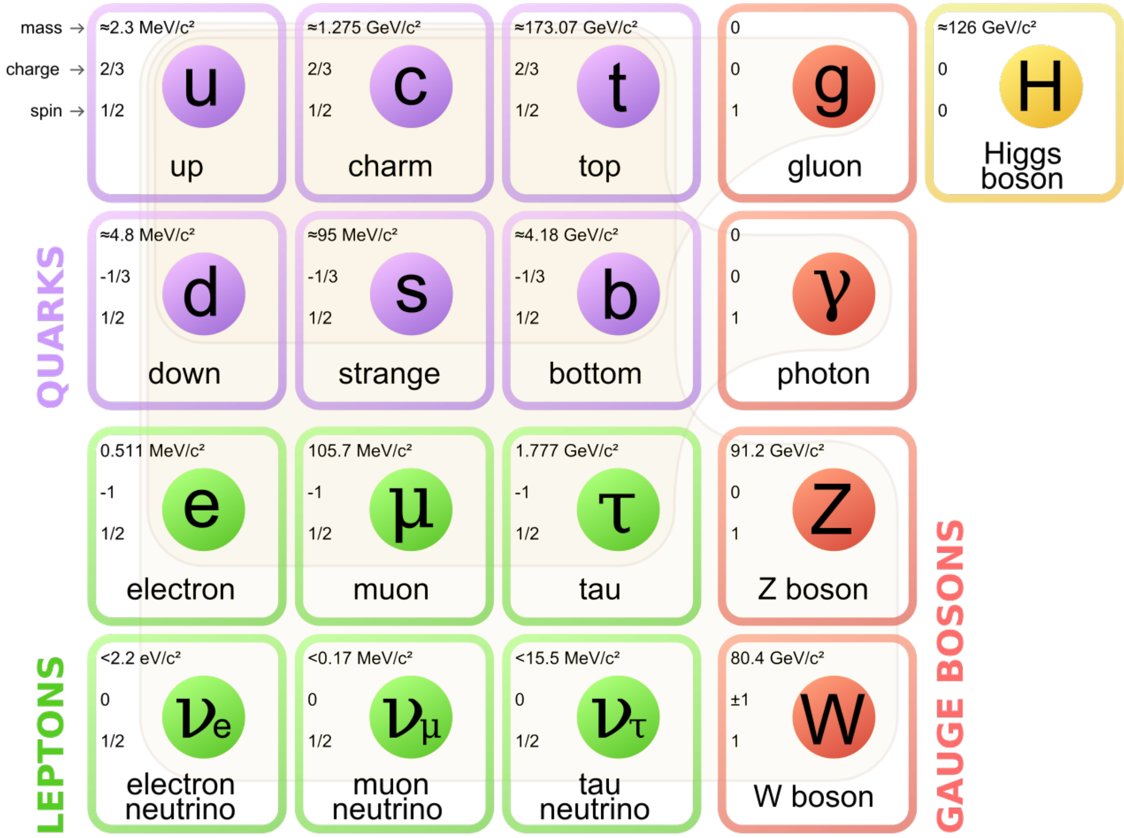

Figure 1.1: Summary of elementary particles and their basic properties [1].

1.1.3 Hadrons

Hadrons are particles composed of quarks. They are divided into two main groups, called Mesons and Baryons, by the amount of quarks they contain.

Mesons

Mesons are composite particles made of a quark-antiquark pair. This means they have integer spin, therefore they are bosons. One of the mesons is J/ψ ($c\bar{c}$) which is important for this thesis.

J/ψ meson

J/ψ is a particle composed of charm quark and antiquark pair, therefore it is its own antiparticle. It is the second lightest charmonium with rest mass $m = (3096.916 \pm 0.011)$ MeV [2]. It has spin 1 and parity -1 ($J^{PC} = 1^{--}$) therefore it is a vector meson. It has electric charge 0 and full width at half maximum $\Gamma = (92.9 \pm 2.8)$ keV [2].

When considering Heisenberg's uncertainty principle, this gives an approximate mean lifetime $\tau \approx 7 \cdot 10^{-21}$ s. This lifetime is several orders higher than would be expected for a particle that can decay via the strong force. This is due to the fact, that the lightest pair of mesons the J/ψ could decay into via the strong force are D mesons and the rest mass of two D mesons is higher than the rest mass of J/ψ. Therefore the charm quarks have to first decay into another type of quarks via the weak force and only after that the J/ψ can decay via the strong force. The main decay channels are as mentioned earlier hadronic with (87.7 ± 0.5) % [2] probability and the rest are leptonic, mainly $e^+ + e^-$ and $\mu^+ + \mu^-$, with probabilities (5.97 ± 0.3) % and (5.96 ± 0.3) % [2] respectively.

Baryons

Baryons are composite particles made of three quarks. This means they have half-integer spin, therefore they are fermions. Most common baryons are protons (uud) and neutrons (udd).

1.1.4 Antiparticles

For all the particles that were discussed in the sections above exist their corresponding antiparticles. Antiparticles have the same rest mass as their counterpart but they have opposite charge. Some particles are their own antiparticles, e.g. photons or mesons composed of the same quark and antiquark.

Nowadays we observe that the vast majority of the universe is composed of matter (including us). But current theories suggest that when matter formed from the energy of the Big Bang, our universe contained equal amount of matter and antimatter. Thus a process which disrupted this symmetry must have occurred. Such process is unknown to us and is currently one of the great research areas in modern physics.

1.1.5 Virtual particles

Virtual particles have several important properties which differentiate them from classic particles. They exist as fluctuations due to Heisenberg's uncertainty principle:

$$\Delta E \Delta t \geq \frac{\hbar}{2}. \tag{1.1}$$

They can be created from vacuum by "borrowing" energy ΔE, equivalent to their rest mass, for time Δt. They can exist only for this time, which means that the heavier the particle is the shorter time it exists. But over all, virtual particles are very short-lived. Because they live only for a short time, they have effect only on very short distances, they can travel, at maximum, the distance light would travel in the time for which they exist.

Due to the conservation laws virtual particles are very often created in virtual particle-antiparticle pairs. All virtual particles obey conversation laws such as conservation of energy or conservation of momentum. But they do not obey the energy-momentum relation

$$E^2 = p^2c^2 + m_0^2c^4, \tag{1.2}$$

where E is the total energy of a particle, p is its momentum, m_0 is its rest mass and c is the speed of light in vacuum. This property is described as being off mass shell, opposite to traditional particles which obey the equation Eq. 1.2 and therefore are on mass shell.

Except for arising from vacuum virtual particles are also used when describing effects of a force. An interaction between two particles can be described by the exchange of virtual bosons, more precisely the fore carrier bosons which where discussed earlier in Sec. 1.1.1.

Chapter 2

Quantum chromodynamics

Quantum chromodynamics (QCD) is a non-abelian gauge theory with a symmetry group SU(3). It is a quantum field theory but for the purpose of this thesis it will be described through its properties and experimental results without going too deeply into the mathematical background.

2.1 Color charge

As we already know the strong force is mediated by gluons and affects particles with color charge. In QCD, which is the theory describing interactions via the strong force, a new quantum number is introduced. The are several reasons for this new quantum number. One of them is the existence of particles composed of three identical quarks, for instance Δ^{++} (uuu) composed of three up quarks or Ω^{-} (sss), composed of three strange quarks. These particles contain three identical fermions (quarks) with the same spin, but that is in strict conflict with Pauli's exclusion principle, therefore the need for a quantum number that could differentiate them arises. Another reason is that with the use of this new quantum number other aspects of the strong force can be illustrated.

This quantum number can be interpreted as a new type of charge that has three values. These values are called red, green and blue, therefore the charge is called color charge. Quarks have assigned colors and antiquarks have assigned corresponding anticolors. When quarks interact with each other, they do so by the exchange of gluons. This interaction causes the quarks to change color which is explained as gluons having one color and one anticolor. This allows combinations of three colors and three anticolors. Because of symmetry principles in QCD the resulting combinations create an octet of gluons, which change color, and a singlet, which does not.

When measuring the composite quark particles (hadrons), we observe only those with certain net color, which is called neutral. Here a nice analogy with the colors of light comes at hand. Combining color with its anticolor yields darkness (black), which is color neutral, and combining the three colors (red, green, blue) yields white light, which is also color neutral. As was mentioned earlier, and as could be deduced from the explanation above, the two most common ways of how neutral net color is achieved are composition of mesons, composed of a quark with color and antiquark with the corresponding anticolor, and baryons which are composed of three quarks with all three colors. It turns out that this rule applies universally and therefore a single quark, which always has some net color, cannot exist on its own. This phenomenon is called color confinement and it can be observed when examining the behavior of the strong force at different distances.

2.2 Coupling constant

Let us consider the example of electromagnetic force. When we want to know how two electrically charged static objects affect each other, we use the well known Coulomb's law

$$F = k_e \frac{Z_1 e \, Z_2 e}{R_{12}^2}, \tag{2.1}$$

where k_e is Coulomb's constant, R_{12}^2 is the distance between the two objects and $Z_{1/2}$ are the charges of those objects in multiples of the elementary charge e. Here the intrinsic power of the electromagnetic force is given by the size of the elementary charge e. In macroscopic scales this charge is constant but quantum electrodynamics (QED) tells us that in microscopic scales this is not the case. When looking on a charge from very close distance, its magnitude depends on the distance we are measuring it from. Therefore also the intrinsic strength of the electromagnetic force is changing with distance. To describe this change we introduce a so called running coupling constant denoted α_{em} which describes the strength of a force at a given distance. The same also applies for the strong force as described by QCD, here the coupling constant is denoted α_{s}.

From experiments on QED we know that the coupling constant for the electromagnetic force is rising when measured from small distances and decreases at larger distances until it settles at a constant value. However, from experiments on QCD we know that the coupling constant for the strong force decreases at low distances and increases at higher distances.

Here we see an explanation for the phenomenon of color confinement. When we try to separate two quarks in order to observe a single particle with non neutral color charge we have to overcome the growing strength of the coupling constant α_{s}. At some point the energy we provide for this separation, energy which is deposited in the strong color bond, is high enough so that it is more energetically efficient for the system to pull a quark-antiquark pair from the vacuum, therefore creating two new net color neutral particles, rather than stretching the color bond any further.

When considering the strong force at low distances between two quarks, at some point it gets so small that we assume the quarks are essentially free of this force. This effect is called asymptotic freedom.

This dramatic discrepancy in the behavior of the strong force when compared to the electromagnetic force can be justified by the crucial difference in the properties of the carriers of these forces. In the electromagnetic force the intermediate particles, i.e. photons do not carry the charge of the force they mediate. On the other hand gluons carry color charge. This fact plays a key role for so called screening.

2.3 Screening

The behavior of coupling constants can be explained throughout screening. In QED the electric charge can polarize the vacuum around it. This means polarizing virtual electron-positron pairs in the vacuum. These virtual pairs create a shield around the ”bare” electric charge and from experimental measurements we know that this shield causes the ”bare” electric charge to seem smaller. When computing this process the theory assigns the probability of its occurrence an infinite value. This would mean an infinite shield around the ”bare” electric charge causing it to be zero. But because in macroscopic measurements we still observe a finite electric charge, it means that the ”bare” electric charge also has to be infinite. The combination of the infinite ”bare” charge and the infinite shield yield a finite value for the macroscopic value of the elementary electric charge. The changes of the coupling constant for electromagnetic force correspond to the changes of the apparent electric charge.

In QCD a similar process occurs. The ”bare” color charge polarizes the vacuum around it and creates a shield of virtual particle pairs. But in QCD not just virtual quark-antiquark pairs can be polarized. As was mentioned earlier gluons also carry color charge and therefore virtual gluon pairs can be polarized as well (gluon is its own antiparticle, therefore we do not say gluon-antigluon pair). This is very important because the experiments show that the virtual gluons forming a shield have a stronger and opposite effect than electron-positron pairs in QED. This means that the color charge seems stronger from greater distance. And on the other hand when getting close to the ”bare” color charge it gets asymptotically small. The changes of the coupling constant for the strong force also correspond to the changes of the apparent color charge. Such behavior of the coupling constant is in agreement with the properties of the strong force described earlier.

Perturbative QCD

The fact that the coupling constant for the strong force gets asymptotically small for short distances is very important for perturbative QCD. A perturbative theory is used when an exact solution cannot be computed. The perturbative approach consists of a known exact solution for a similar problem and a correction to make the transition to the uncomputable problem. The correction is often written in the form of a power series with an expansion parameter. When the expansion parameter is small the most important contribution to the power series comes from the first order term and with increasing order of the parameters the terms become less numerically significant. This allows us to omit them and obtain a solution with precision given by the amount of terms included in the calculation.

In QCD there are problems which cannot be computed exactly, but the perturbative approach could solve them. However to be able to use the perturbation computation, the expansion parameter must be small. For QCD this expansion parameter is the coupling constant and therefore the possibility of α_s being small is very important. Results of particle experiments with small α_s can be predicted or compared with the results obtained by the theoretical computations.

2.4 Deep-inelastic scattering

One of the most important experiments in high-energy particle physics, which provided us with results consistent with the picture of QCD described above, is deep-inelastic scattering. Deep-inelastic scattering is the logical successor of microscopes. To see something, we need photons to interact with an object and then travel to our eye to be detected. But photons of the visible spectrum have certain wavelength and they cannot distinguish objects smaller than this wavelength. In order to observe particles we need to use something that has smaller wavelength than is the spatial extent of these particles. Deep-inelastic scattering uses the fact that when a probe particle has high momentum p its wavelength λ gets smaller which is described by the equation of the de Broglie wavelength

$$\lambda = \frac{h}{p}, \tag{2.2}$$

where h is the Planck constant. Instead of photons, leptons can be used to observe a particle. Both charged leptons (e, μ, τ) and neutral leptons $(\nu_e, \nu_\mu, \nu_\tau)$ can be used to probe the target in order to examine its properties, the first for electromagnetic properties and the second to examine behavior with regard to the weak force. But in reality the charged leptons, mainly electrons and muons, are used in the majority of cases because they are much more easily manipulated. These leptons are accelerated to a very high energy. When the high energy lepton hits a particle we want to observe, e.g., a proton or a lead nucleus, there is an interaction via an exchange of a virtual high-energy photon. The energy transfer in the interaction is usually so big that the observed proton is disintegrated in the process. But if we detect products of the collision, we can determine certain properties of the proton.

The main measurement of such an experiment is the cross section of the collision. Cross section can be viewed as the effective area of the target from the point of view of the probing particle and it is discussed further in Sec. 3.1.2. More precisely the goal of the

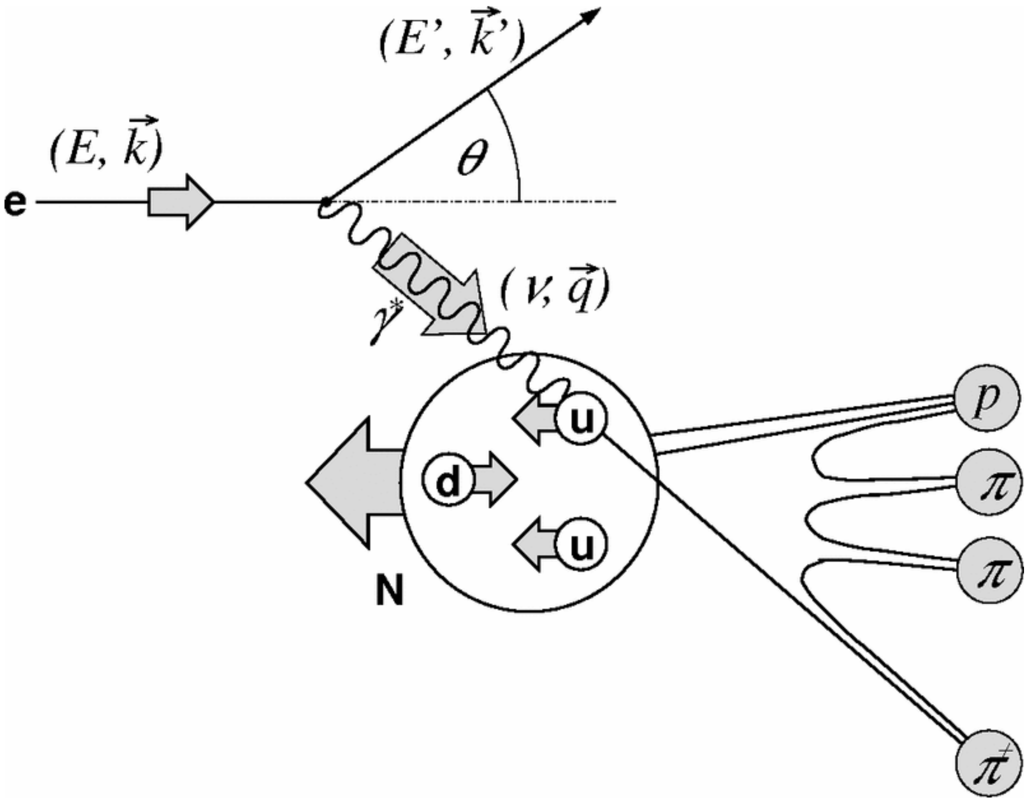

Figure 2.1: Diagram of an example of a deep-inelastic event. An electron e interacts with a nucleon (proton) N via the exchange of a virtual photon γ^{*} [3].

experiment is to measure the variation of the cross section with the energy lost by the probe [4]

$$\nu = E_i - E_f, \tag{2.3}$$

where E_i is the initial energy and E_f is the final energy, and the angle θ at which the probing particle is scattered after the collision which is described by the square of the momentum transferred in the collision [4]

$$q^2 = 2E_iE_f(1 - \cos\theta). \tag{2.4}$$

The momentum transferred in the collision q^2 is equal to the momentum of the virtual photon. How much is the photon virtual (i.e. off mass shell) is described by its virtuality

$$Q^2 = -q^2. \tag{2.5}$$

With Eq. 2.2 in mind we see that with higher virtuality we obtain a better resolution of the experiment, therefore Q^2 is often used to describe the resolution of the experiment. A diagram of a deep-inelastic experiment with the variables discussed above denoted in it can bee seen in Fig. 2.1.

2.4.1 Bjorken scaling

The measurement of the cross section σ and the kinematic parameters of the collision E_i, q^2 enables us to connect the experimental results to the theoretical predictions about the structure of the proton. Especially two ideas are very important for this. One of them is the parton model, proposed by Richard Feynman, which states that the proton is made up of smaller constituents called partons and all properties of these partons are to be determined by the experiments. And the second one is the idea of scaling introduced by James Bjorken. This idea states that when the momentum of the probing particle is very large the dependence of the measured cross section on the kinematic factors becomes simple. The changes of the cross section dependence on the kinematic factors can be then interpreted as that for low energies the probe scatters off the proton as if it is a point like object. For higher energies the dependence becomes more complicated as the probe starts to distinguish the inner structure of the proton but still scatters off the whole proton coherently. And for very high energies the dependence becomes simple again as the probe is now scattering incoherently only off a single point like parton.

The idea of scaling can be also examined with respect to the running coupling constant. The momentum of the probing particle sets a corresponding spatial resolution according to the Eq. 2.2. When the dependence of α_s on distance discussed in Sec. 2.2 is taken into account we get the following picture. For probes with energies in the range of the coherent scattering, the spatial resolution is such that the coupling constant is big enough that the partons interact with each other. This is reflected in the complicated behavior of the cross section. When the energy of the probe is high enough, the distance scale gets small enough and the coupling constant approaches the asymptotic free region. This means that the partons interact very weakly and can be considered practically as free particles which is resulting in the simple dependence of the cross section on the kinematic factors. When considering the momentum - wavelength relation via Eq. 2.2, the experimental results are confirming the behavior of the strong coupling constant α_s described in Sec. 2.2. An example of such experimental results can be seen of Fig. 2.2.

2.4.2 Structure functions

With these ideas in mind and other assumptions a formula describing the cross section dependence on the kinematic factors can be derived. This formula has to contain a part describing the electron and a part describing the virtual photon. These are well described in quantum electrodynamics but the formula also has to contain a part describing the proton and the complicated disintegration process. This problematic part is described by so called structure functions of which we assume no previous knowledge and we want to establish their properties from deep-inelastic experiments. The Eq. 2.6 is taken from [4]

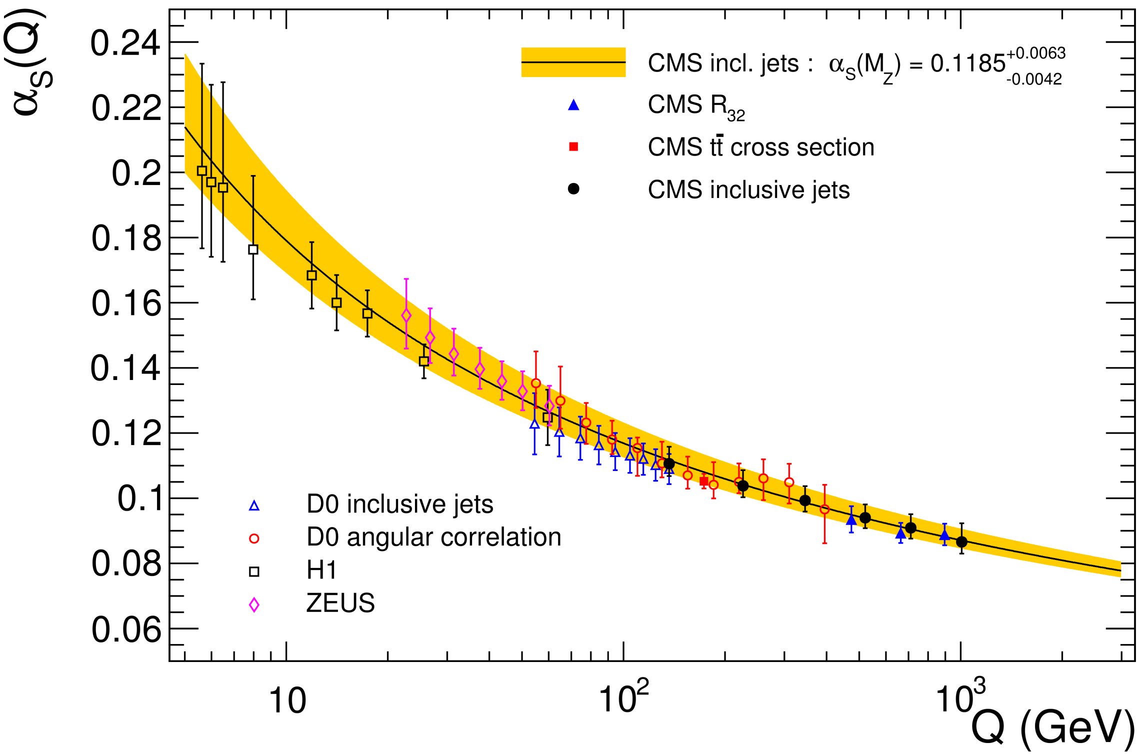

Figure 2.2: The coupling constant of the strong force (α_s) as a function of the negative momentum transferred in the collision (Q) [5].

$$\frac{\mathrm{d}^2\sigma}{\mathrm{d}q^2\,\mathrm{d}\nu} = \frac{4\pi\alpha_{\mathrm{em}}^2}{q^4}\frac{E_f}{E_i M_N}\left[\frac{M_N}{\nu}F_2(q^2,\nu)\cos^2\frac{\theta}{2} + 2F_1(q^2,\nu)\sin^2\frac{\theta}{2}\right], \tag{2.6}$$

where M_N is the mass of the nucleon (proton). The structure functions are introduced into the equation as numbers with now physical dimension and if they are to have any dependence on the physical quantities q^2 and ν, their physical dimensions must cancel out. Bjorken suggested that this will be achieved if the structure functions are dependent only on a dimensionless ratio of the two and not on each independently. He chose this ratio to be [4]

$$x = \frac{q^2}{2M_N\nu}. \tag{2.7}$$

Therefore for the high energies of deep-inelastic scattering, which can be approximated by the limit of q^2, $\nu \to \infty$, we can write the structure functions as only dependent on x

$$\lim_{q^2,\nu\to\infty} F_{1,2}(q^2,\nu) \to F_{1,2}(x). \tag{2.8}$$

It turns out that the variable x chosen by Bjorken also has a significant physical interpretation. It is the fraction of the momentum of the proton carried by the parton which was struck by the probing photon.

When comparing Eq. 2.6 with the formula for scattering of an electron with a particle of spin $\frac{1}{2}$ obtained from QED, a relation between the structure functions may be derived [4]

$$2xF_1(x) = F_2(x). \tag{2.9}$$

And it turns out that this ratio is in agreement with the experimental results suggesting that partons have spin $\frac{1}{2}$, which is in agreement with the picture of $\frac{1}{2}$ spin quarks. Another conclusion, which may be derived when comparing the structure functions of Eq. 2.6 with QED, is that the structure functions are essentially distributions of the electric charge in the proton.

2.5 Saturation

When more extensive and precise deep-inelastic experiments were conducted, it was discovered that the dependence of the structure functions on the kinematic factors was not as simple as suggested by Bjorken. The structure functions vary not only with the Bjorken x but also with the transferred momentum q^2. This can be seen in Fig. 2.3 and it also shows why the earlier experiments, which examined the structure functions only for limited ranges of q^2 and mainly in the mid-x region, did not observe the q^2 dependence. With this fact in mind the structure functions for deep-inelastic experiments have to be written as dependent both on x and q^2

$$F_{1,2} = F_{1,2}(x, q^2). \tag{2.10}$$

Very important is the fact that structure functions at leading order, which means including only the first order term in the perturbation calculation, may correspond with both cross section and number of particles. This correspondence is complicated and varies depending on the theoretical model which is used to calculate them. For the purpose of this thesis suffices the information that the structure functions are proportional to them.

When we examine the dependence of the structure functions on x and q^2 displayed in Fig. 2.3 now armed with the new interpretation of the structure functions, we can make several deductions. We observe lower number of partons with high x, as that would mean that one of the partons is carrying the majority of the proton momentum and the others just the remaining fraction. For quarks of similar mass this means that one of them has significantly higher velocity which would eventually result in the separation of the quarks. But as we know the color confinement of the strong force will not allow this. Therefore a quark can have majority of the momentum of the proton just for a brief time until the strong force compensates it. With increasing q^2, which provides us with better resolution,

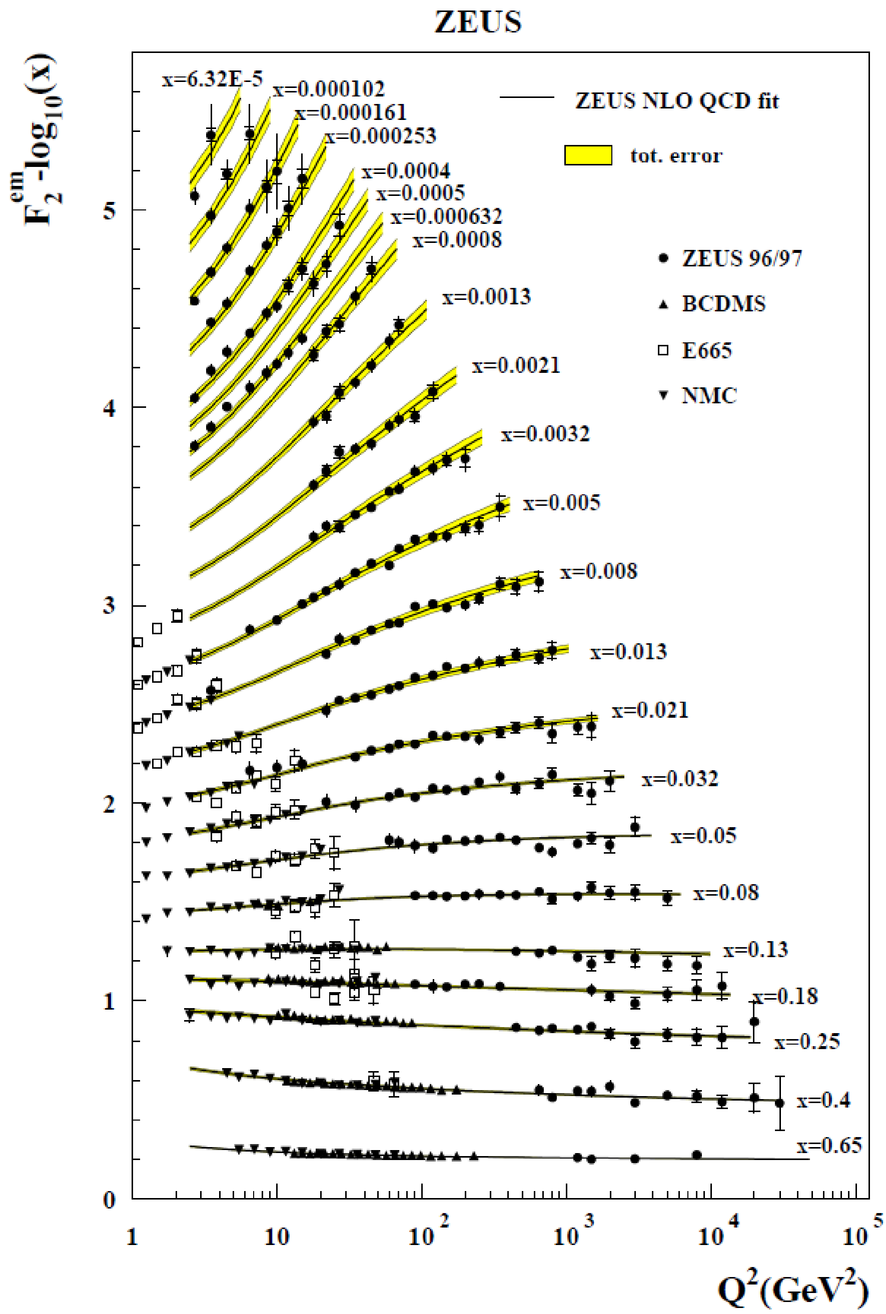

Figure 2.3: Measurement of the structure function F_2 dependence on the negative transferred momentum Q^2 for different Bjorken x [6].

we observe even fewer partons with high x. On the other hand we observe more partons carrying a small portion of the proton's momentum. And with better resolution, provided by the higher q^2, the amount of observed low x partons rises, which is exactly the opposite effect as for high x. This can be interpreted as that when using a probe with better resolution, we can observe more complicated quantum sub-processes of the QCD.

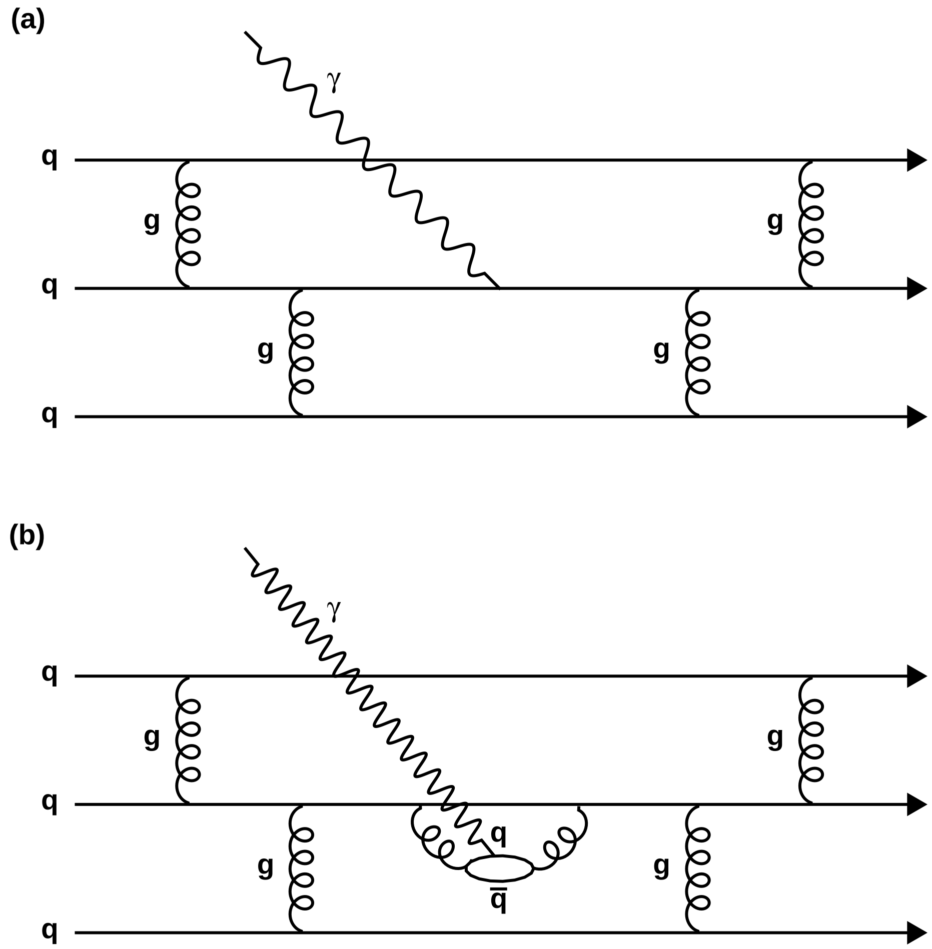

Figure 2.4: Illustration of the proton structure as it might be observed by longer-wavelength probe (a) and shorter-wavelength probe (b).

For example a longer-wavelength probe can see just a quark but with shorter-wavelength probe we can resolve a quark accompanied by a gluon. But the gluon + quark state measured by the shorter-wavelength probe has to have the same momentum as the isolated quark measured by the longer-wavelength probe. For higher values of q^2 this will result in observing more partons but with lower values of x. An example of a similar situation is illustrated in Fig. 2.4.

Let us now consider the structure functions of partons in a proton as the function of Bjorken x. If the proton was made up of three independent quarks, the structure functions would have just a single value, same for all three quarks which would each carry a third of the proton' s momentum. But as we know the quarks are bound together by the continuous exchange of gluons. This causes the structure functions to have a probabilistic distribution over x, having low values for big and small x and high value for x around $\frac{1}{3}$. This behavior can be seen in Fig. 2.5.

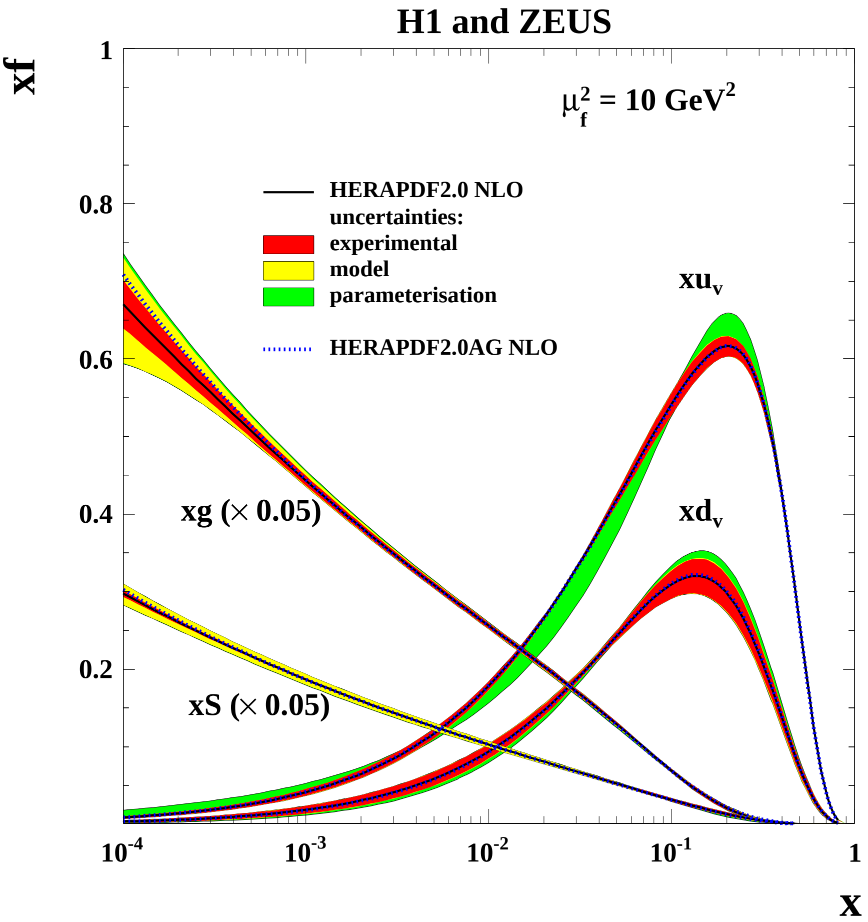

Figure 2.5: The parton distribution functions from HERAPDF2.0 at $Q^2 = 10\ \mathrm{GeV}^2$. The gluon and sea distributions are scaled down by a factor of 20. $\mathrm{xu_v} \sim$ up valence quarks, $\mathrm{xd_v} \sim$ down valence quarks, $\mathrm{xS} \sim$ sea quarks, $\mathrm{xG} \sim$ gluons [7].

However the graph also reveals a rise of parton distribution functions for other partons at low x. From the information discussed in the paragraph above, we can conclude that when using a higher momentum probe, in Fig. 2.5 momentum of the probe is $q^2 = 10\ \mathrm{GeV}^2$, we will observe more partons with low values of x and less partons with high values of x. This fact would explain the rise of structure functions at low x. As it turns out, the partons that are observed at low x are the sea quarks (virtual quark-antiquark pairs) and predominantly gluons. This means that when observing a proton with good enough resolution (high enough q^2), it is possible to measure the quantum sub-processes of QCD discussed above. With higher values of q^2 valence quarks of a proton (uud) exist in states with more and more gluons which can then exist as virtual quark-antiquark pairs or split into more gluons. For certain value of x this would eventually lead to a number of gluons and sea quarks whose total cross section would be bigger than is the cross section of the proton. Such a result is of course impossible and therefore a process which will compensate the splitting of the partons must occur. This process is called saturation and it predicts that for values of given x and smaller the gluons and sea quarks would recombine back to fewer partons with higher x rather than keep splitting.

2.6 Nuclear shadowing

Nuclear shadowing describes how are the nuclear structure functions different from the sum of the structure functions of their constituents. The existence of this difference is a well know experimental fact. For the structure function F_2 the nuclear ratio is defined as [8]

$$R^A_{F_2}(x,q^2) = \frac{F_2^A(x,q^2)}{AF_2^{\text{nucleon}}(x,q^2)}, \tag{2.11}$$

where $F_2^A(x,q^2)$ is the nuclear structure function of a nucleus with mass number (number of nucleons) A and $F_2^{\text{nucleon}}(x,q^2)$ is the structure function of a nucleon. The structure function of a nucleon is defined through measurements on deuterium as

$$F_2^{\text{nucleon}}(x,q^2) = \frac{F_2^{\text{deuterium}}(x,q^2)}{2}, \tag{2.12}$$

assuming nuclear effects in deuterium to be negligible.

The experimental data on nuclear shadowing, which are available only for not very small x and small or moderate Q^2, indicate the following behavior. Shadowing increases with decreasing x and increasing A. Shadowing decreases with increasing Q^2. However there are no available data on the dependence of the nuclear shadowing on the impact parameter b, which will be introduced in Sec. 3.1.

The phenomenon of nuclear shadowing is related to multiple scattering of the virtual photon on the target nucleus. It is possible to derive the following correspondence between the structure function F_A^2 and the cross section of the collision σ_{γ^*-A}

$$F_A^2(x,Q^2) = \frac{Q^2(1-x)}{4\pi^2\alpha_{\text{em}}}\sigma_{\gamma^*-A}. \tag{2.13}$$

There are many models describing nuclear shadowing and they differ in a variety of things. Some of them approach the virtual photon interaction as hadron fluctuation (vector dominance models) and some as quark-antiquark pair (dipole models). Some models try to explain the origin of shadowing via the multiple scattering process and other focus just on describing the evolution of the shadowing. The interpretation of these models is also frame dependent. More information and description of concrete models may be found in [8].

For small values of x the nuclear ratio $R^A_{F_2}(x,q^2)$ is smaller than one. Therefore the the nuclear structure function and consequently the nuclear cross section, via Eq. 2.13, is smaller than the sum of the cross sections of the constituent nucleons. Let us now consider the phenomenon of saturation discussed in Sec. 2.5 and use it to explain nuclear shadowing. In the region of small x the saturation for nucleons in a nucleus may occur at higher x than if they were free. This is due to the possibility of interaction between gluons from different nucleons which are very close to each other. Such a process will result in $R^A_{F_2}(x,q^2) < 1$. Therefore we have to consider a dependence of the nuclear saturation on the atomic mass number. A graph predicting the nuclear saturation scale dependence on the atomic mass number A and the Bjorken x can be seen in Fig. 2.6.

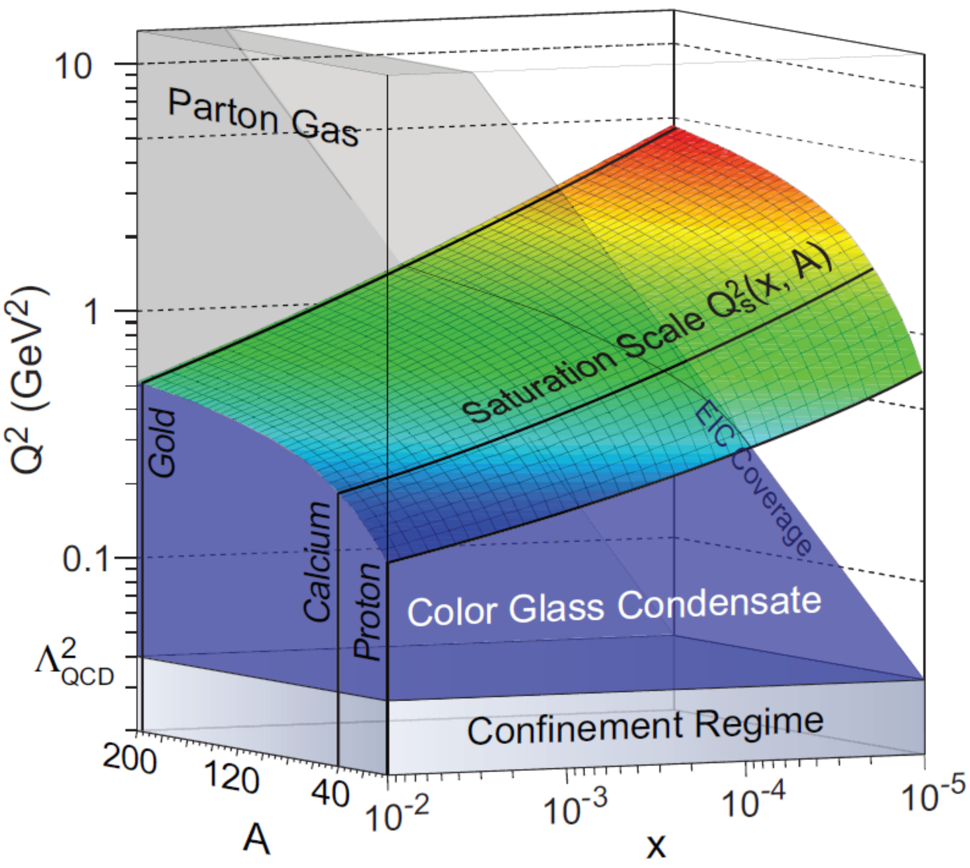

Figure 2.6: Theoretical expectations for the saturation scale at medium impact parameter as a function of Bjorken x and the nuclear mass number A [9].

Chapter 3

Ultra-peripheral collisions

Ultra-peripheral collisions (UPC) are in several aspects similar to the deep-inelastic scattering discussed in Sec. 2.4. They are a great tool to examine the fundamental properties of QED and QCD. They provided us with the first evidence for nuclear shadowing, discussed in Sec. 2.6, caused by gluons [10]. Ultra-peripheral collisions also enable us to study gluon distribution functions for small values of Bjorken x and at high resolution. The LHC is capable of providing energies never reached before for UPC. This makes ultra-peripheral collisions a great candidate to measure and explore the gluon saturation discussed in Sec. 2.5.

3.1 Definitions

3.1.1 Impact parameter, centrality, multiplicity

Impact parameter (b) is defined as the transverse distance between the centers of two colliding particles. Centrality classifies what type of collision is occurring depending on the impact parameter and the radius of the involved particles (R_1 and R_2). A collision is called central (head on), if the impact parameter is much smaller than the radius of the colliding particles. If the impact parameter is approximately the same as the sum of the radii ($b \approx R_1 + R_2$) the collision is refereed to as peripheral. And if the impact parameter is bigger than the sum of the radii of the colliding particles an ultra-peripheral collision takes place. All three of these situations are illustrated in Fig. 3.1.

The centrality of a collision may be connected to the number of particles produced in the collision. The number of particles produced in a collision is called multiplicity.

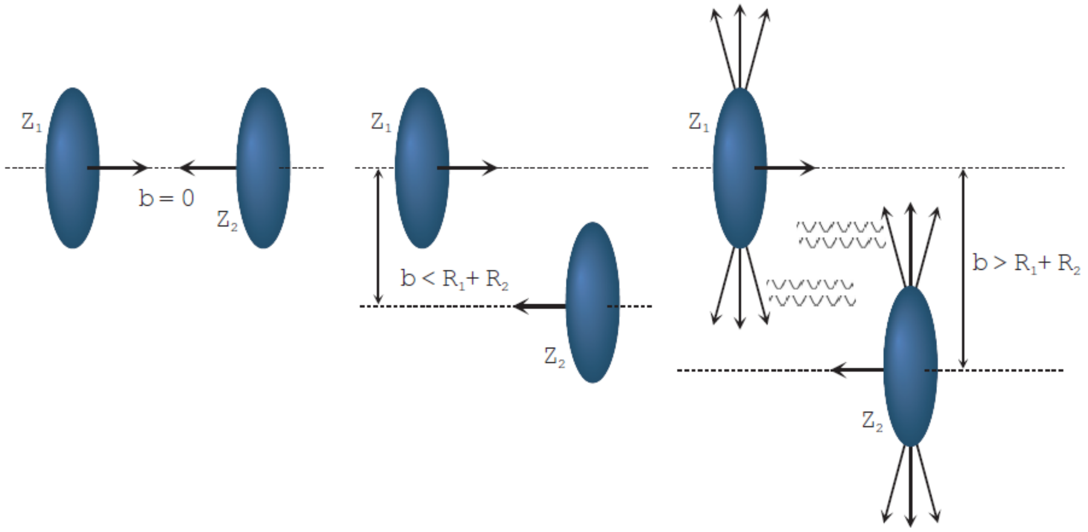

Figure 3.1: Type of collisions with different centrality. From left: central, peripheral, ultra-peripheral [11].

3.1.2 Cross section

Cross section is the effective area of a collision. It quantifies the probability of a particular event occurring. The differential cross section gives the probability of a particle, produced in a collision, scattering in a given solid angle. Total cross section over the solid angle ($\mathrm{d}\Omega = \sin\theta\,\mathrm{d}\theta\,\mathrm{d}\varphi$) is calculated as

$$\sigma_{tot} = \oint \frac{\mathrm{d}\sigma}{\mathrm{d}\Omega}\mathrm{d}\Omega = \int_0^{2\pi}\int_0^{\pi} \frac{\mathrm{d}\sigma}{\mathrm{d}\Omega}\sin\theta\,\mathrm{d}\theta\,\mathrm{d}\varphi. \tag{3.1}$$

The SI unit of cross section is m^2. In particle physics it is more convenient to use a smaller unit called barn $b = 10^{-28}\ \mathrm{m}^2$.

3.1.3 Luminosity

Luminosity (L) is linked to the number of events produced in an experiment. The number of events (N) with cross section (σ) produced per unit of time (t) is

$$\frac{\mathrm{d}N}{\mathrm{d}t} = \sigma L. \tag{3.2}$$

The dimension of luminosity is number of events per time per area. Units commonly used for luminosity are $\mathrm{cm}^{-2}\mathrm{s}^{-1}$ and $\mathrm{b}^{-1}\mathrm{s}^{-1}$.

In theory the luminosity of a circular collider experiment can be calculated as

$$L = \frac{f}{4\pi} \frac{n_1 n_2}{\sigma_x \sigma_y}, \tag{3.3}$$

where n_1, n_2 are the number of particles in accelerated bunches, f is the frequency at which they circulate in the accelerator and σ_x, σ_y are cross sections of the bunches. But in reality we do not know the precise cross section of a bunch in a collider and therefore we have to use a different approach. At the LHC the luminosity of the apparatus is determined with the help of so called van der Meer scans.

Van der Meer scans are special runs where the beams are moved against each other to measure their geometrical properties and at the same time a reference process is measured, so that the cross section for that reference process is obtained. Later on, this cross section is used to determine the luminosity in normal running conditions

The amount of produced events over certain time (T) can be well described by the integrated luminosity (L_{int})

$$L_{int} = \int_0^T L \, \mathrm{d}t. \tag{3.4}$$

3.1.4 Rapidity and pseudorapidity

Rapidity is defined as

$$y = \frac{1}{2} \ln \frac{E + p_l}{E - p_l}, \tag{3.5}$$

where E is the total energy of a particle and p_l is its longitudinal momentum. Rapidity is not invariant under Lorentz transformation, but it is additive in Lorentz transformation along the longitudinal axis. Because of this it is used to describe relativistic particles in a similar way as speed is used to described non-relativistic particles.

Pseudorapidity is defined as

$$\eta = -\ln \tan \frac{\theta}{2}, \tag{3.6}$$

where θ is the deviation of a particle from the longitudinal axis of the collision. The biggest advantage of pseudorapidity is the fact that it depends only on the angle θ, which can be easily measured in a detector. When considering the limit of a particle traveling at very high speed, it can be derived that

$$\eta = \frac{1}{2} \ln \frac{|\vec{p}\,| + p_l}{|\vec{p}\,| - p_l}, \tag{3.7}$$

which for rest mass negligible in comparison to the momentum of the particle means $|\vec{p}\,| \approx E$ therefore the definition of pseudorapidity converges to the definition of rapidity.

3.2 Photoproduction

Ultra-peripheral collisions at ALICE are realized by accelerating a lead ion and a particle that we want to observe (e.g. another lead ion or proton). When the ion is accelerated nearly to the speed of light, its electromagnetic filed becomes flat due to relativistic effects. This field around the ion can be then considered as a field of virtual photons with low virtuality, often called quasi-real [10]. Due to particles being far enough in UPC so that the strong interaction between them is suppressed, they interact only via these quasi-real photons. Through the semi-classical approach the photon flux per unit area is given by [10]

$$n(k,b) = \frac{\alpha_{\mathrm{em}} Z^2}{\pi^2 b^2} x^2 \left[K_1^2(x) + \frac{1}{\gamma} K_0^2(x) \right], \tag{3.8}$$

where k is the energy of the photon in the nucleus frame with Lorentz factor γ, Z is the electric charge of the nucleus, K_0 and K_1 are the Bessel functions and $x = kb/\gamma$. This formula is only valid for heavy-ion nuclei in collisions with impact parameter b larger than b_{min} which is the sum of the radii of the colliding particles. The integrated photon flux

$$n(k) = \int \mathrm{d}^2 b \; n(k,b) \tag{3.9}$$

is then given by [10]

$$n(k) = \frac{2\alpha Z^2}{\pi} \left[\xi K_0(\xi) K_1(\xi) - \frac{\xi^2}{2} (K_1^2(\xi) - K_0^2(\xi)) \right], \tag{3.10}$$

where $\xi = kb_{min}/\gamma$.

The intensity of the quasi-real photon flux is proportional to the charge Z of the ion as $\sim Z^2$, that is why heavy ions allow us to perform UPC experiments. The energy of the accelerated ion is reflected in the photon intensity through the Lorentz factor.

3.2.1 Exclusive photoproduction of J/ψ

In this thesis we are interested only in exclusive J/ψ photoproduction, an event where only the J/ψ is created and nothing else. But the J/ψ is short-lived and we detect only its decay products. The main decay channel of the J/ψ is into several lighter hadrons. It is necessary to measure the kinematics of the J/ψ, but that is very hard for many hadronic products. Therefore we measure only the dilepton ($e^+ + e^-$, $\mu^+ + \mu^-$) decay channel of the J/ψ which occurs only in approximately 12 % of cases, as discussed in Sec. 1.1.3. This gives us a clear idea of the tracks measured by the detector for this event. A comparison of the tracks left in the ALICE detector by a central hadronic collision and an ultra-peripheral collision where the exclusively produced J/ψ decays into two leptons can be seen in Fig. 3.2.

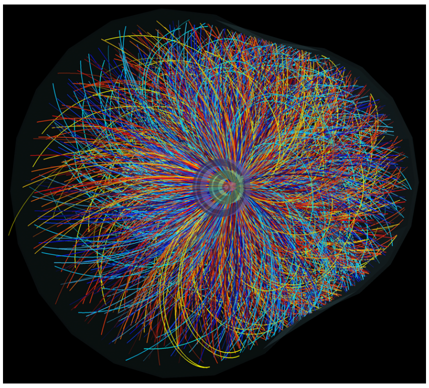

(a) Central collision.

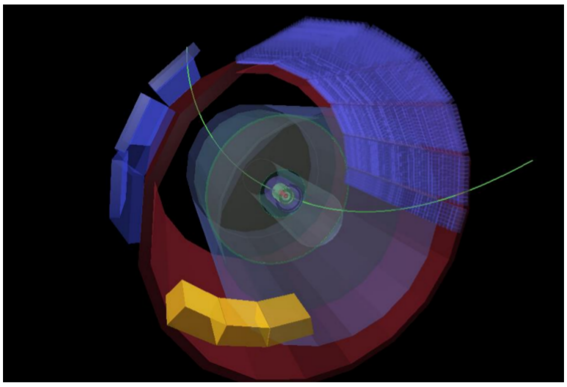

(b) Ultra-peripheral collision.

Figure 3.2: Comparison of the track left in the detector by a central hadronic collision Pb-Pb (a) and an ultra-peripheral collision (b) [12].

The are several UPC processes that lead to exclusive J/ψ photoproduction. They can be classified as follows.

3.2.2 Photon-nucleus interactions in Pb-Pb UPC

The cross section for J/ψ photoproduction in Pb-Pb UPC is given by [10]

$$\frac{d\sigma_{\mathrm{PbPb}}(y)}{dy} = N_{\gamma\mathrm{Pb}}(y,M)\sigma_{\gamma\mathrm{Pb}}(y) + N_{\gamma\mathrm{Pb}}(-y,M)\sigma_{\gamma\mathrm{Pb}}(-y), \tag{3.11}$$

where M is the mass of the produced J/ψ and $y = \ln(2k/M)$ is its rapidity, where k is the photon energy and $\sigma_{\gamma\mathrm{Pb}}(y)$ is the cross section of the photon-nucleus process.

There are two terms in Eq. 3.11 because both of the lead nuclei can act as the source of the photon.

With corresponding values of Z and γ for the accelerated lead ion and using rapidity y instead of the photon energy k we obtain the photon flux $N_{\gamma\mathrm{Pb}}$ created by the lead nucleus from Eq. 3.10 as [10]

$$N_{\gamma\mathrm{Pb}}(y,M) \equiv k \left. \frac{dn(k)}{dk} \right|_{\mathrm{Pb}}. \tag{3.12}$$

The collision of the photon and the lead nucleus can be coherent, meaning the photon interacts with the whole nucleus. This corresponds to values of transverse momentum of the produced J/ψ around $p_t \sim 60$ MeV/c [10]. These processes mostly result in the lead nucleus being intact, but due to the intense electromagnetic filed secondary electromagnetic processes may occur. They result in excitation of the ion which consequently radiates at least one neutron in the direction of its movement.

The collision of the photon and lead nucleus can be also incoherent, meaning the photon interacts only with a given nucleon in the nucleus. Because the radius of the nucleon is much smaller than that of the nucleus, the corresponding transverse momentum of the produced J/ψ is higher $p_t \sim 300$ MeV/c [10]. In this case the lead nucleus almost always disintegrates producing forward neutrons.

3.2.3 Photon-proton interactions in p-Pb UPC

The cross section for J/ψ photoproduction in p-Pb UPC is similar to Eq. 3.11, but with only one term because the charge of the proton is much smaller than that of the lead ion and therefore the photon flux induced by the proton can be neglected. This gives the cross section as [10]

$$\frac{\mathrm{d}\sigma_{\mathrm{pPb}}(y)}{\mathrm{d}y} = N_{\gamma\mathrm{Pb}}(y, M)\sigma_{\gamma\mathrm{p}}(y). \tag{3.13}$$

The photon-proton collision can be elastic, meaning the proton stays unchanged after the collision. This corresponds to the same momentum scale as in the photon-nucleus incoherent case $p_t \sim 300$ MeV/c [10].

Or the photon-proton collision can be dissociative, meaning the proton is disintegrated in the process. Such an event corresponds to transverse momentum of the produced J/ψ above $p_t \sim 1$ GeV/c [10].

Here we will discus an example of the interpretation of the cross section measurement. When considering perturbative QCD the interaction of the photon and proton can be described by the exchange of a colorless system of two gluons. This enables us to connect the cross section of this process to the gluon distribution functions, which are of great interest. In the leading logarithmic approximation at zero transferred momentum $t = 0$ and negligible photon virtuality, the photon-proton elastic cross section for production of J/ψ with mass $M_{J/\psi}$, which decays into a pair of electrons, is [12]

$$\left.\frac{\mathrm{d}\sigma_{\gamma p}}{\mathrm{d}t}\right|_{t=0} = \frac{\Gamma_{ee}\pi^3\alpha_\mathrm{s}}{3M_{J/\psi}\alpha_\mathrm{em}}\left[xg(x, Q^2)\right]^2, \tag{3.14}$$

where x is the Bjorken x, Γ_{ee} is the width of the dielectron decay, $Q^2 = M_{J/\psi}/4$ and $xg(x, Q^2)$ is the gluon parton distribution function.

A general diagram of the p/Pb-Pb ultra-peripheral collision producing a J/ψ meson can be seen in Fig. 3.3.

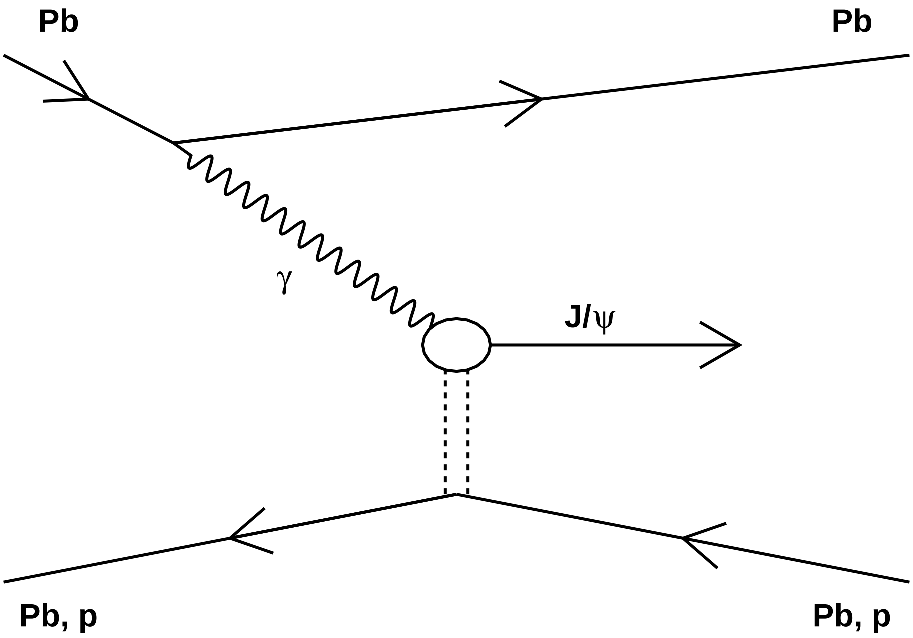

Figure 3.3: Exclusive photoproduction of a J/ψ vector meson in a Pb-Pb or p-Pb ultra-peripheral collision.

3.2.4 Photon-photon interactions in $\gamma\gamma$ UPC

When two lead ions are colliding also photon-photon collisions are possible. They can result in the production of a pair of leptons and therefore they will contribute to the total measurement. The cross section for dilepton production at lowest order in QED is given by [12]

$$\sigma_{\gamma\gamma} = \frac{\pi\alpha_{\text{em}}^2}{4s}\beta\left[\frac{3-\beta^4}{2\beta}\ln\frac{1+\beta}{1-\beta} - 2 + \beta^2\right], \tag{3.15}$$

where $\beta = \sqrt{1-4m_l^2/s}$ is the velocity of the lepton, with mass m_l, in the rest frame of the photon system and s is the total energy of the system.

A diagram of a $\gamma\gamma$ ultra-peripheral collision can be seen in Fig. 3.4.

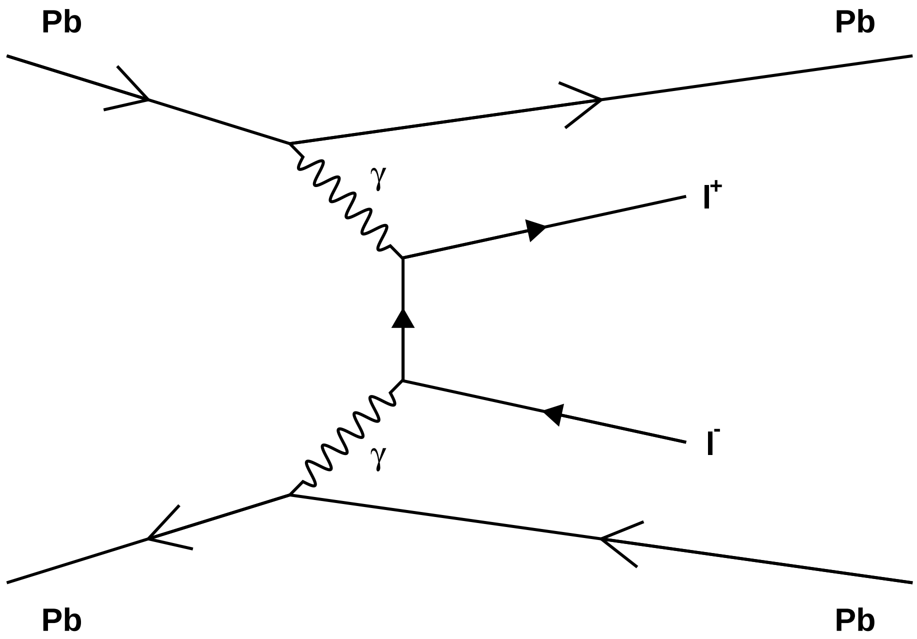

Figure 3.4: Lepton pair production by $\gamma\gamma$ interaction in a Pb-Pb ultra-peripheral collision.

3.2.5 Models for J/ψ photoproduction

There are many models that try to predict the cross sections for photoproduction in ultra-peripheral collisions. To name some of them [10]: AB-AN, CSS, KN, LM, GM-GDGM, RSZ, IKS. All these models are based on Eq. 3.11, therefore they have two main parts: the photon flux and the photonuclear cross section. They differ in both.

Some of them (CSS, LM, GM-GDGM) use Eq. 3.10 to describe the photon flux and other (AB-AN, KN, RSZ-GZ) integrate the convolution of Eq. 3.8 with the probability of no hadronic interaction. When approaching the photonuclear cross section the models can be divided into three groups.

Models based on the generalized vector dominance model (KN), which rely on the idea that the quasi-real photon fluctuates to a vector meson (J/ψ) which then interacts with the nucleus (Pb) or proton (p).

Models based on the leading order (LO) pQCD (AB-AN, RSZ), which use the methods of perturbative calculations. This is the model used as an example in Sec. 3.2.3 enabling the derivation of the Eq. 3.14.

And the color dipole models (CSS, LM, GM-GDGM). Their basic idea is that the quasi-real photon fluctuates into a quark-antiquark pair which forms a color dipole and this dipole then interacts with the ion (Pb) or proton (p). After the interaction the dipole proceeds to crate a vector meson, J/ψ in our case.

A more thorough and in depth report on the models used for predicting cross sections of photoproduction processes can be found in [10].

Chapter 4

The ALICE experiment at the CERN LHC

A brief description of the CERN organisation and the Large Hadron Collider is at the beginning of this chapter. After that follows a description of selected ALICE sub-detectors together with the trigger and data acquisition system. Numerical values in this chapter are taken from [13], [14] and the official CERN website, unless cited otherwise.

4.1 CERN

The European Organization for Nuclear Research (CERN), founded in 1954, operates the largest accelerator complex in the world (see Fig. 4.1). It is located on the Franco-Swiss border near the city of Geneva. CERN is an international collaboration of 22 member states, but many other states have observer status which means that they can be active members of the collaboration, but they have no decision rights.

The main purpose of CERN is to provide technology (e.g. accelerators) and infrastructure necessary for scientists who are trying to answer fundamental questions of Nature. In its history CERN was, and still is, involved in the development of many technological fields. Moreover, many famous discoveries were made in CERN, such as the discovery of W and Z bosons, the first creation of antihydrogen and in recent years the discovery of the Higgs boson. Finally, CERN has also contributed to the world with the invention of the World Wide Web.

4.2 The Large Hadron Collider

The Large Hadron Collider (LHC) is the largest and most powerful particle accelerator in the world. It was designed to accelerate protons and heavy ions. It is located as deep as

175 meters under ground and has 27 kilometer circumference. The LHC is a synchrotron accelerator consisting of two beam pipes accelerating particles in opposite directions and subsequently colliding them at the four sites of the main experiments: ATLAS, CMS, ALICE and LHCb.

Particles in the LHC are accelerated once per orbit by 16 radiofrequency cavities (8 per each beam). The necessary turning of the accelerated particles is achieved by 1232 fifteen-meter long superconducting dipole magnets. Another 395 quadrupole superconducting magnets, which are 5-7 meter long, are installed for the purpose of beam focusing. In order to keep all the magnets at a superconducting temperature the LHC has the largest cryogenic system in the world, using liquid helium at a temperature of -273.15°C. In order to avoid collisions of the accelerated particles with the gas inside the beam pipes the LHC employs the world's largest vacuum system, which is keeping the beam pipes at ultra-high vacuum with a pressure as low as 10^{-11} mbar.

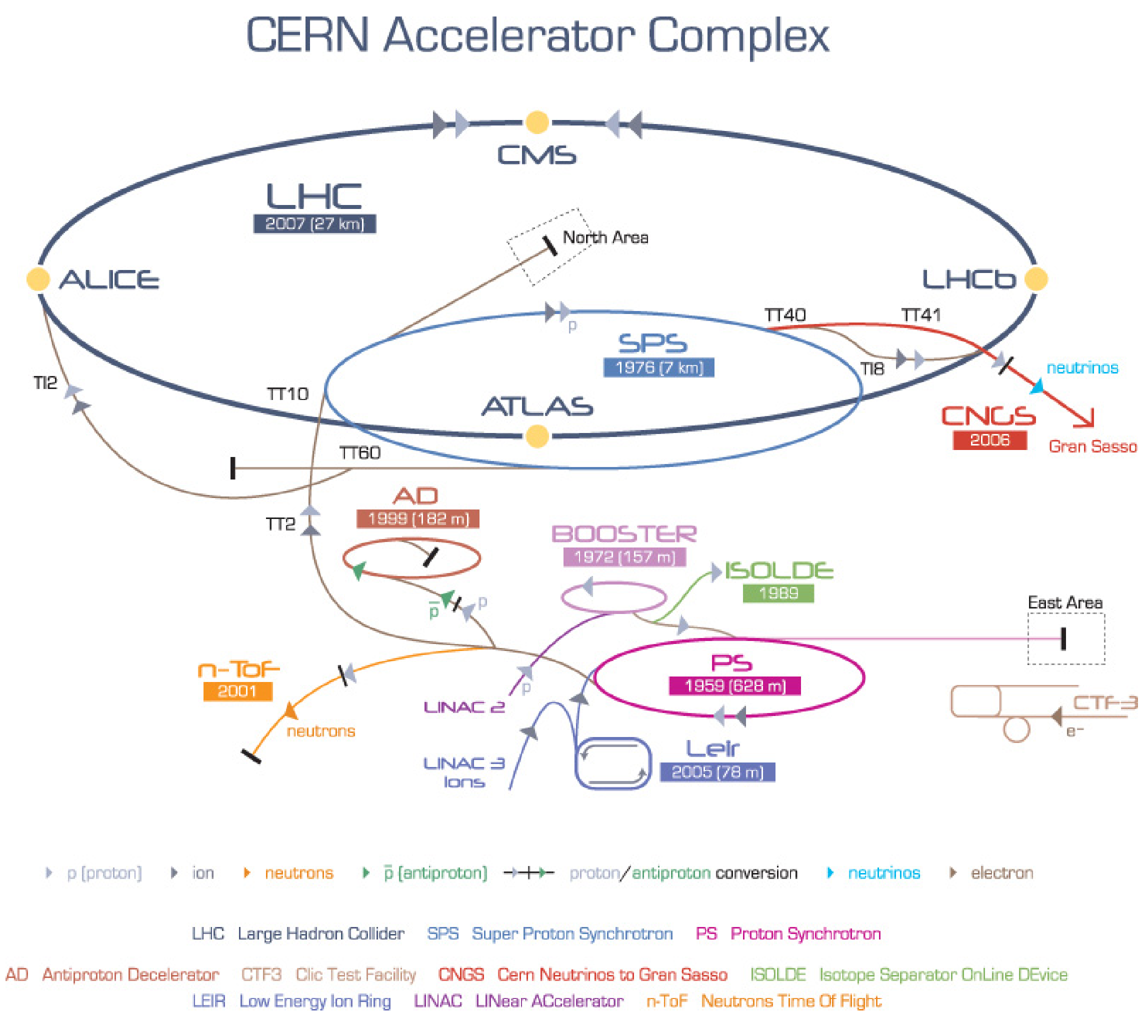

Figure 4.1: Diagram of the CERN accelerator complex [15].

The LHC is not a stand-alone collider, it is a part of a huge accelerator complex, as can be seen in Fig. 4.1. For a proton to be accelerated by the LHC it must undergo several steps. A hydrogen gas striped of electrons by an electric field serves as a source of protons. These are then accelerated by the linear accelerator Linac 2 to an energy of 50 MeV. The created beam is then accelerated by the Proton Synchrotron Booster (PSB) to 1.4 GeV, followed by the Proton Synchrotron (PS), which accelerates the beam to 25 GeV. Finally, the protons are accelerated by the Super Proton Synchrotron (SPS) to 450 GeV and inserted into the LHC. Here after 4 minutes and 20 seconds of filling and 20 minutes of accelerating they reach their maximum energy of 6.5 GeV. When the two beams are collided at the four experimental sites, the total energy at the collision point is 13 TeV.

For accelerating lead ions a piece of solid lead is vaporized as a source material. The ions are then accelerated by the linear accelerator Linac 3. From there on, they are collected and accelerated by the Low Energy Ion Ring (LEIR). After this, they follow the same route as protons.

4.3 ALICE

A Large Ion Collider Experiment (ALICE) is one of the four main experiments located along the CERN LHC ring. The ALICE Collaboration, which designed, built and maintains in operation the ALICE detector, is an international collaboration of more then 1500 physicists, engineers and technicians, involving hundreds of graduate students, from 157 institutions in 37 countries around the world.

It was designed as a general-purpose heavy-ion detector focusing on the QCD segment of the Standard Model. It can study the extremely hot and dense state of matter called quark-gluon plasma in Pb-Pb collisions via measurement of electrons, muons, hadrons and photons coming from the collision. Moreover, ALICE can be also used to study rare events such as UPC. The physics program for ALICE also includes lighter ions collisions as well as proton-ion collisions and proton-proton collisions.

ALICE is a massive detector with dimensions of $16\times16\times26$ m^3, weighting approximately 10 000 tons. It is composed out of two main parts, a central barrel covering polar angles from 45° to 135° and capable of measuring hadrons, photons and electrons; and a forward muon spectrometer. The central part is embedded in a large 0.5 T solenoid magnet which is reused from the L3 experiment at LEP.

Furthermore, ALICE is composed out of many detector subsystems (its schematic layout can be seen in Fig. 4.2), for the purpose of this thesis only several of them will be described: the Inner Tracking System (ITS) composed of six layers of precise Silicon Pixel (SPD), Strip (SSD) and Drift (SDD) Detectors, the Time-Projection Chamber (TPC), the Time-Of-Flight (TOF) detector, the muon spectrometer, the Zero Degree Calorimeter (ZDC), the V0 detector and the ALICE Diffractive (AD) detector.

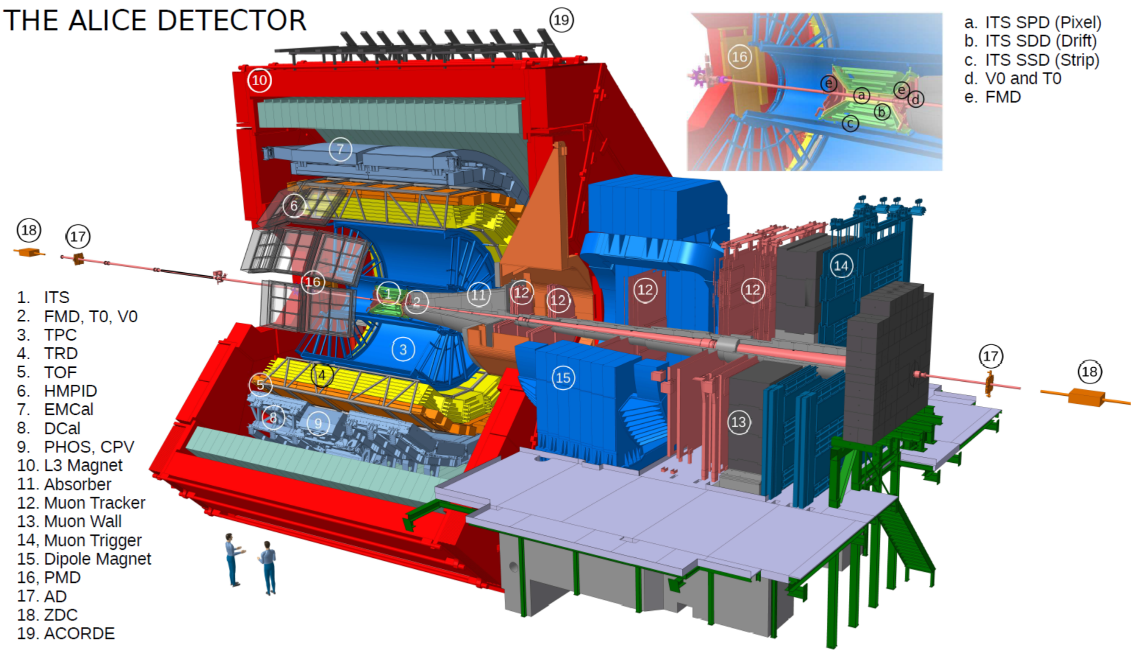

Figure 4.2: Schematic layout of the ALICE detector [16].

4.3.1 Inner Tracking System

The main purpose of the Inner Tracking System (ITS) is to localize the primary vertexes with resolutions better than 100 μm and to reconstruct the secondary vertexes from weak decays of unstable particles. The ITS can also identify particles with momentum lower than 200 MeV/c and it improves momentum and angle resolution for tracks reconstructed by the Time-Projection Chamber. For precise measurements it is very important, that the beam pipe does not move relative to the ITS, therefore a carbon support structure holds both the beam pipe and the ITS in one place. For the particles from the primary vertex to be able to pass through the ITS to other detectors, the amount of material in the detector cannot be too high. But there is a minimum required width of the material so that the particle can interact and be detected, therefore a fine balance between these two has to be kept.

The ITS consists of six layers of cylindrical silicon detectors with radii from 4 to 43 cm. They are located closely around the beam pipe and are coaxial to it, the layout of the ITS can be seen in Fig. 4.3. The ITS covers the pseudorapidity range of $|\eta| < 0.9$ and full azimuthal coverage.

Silicon Pixel Detector

The track density near the beam pipe is as high as 50 tracks/cm^2, therefore to achieve a good enough spatial resolution, the two innermost layers of the ITS are Silicon Pixel

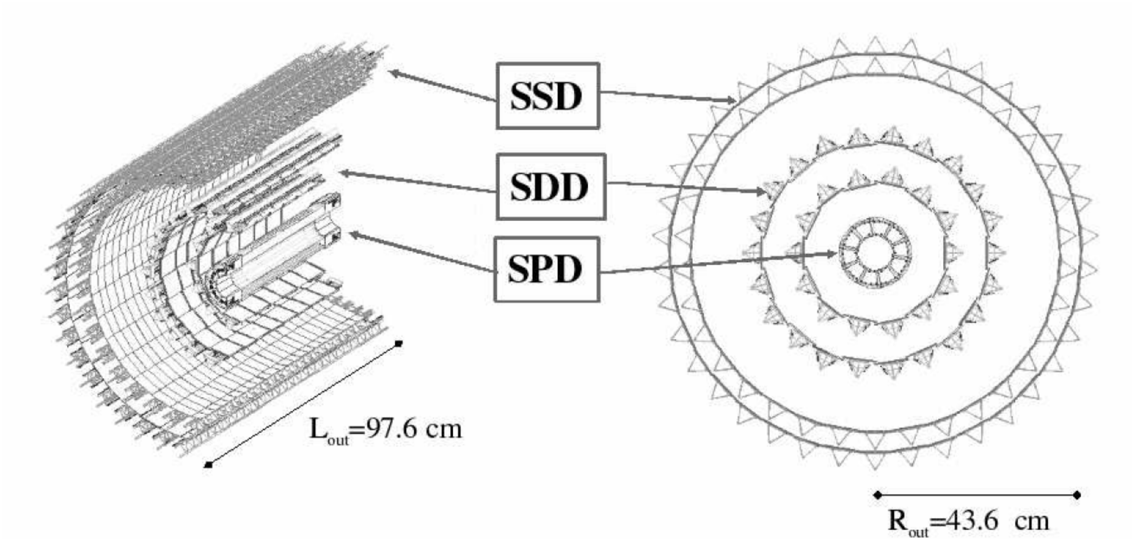

Figure 4.3: Layout of the ITS [13].

Detectors (SPD). They are primarily used for vertex localization and can also be used as triggers. The pseudorapidity range for the first layer of SPD is extended to $|\eta| < 1.98$. The basic element of the SPD is a half-stave. On this half-stave, there is a two dimensional silicon matrix with 256×160 cells. Each cell provides a binary output, if the energy of a particle passing through the cell is higher then a given threshold a signal is produced. When two half-staves are wired together they form a stave. Six staves are then bonded to support structures, two for the inner layer and four for the outer layer. Such an arrangement is called a sector and the full barrel of the SPD is made of ten sectors.

Silicon Drift Detector

For the two middle layers, where the track density is lower (up to 7 tracks/cm^2), Silicon Drift Detectors (SDD) are used. They have analog readout and provide both information about the track position and $\mathrm{d}E/\mathrm{d}x$ measurement for particle identification (as can be seen in Fig. 4.4). Their acceptance in pseudorapidity is $|\eta| < 0.9$. The sensitive part of the detector is split into two drift regions by a central cathode and each drift region has 256 collection anodes.

Silicon Strip Detector

The two outermost layers of the ITS are Silicon Strip Detectors (SSD). They provide a measurement of two the dimensional position of the tracks. This is crucial for matching tracks from the ITS to the tracks from the Time-Projection Chamber. They also provide $\mathrm{d}E/\mathrm{d}x$ measurement for particle identification (as can be seen in Fig. 4.4). The detection modules are 300 μm thick double sided silicon strip detectors with 768 strips on each side.

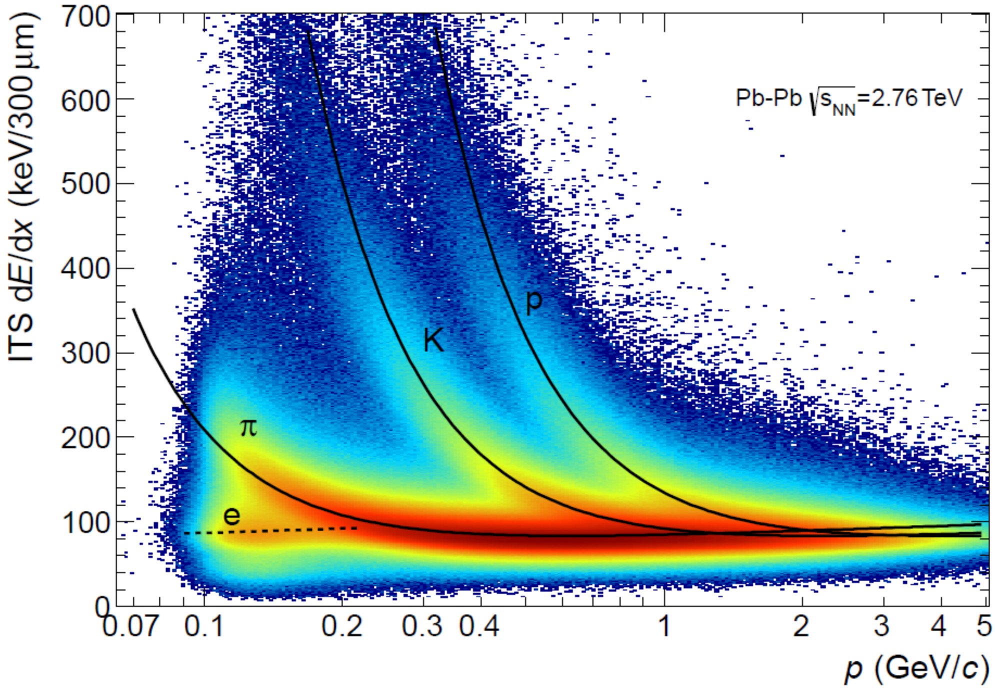

Figure 4.4: dE/dx measurement for the ITS as a function of momentum in Pb–Pb collisions at $\sqrt{s_{NN}} = 2.76$ TeV [17].

4.3.2 Time-Projection Chamber

The Time-Projection Chamber (TPC) is the main tracking detector at central rapidities in ALICE. Together with other detectors it also provides measurement of charged-particle momentum, particle identification (see Fig. 4.5) and vertex determination.

The pseudorapidity range of the TPC for tracks with full radial length is $|\eta| < 0.9$, matching that of ITS and TOF. For reduced track length it is possible to achieve a pseudorapidity range up to $|\eta| = 1.5$, but with reduced momentum resolution. The TPC has a full azimuthal coverage and measures particles with p_t from 0.1 GeV/c up to 100 GeV/c with good resolution (as can be seen in Fig. 4.6).

The TPC has a cylindrical shape with an inner radius (of the active volume) of about 88 cm and the outer radius (of the active volume) of about 250 cm. It is 500 cm long in the beam direction and divided into two halves (250 cm each) by a central electrode, the schematic layout of the TPC cage can be seen in Fig. 4.7. For 2017 measurements the active volume of the detector (90 m^3) is filled with Ne-CO_2-N_2 (90-10-5 divided by 1.05 to normalize) gas mixture. From 2015 to 2016 the fill gas was Ar-CO_2 (88-12) mixture.

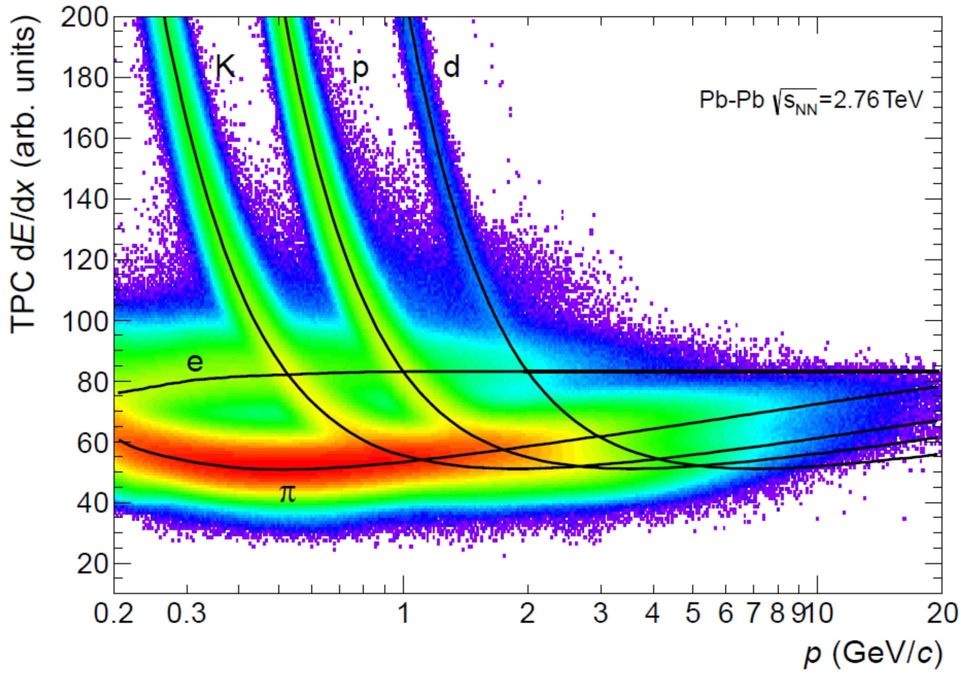

Figure 4.5: d$E/$dx measurement for the TPC as a function of momentum in Pb–Pb collisions at $\sqrt{s_{NN}} = 2.76$ TeV [17].

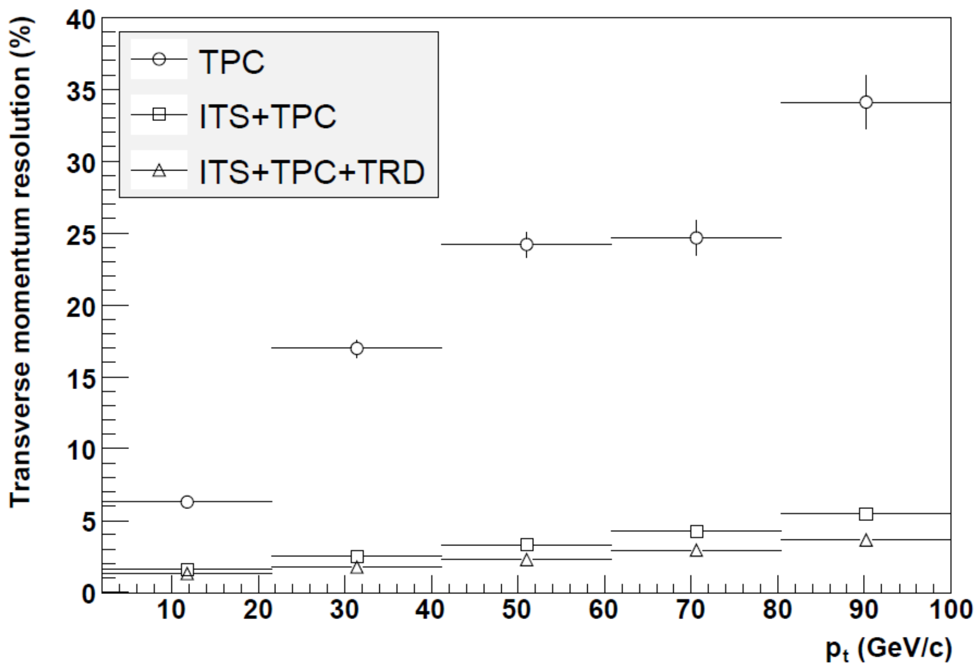

Figure 4.6: Transverse momentum resolution for central barrel detectors: TPC, ITS and TRD (Transition Radiation Detector) [13].

The active volume of the detector is operated at a voltage gradient of approximately 400 V/cm, with the central electrode at 100 kV. Charged particles passing through the detector ionize the working gas. Electrons from primary ionization drift up to 250 cm to the end plates. With the neon mixture the maximum drift time is 90 μs, which is the limiting factor for the measurement rate. The necessary signal amplification and readout is achieved by multi-wire proportional chambers with cathode pad readout, mounted on the end plates. They form 18 trapezoidal sectors, smaller near the center and larger further from the center, on each end plate. The multi-wire proportional chambers are located behind a wire gate. The wire gate stops any electrons from reaching the multi-wire proportional chambers, except for the time when the detector is supposed to take data. It also prevents ions from drifting back to the detector active volume, which would distort the homogeneous electric field.

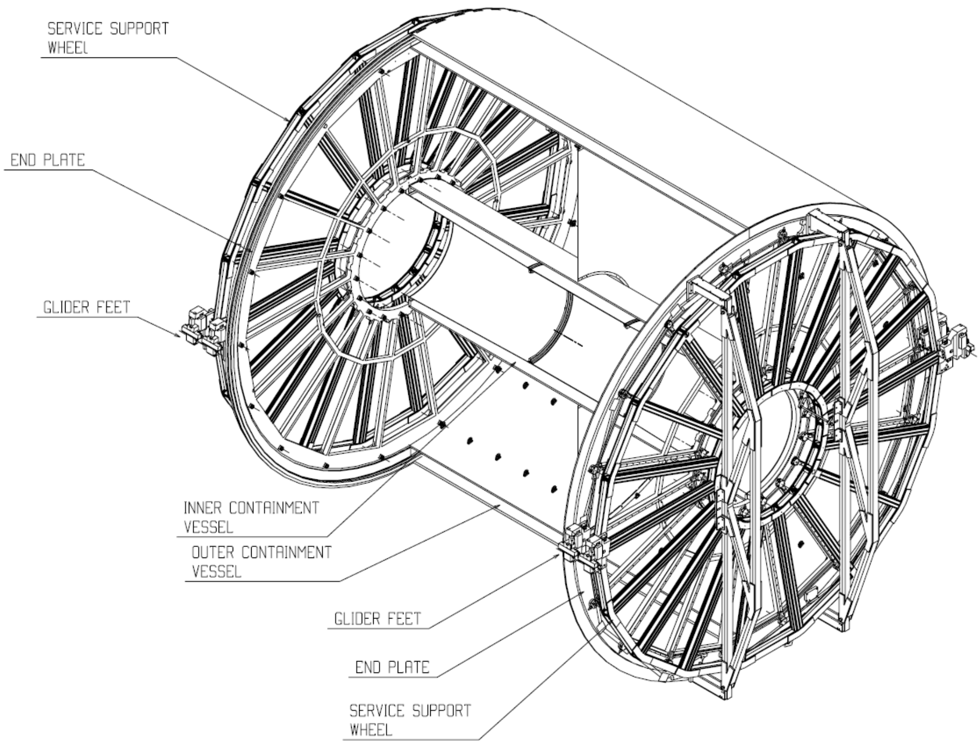

Figure 4.7: Schematic layout of the TPC cage [13].

4.3.3 Time-Of-Flight detector

The main purpose of the Time-Of-Flight (TOF) detector is particle identification, based on particle velocity (see Fig. 4.8), in the intermediate momentum range, below 2.5 GeV/c for pions and kaons and up to 4 GeV/c for protons. It can also be used as a trigger.

The TOF has a full azimuthal coverage and the pseudorapidity coverage is $|\eta| < 0.9$. It has a cylindrical shape with the inner radius of 370 cm and the outer radius of 399 cm. In the beam direction it is 741 cm long (active region).

The TOF is composed out of Multi-gap Resistive-Plate Chambers (MRPC) with 10 gaps of 250 μm. This design ensures a high uniform electric field across the entire active region. Due to the small width of the gaps, the electrons from the primary ionization immediately start an avalanche without any associated drift time. Thus the time delay is caused only by the formation of the avalanche, allowing the intrinsic time resolution to be better then 40 ps. The MRPCs are mounted onto modules which have 5 segments, of different length, in beam direction and 18 sectors in azimuthal angle.

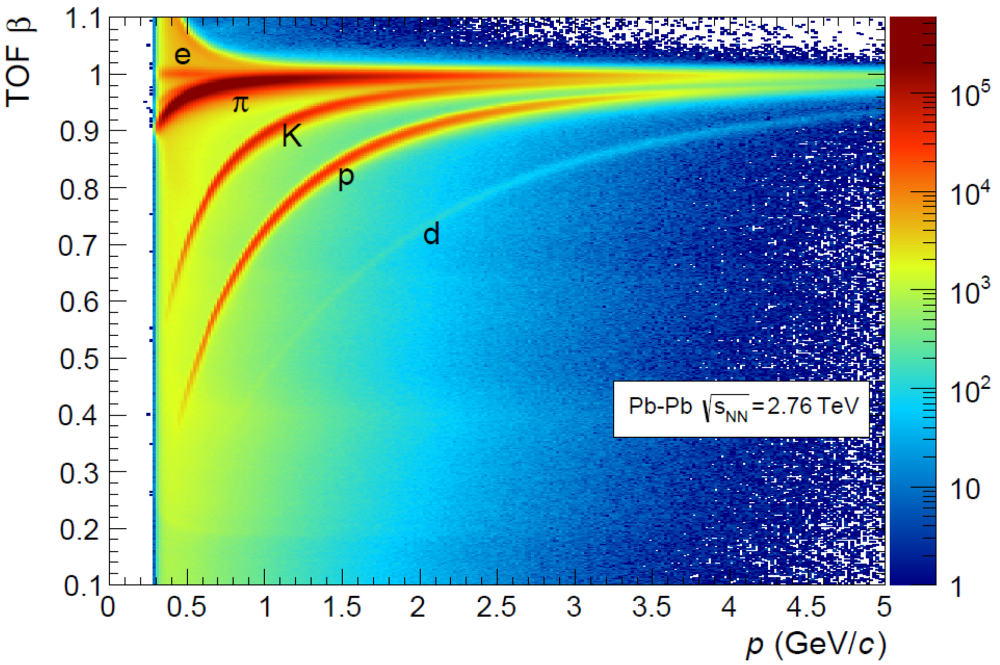

Figure 4.8: Velocity $\beta = \frac{c}{v}$ distribution, measured by TOF, as a function of momentum, measured by TPC, in Pb–Pb collisions at $\sqrt{s_{NN}} = 2.76$ TeV [17].

4.3.4 Muon spectrometer

The muon spectrometer was designed to measure the heavy-quark vector mesons (i.e. ϕ, J/ψ, ψ', Υ, Υ' and Υ'') via their dimuon ($\mu^+\mu^-$) decay channel. Moreover, the unlike-sign dimuon continuum, caused predominantly by the semileptonic decays of open charm and open beauty particles, can be measured up to mass of 10 GeV$/c^2$. The simultaneous measurement of different vector mesons by the same apparatus allows comparison of their production rate and its dependence on different variables.

The pseudorapidity acceptance for the muon spectrometer is $-4.0 < \eta < -2.5$ and full in the azimuthal angle. The spectrometer was build as large as possible, because of that the main source of uncertainty in the dimuon measurements is due to statistic limitations. In addition, a large acceptance close to zero p_t is needed for the J/ψ measurement. This is in particular important for this thesis, because the J/ψ data together with the dimuon continuum measurement were used for studies of signal extraction described in Chap. 6.

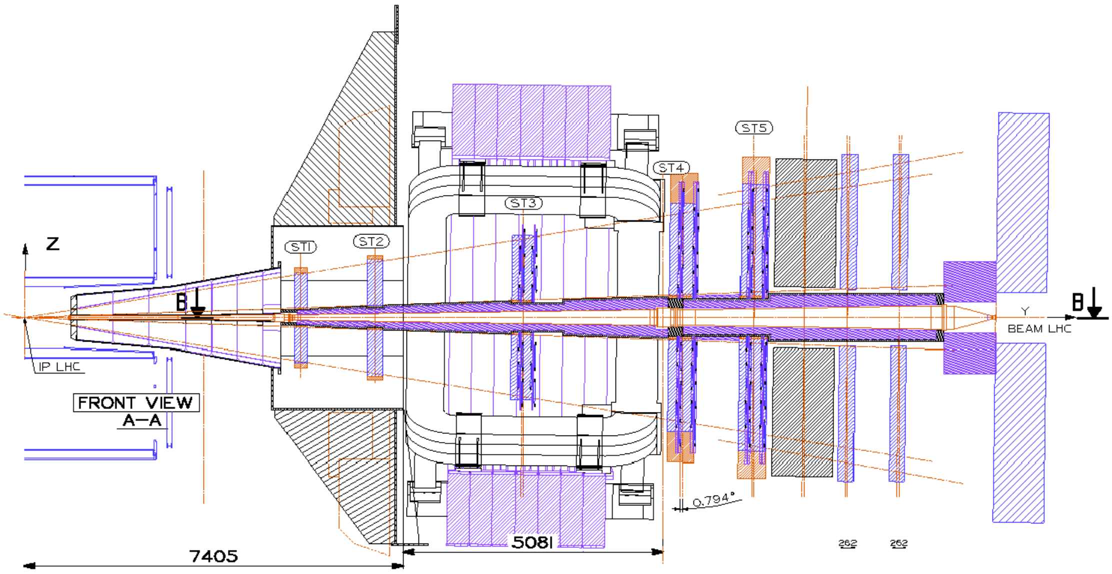

Figure 4.9: The longitudinal layout of the muon spectrometer [13].

The longitudinal layout of the muon spectrometer can be seen in Fig. 4.9. Due to the very high particle multiplicity in Pb-Pb collisions the apparatus of the spectrometer starts with a 4.13 m long passive front filter, made predominantly from carbon and concrete, to stop any hadrons and photons coming from the primary vertex. After that follows a high granularity tracking system composed of 10 planes of multi-wire proportional chambers with cathode pad readout. These are organized in 5 measuring stations ST1-ST5. The ST3 segment is inside a large dipole magnet with integrated magnetic field of 3 Tm, which enables muon momentum measurement. The tracking system is also protected from primary and secondary particles produced at large rapidities by a beam shield constructed out of tungsten, lead and stainless steel. While for the tracking system this shielding is sufficient, for the trigger chambers (located at the back end of the muon spectrometer) an additional 1.2 m long iron muon filter is necessary. Together with the front absorber the muon filter stops all muons with momentum less then 4 GeV$/c$. As mentioned earlier the muon spectrometer ends with 4 planes of trigger chambers. These are constructed out of 4 resistive plate chambers operated in streamer mode and organized into two trigger stations. The trigger chambers are capable to perform a programmable p_t selection in range from approximately 0.5 GeV$/c$ to about 2 GeV$/c$ by the following signals: at least one single muon track above the p_t cut; at least two unlike-sign muon tracks, each of them above the p_t cut; at least two like-sign muon tracks, each of them above the p_t cut.

4.3.5 Zero-Degree Calorimeter

The number of nucleons participating in a collision can be estimated by measuring the energy carried away from the collision by non-interacting (spectator) nucleons in the very forward region. This measurement is provided by two sets of Zero-Degree Calorimeters (ZDC) located 116 m on each side from the interaction point. Each set is composed of a neutron (ZN) and a proton (ZP) calorimeter.

The spectator nucleons are detected through their interaction with a passive material. The showers they produce emit Cherenkov radiation in quartz fibers which also collect the signal and deliver it to photomultiplier tubes (PMTs). The ZN detector serves for detection of neutrons, it is located at a 0° angle relative to the beam axis. The ZP detector serves for detection of protons, it is located externally alongside the beam pipe, because protons are deflected there (unlike neutrons) by the magnetic field of the LHC. To protect the ZDC from radiation damage, both ZN and ZP are placed on lifting platforms to retract them from the measuring region when not in use. The schematic layout of the ZDC can be seen in Fig. 4.10.

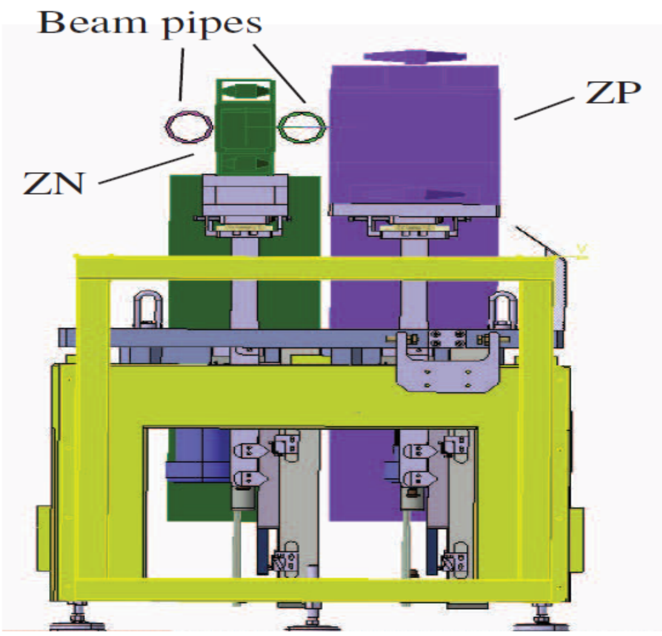

Figure 4.10: Front view of the ZDC [13].

Due to the space limitation for the ZN a very dense wolfram alloy is used as the passive material. For the ZP the space limitations are not so strict and furthermore the protons are more spread out then the neutrons, therefore the ZP is larger and constructed out of less dense brass.

4.3.6 V0 detector

V0 is a small angle detector consisting of two arrays of scintillator counters called V0A and V0C. They cover the pseudorapidity range of $2.8 < \eta_{V0A} < 5.1$ and $-3.7 < \eta_{V0C} < -1.7$ respectively. The V0A is located 340 cm from the interaction point in the direction to the ATLAS experiment and the V0C is mounted on the hadronic absorber of the muon spectrometer, located 90 cm from the interaction point in the direction to the CMS experiment. Each scintillator array consists of 32 cells forming 4 concentric rings subdivided into 8 azimuthal sectors. The signal from the BC404 scintillating material is transported by wave-length shifting fibers to the photo-multiplier system. Photos of the V0A and V0C detectors can be seen in Fig. 4.11.

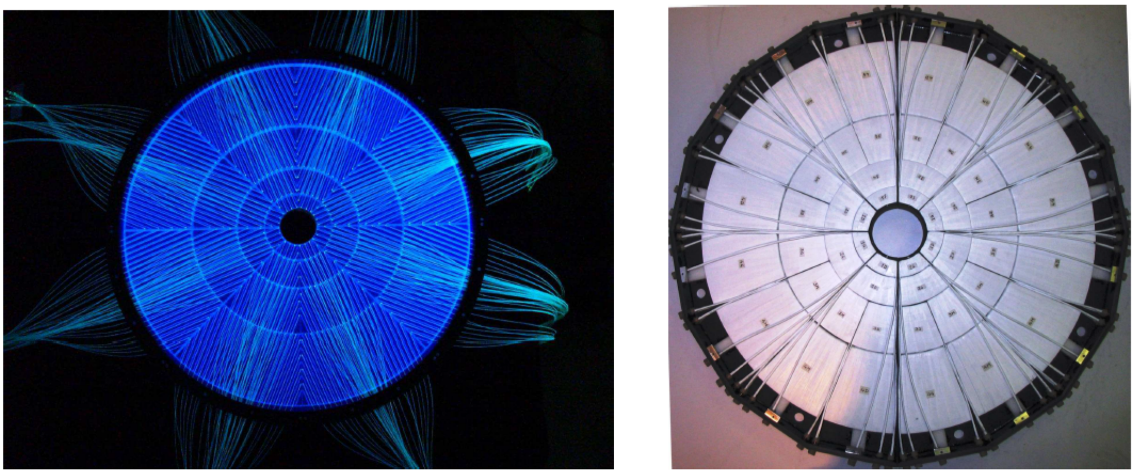

Figure 4.11: Front view of the V0A (left) and V0C (right) [13].

The main purpose of the V0 detector is triggering. It serves as a minimum-bias trigger for the central-barrel detectors. Because the number of detected particles in the V0 arrays is linearly dependent on the number of primary particles, the V0 also serves as a centrality trigger via a multiplicity measurement. Moreover, the V0 can be used to eliminate false events caused by interactions of accelerated protons or ions with the residual gas particles in the vacuum of the beam line. Furthermore, the V0C can help to reject a large part of false signals in the muon spectrometer trigger chambers. Finally, the V0 detector also provides luminosity measurements.

4.3.7 The ALICE Diffractive detector

The ALICE Diffractive (AD) detector is a small scintillating detector installed in the very forward region. It consists of two main stations (one such station can be seen in Fig. 4.12), each having 2 layers of 4 plastic scintillator pads. The ADA station is located 16.95 m from the interaction point towards the ATLAS experiment and the ADC station is located 19.57 m from the interaction point towards the CMS experiment. They cover the pseudorapidity range $4.8 < \eta_{ADA} < 6.3$ and $-7.0 < \eta_{ADC} < -4.9$, respectively. Each of the 16 pads has approximate dimensions of $22 \times 22 \times 2.5$ cm^3. Particles passing through the detector produce light in the BC404 scintillating material, which is then collected by wave-length shifting (WLS) bars located on the sides of the pads. This signal is then transferred by transparent optical fibers to photomultiplier tubes.

The AD detector was installed in the Long Shutdown 1 between Run 1 (2009-2013) and Run 2 (2015-2018). It helps to increase the sensitivity to diffractive masses below 10 GeV$/c^2$. Furthermore, the AD detector can be used as a veto trigger for UPC events to suppress background.

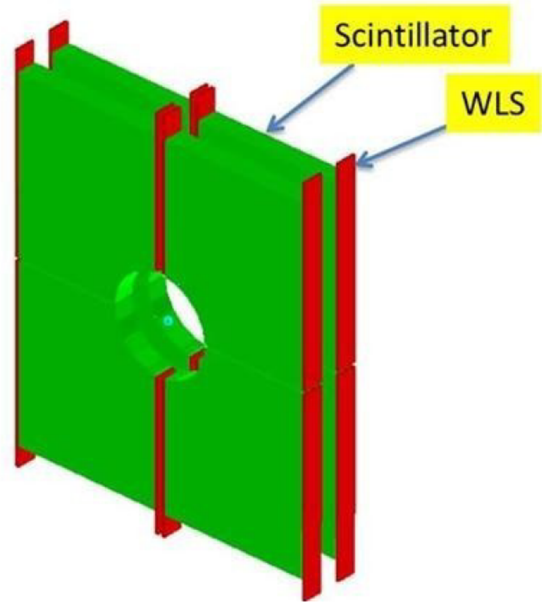

Figure 4.12: Schematic layout of the AD detector [14].

4.3.8 The trigger and data acquisition systems

Trigger system

The collision rate at the LHC can go up to 600 million inelastic events per second [18]. The detectors and associated electronics are not able to read out and store such huge amount of data. Moreover, only some of these events are of interest to us, and therefore we select only certain events to be read out and stored.

The ALICE Central Trigger Processor (CTP) was designed to achieve this, based on inputs from detectors called triggers. The fast triggers are divided into two categories: Level 0 (L0) trigger, for which the CTP decision reaches the detector at 1.2 μs, but does not contain all the trigger inputs, and Level 1 (L1) trigger, which arrives at 6.5 μs with the remaining inputs. The final trigger level is Level 2 (L2) and it arrives at 88 μs. It waits for the past-future protection, which prevents events from being spoiled by pile-up.

The CTP needs 100 ns to make a decision, the rest of the time delay is caused by detector delays and transferring the signal through cables. There is a total of 60 triggers divided in the three categories as follows: 24 L0 triggers, 24 L1 triggers and 12 L2 triggers. All the triggers used for UPC events are L0 triggers.

Data Acquisition

The Data AcQuisition (DAQ) System was designed to collect measured data from the ALICE sub-detectors and deliver them to the main data storage center. It can handle a bandwidth of 1.25 GB/s.

When the Central Trigger Processor (CTP) accepts an event, it sends a signal through a Local Trigger Unit (LTU), which uses as an interface a Timing, Trigger and Control (TTC) system. The data measured by the detector are transferred by the Front-End Read-Out (FERO) electronics to the Detector Data Links (DDL).

These data are then send to the DAQ Readout Receiver Cards (D-RORC), which are hosted by the Local Data Concentrators (LDC). Each LDC, which are commodity PCs, can host several D-RORCs writing data to the LDC memory. These data are then assembled by the LDCs into sub-events.

The LDCs transport the sub-events to the Global Data Collectors (GDC), also commodity PCs, which build the complete events. The LDCs do not communicate with each other, the Event-Destination Manager (EDM) informs the LDCs about the GDCs availability.

The HLT (see Sec. 4.3.8) receives all the relevant data via DDLs to its HLT Readout Receiver Card (H-RORC) and Front-End Processors (FEP). All the decisions and data generated by the HLT are then sent via DDLs to dedicated LDCs.

During a run period the GDC stores files of fixed size to the Transient Data Storage (TDS). And finally, the TDS movers (TDSM) transport the data from TDS to the the Permanent Data Storage (PDS). The architecture of the DAQ system can be seen in Fig. 4.13.

High-Level Trigger

To further minimize the amount of data produced by the ALICE sub-detectors, which has to be read out and stored, an online processing is done by the High-Level Trigger (HLT). The HLT consists of 1000 multi-processor PC farm operating in a 6 layer scheme.

In the first layer the raw data from all ALICE detectors are received. The second layer extracts hits and clusters, the third layer reconstructs the event individually for each detector. The fourth layer combines information from all the detectors and reconstructs the entire event. Based on this information the fifth layer selects events or regions of interest

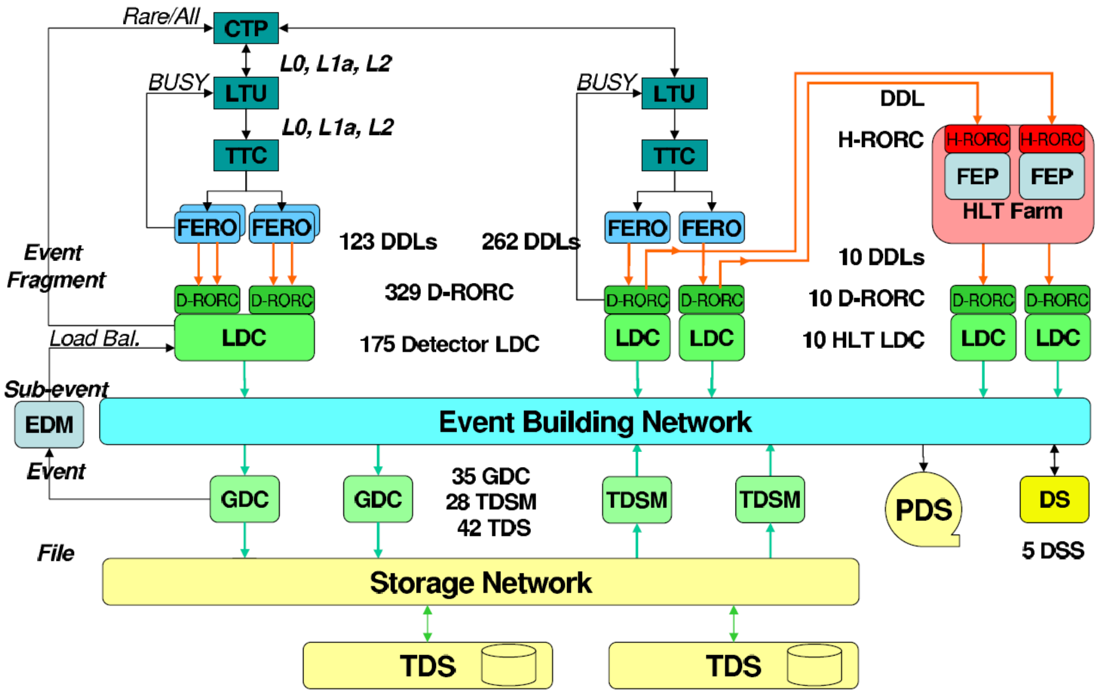

Figure 4.13: Architecture of the DAQ system [13].

according to given physics criteria. Finally, in the sixth layer this data is submitted to complex data compression algorithms.

AliRoot framework

AliRoot is the ALICE offline framework. It is an object-oriented environment based on the ROOT system together with the AliEn system, which enables it to connect to the computing grid. It is entirely written in C++, except few external programs, hidden from users, which are written in FORTRAN.

AliRoot was designed with focus on re-usability and modularity. As a result of that, it is possible to exchange well defined parts of the program with small or no impact to the rest of the code. AliRoot contains Monte Carlo (MC) generators, simulations of the ALICE detectors and electronics, necessary analysis tools and much more. This allows the AliRoot framework to be used for simulation, alignment, calibration, reconstruction, visualization and analysis of the experimental data.

Chapter 5

Previous UPC measurements with ALICE

Results of two papers on UPC measurements with ALICE are presented in this chapter. The first paper reports results on coherent J/ψ photoproduction in ultra-peripheral Pb-Pb collisions at $\sqrt{s_{NN}} = 2.76$ TeV, while the other focus on charmonium and e^+e^- pair photoproduction at mid-rapidity in ultra-peripheral Pb-Pb collisions at $\sqrt{s_{NN}} = 2.76$ TeV. Note that in both papers the signal extraction is a major contributor to the total systematic uncertainty of the measurement, as shown in Tab. 5.1 and Tab. 5.2.

5.1 Coherent J/ψ photoproduction in ultra-peripheral Pb-Pb collisions at $\sqrt{s_{NN}} = 2.76$ TeV

Results of coherent J/ψ photoproduction in ultra-peripheral Pb-Pb collisions at $\sqrt{s_{NN}} = 2.76$ TeV [19] are presented in the following text.

The measurement of vector meson production in heavy-ion collisions was performed in order to probe nuclear gluon distribution functions in the low-x region. A J/ψ produced at rapidity y is sensitive to gluon distribution at

$$x = \frac{M^2_{\mathrm{J}/\psi}}{W^2_{\pm}} = \frac{M_{\mathrm{J}/\psi}}{\sqrt{s_{NN}}} e^{\mp y}, \tag{5.1}$$

here $M_{\mathrm{J}/\psi}$ is the invariant mass of the J/ψ. For the J/ψ mesons studied in this paper, which were produced in the forward-rapidity region $-3.6 < y < -2.6$, the corresponding values of Bjorken x are approximately $x \approx 10^{-5}$ and $x \approx 10^{-2}$. The two possible results are due to the fact, that both Pb ions can be the source of the virtual γ photon. According to the STARLIGHT Monte Carlo simulations the $x \approx 10^{-5}$ contributes with 6 % to the total cross section, while the $x \approx 10^{-2}$ is the dominant contribution to the total cross section with 94 %.

As mentioned above the analysis presented in this paper was made on a sample of events from the 2011 Pb-Pb run at $\sqrt{s_{NN}} = 2.76$ TeV. The sample consists of dimuon decays of the J/ψ in the forward-rapidity region. The analysis is focused on the coherent production, this is achieved by a transverse momentum condition for the J/ψ $p_t < 0.3$ GeV/c.

The events were selected by the FUPC trigger for UPC events where a dimuon pair is produced. The integrated luminosity for this trigger was approximately 55 mb^{-1}. The FUPC trigger selects dimuon decays of the J/ψ and a muon continuum produced by the two-photon interactions ($\gamma\gamma \rightarrow \mu^+\mu^-$). This is achieved by the following criteria:

1. A single muon above a 1 GeV/c p_t-threshold.
2. At least one hit in the V0C detector. In addition, V0C vetoes the beam-gas events which could produce a trigger in the muon arm.
3. No hits in the V0A detector to reject hadronic collisions.

The offline selection criteria were chosen so that only events with two tracks in the muon spectrometer and very low J/ψ p_t were selected. These are the applied selection criteria (number of events left after the selection):

1. Two reconstructed tracks in the muon arm (432 422 events).
2. Due to the multiple scattering in the front absorber, the distance between the vertex and the track extrapolated to the vertex transverse plane (DCA) distribution of the tracks coming from the interaction vertex can be described by a Gaussian function, whose width depends on the absorber material and is proportional to $1/p$, where p is the muon momentum. The beam induced background does not follow this trend and was rejected by applying a cut on the product $p\times$DCA, at 6 times the standard deviation (26,958 events).
3. At least one of the muon track candidates was required to match a trigger track above the 1 GeV/c p_t-threshold in the spectrometer trigger chambers (10 172 events).
4. Both tracks pseudorapidities within the range $-3.7 < \eta < -2.5$, to match the V0C acceptance (5 100 events).
5. The tracks exit from the absorber in the range 17.5 cm $< R_{abs} <$ 89.5 cm, limiting the two parts of the absorber covering the angular acceptance of the spectrometer (R_{abs} is the radial coordinate of the track at the end of the front absorber) (5 095 events).

6. Dimuon rapidity to be in the range $-3.6 < y < -2.6$, which ensured that the edges of the overlap between V0C and the muon spectrometer were avoided (4 919 events).

7. Two tracks with opposite charges (3 209 events).

8. Only events with a neutron ZDC signal below 6 TeV on each side were kept. In the present data sample, this cut does not remove any events with a J/ψ produced with a transverse momentum below 0.3 GeV/c, but reduces hadronic contamination at higher p_t (817 events).

9. Dimuons to have $p_t < 0.3$ GeV/c and invariant mass $2.8 < M_{inv} < 3.4$ GeV/c^2 (122 events).

10. V0 offline timing compatible with crossing beams (117 events).

The acceptance and efficiency of the J/ψ reconstruction were determined from a large sample of coherent and incoherent J/ψ events generated by STARLIGHT and folded with the Monte Carlo simulations of the ALICE detectors. The obtained values of the product of the acceptance and efficiency corrections $(\mathrm{Acc}\times\varepsilon)_{J/\psi}$ were 16.6 % and 14.3 % for coherent and incoherent J/ψ respectively.

The invariant mass distribution of opposite sign muon pairs in the interval $2.2 < M_{inv} < 4.6$ GeV/c^2 can be seen in Fig. 5.1. A clear J/ψ peak is visible on top of the dimuon continuum.

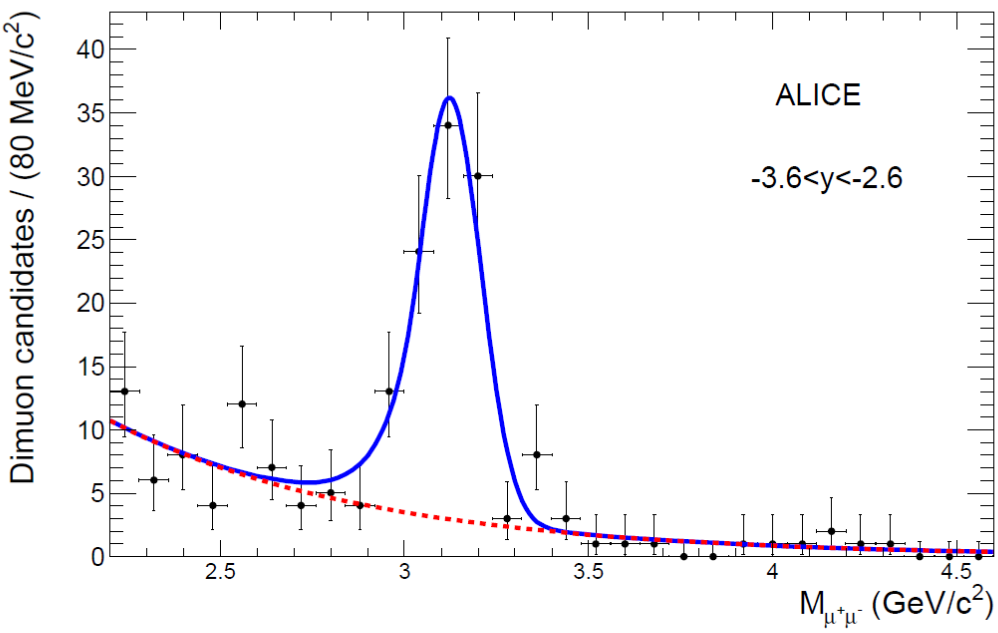

Figure 5.1: Invariant mass distribution for the selected dimuon events [19].

The J/ψ yield was obtained by fitting the invariant mass spectrum with an exponential function describing the background and a Crystal Ball function to extract the signal. The parameters of the Crystal Ball function were fixed on values obtained from simulations. The extracted number of J/ψs was $N_{yield} = 96 \pm 12(\mathrm{stat}) \pm 6(\mathrm{sys})$. The systematic error was obtained by varying the Crystal Ball parameters.

The total number of coherent J/ψs is calculated as

$$N^{coh}_{\mathrm{J}/\psi} = \frac{N_{yield}}{1 + f_I + d_D}, \tag{5.2}$$

where f_D is the fraction of J/ψ mesons coming from the decay of $\psi' \to \mathrm{J}/\psi +$ anything and f_I is the fraction of incoherent events in the $p_t < 0.3$ GeV$/c$ region. The resulting number of J/ψs is $N^{coh}_{\mathrm{J}/\psi} = 75 \pm 10(\mathrm{stat})^{+7}_{-11}(\mathrm{sys})$.

The differential cross section is then given by

$$\frac{\mathrm{d}\sigma^{coh}_{\mathrm{J}/\psi}}{\mathrm{d}y} = \frac{N^{coh}_{\mathrm{J}/\psi}}{(\mathrm{Acc} \times \varepsilon)_{\mathrm{J}/\psi} \cdot \varepsilon_{trig} \cdot BR(\mathrm{J}/\psi \to \mu^+\mu^-) \cdot \mathscr{L}_{int} \cdot \Delta y}, \tag{5.3}$$

where $N^{coh}_{\mathrm{J}/\psi}$ is the number of produced coherent J/ψs, $(\mathrm{Acc}\times\varepsilon)_{\mathrm{J}/\psi}$ is the product of the acceptance and efficiency of the muon spectrometer, ε_{trig} is the V0 trigger efficiency, $BR(\mathrm{J}/\psi \to \mu^+\mu^-) = 5.93$ % is the branching ratio for the dimuon J/ψ decay channel, $\mathscr{L}_{int}$ is the total integrated luminosity and $\Delta y = 1$ is the rapidity interval bin size. Due to problems with obtaining a precise value for the V0 trigger efficiency a QED continuum pair production was used for normalization instead of Eq. 5.3.

The events selected by the FUPC trigger also contain $\gamma\gamma \to \mu^+\mu^-$ events, which are very similar to the J/ψ decays in terms of kinematics. The cross section for $\gamma\gamma \to \mu^+\mu^-$ can be written in a similar way to Eq. 5.3. The fraction of these two is then independent of luminosity and trigger efficiency and can be written as

$$\frac{\mathrm{d}\sigma^{coh}_{\mathrm{J}/\psi}}{\mathrm{d}y} = \frac{1}{BR(\mathrm{J}/\psi \to \mu^+\mu^-)} \cdot \frac{N^{coh}_{\mathrm{J}/\psi}}{N_{\gamma\gamma}} \cdot \frac{(\mathrm{Acc} \times \varepsilon)_{\gamma\gamma}}{(\mathrm{Acc} \times \varepsilon)_{\mathrm{J}/\psi}} \cdot \frac{\sigma_{\gamma\gamma}}{\Delta y}, \tag{5.4}$$

where $N_{\gamma\gamma}$ is the number of events in the invariant mass intervals $2.2 < M_{inv} < 2.6$ GeV$/c^2$ ($N_{\gamma\gamma} = 43 \pm 7(\mathrm{stat})$) and $3.5 < M_{inv} < 6$ GeV$/c^2$ ($N_{\gamma\gamma} = 15 \pm 4(\mathrm{stat})$), to avoid contamination from the J/ψ peak. The $\sigma_{\gamma\gamma}$ was determined from STARLIGHT simulations. The $(\mathrm{Acc} \times \varepsilon)_{\gamma\gamma}$ was obtained from STARLIGHT simulations folded with the detector response simulation. The sources of systematic uncertainties are summarized in Tab. 5.1.

The final differential cross section for coherent J/ψ photoproduction is $\mathrm{d}\sigma^{coh}_{\mathrm{J}/\psi}/\mathrm{d}y = (1.00 \pm 0.18(\mathrm{stat})^{+0.24}_{-0.26}(\mathrm{sys}))$ mb. This result is compared with predictions made by various models (see Fig. 5.2). Best agreement is seen for models which include nuclear gluon shadowing.

Source	Value
Theoretical uncertainty in $\sigma_{\gamma\gamma}$	20 %
Coherent signal extraction	$^{+9\ \%}_{-14\ \%}$
Reconstruction efficiency	6 %
RPC trigger efficiency	5 %
J/ψ acceptance calculation	3 %
Two-photon e^+e^- background	2 %
Branching ratio	1 %
Total	$^{+24\ \%}_{-26\ \%}$

Table 5.1: Summary of the contributions to the systematic uncertainty for the integrated J/ψ cross section measurement. The error for the coherent signal extraction includes the systematic error in the fit of the invariant mass spectrum and the systematic errors on f_D and f_I [19].

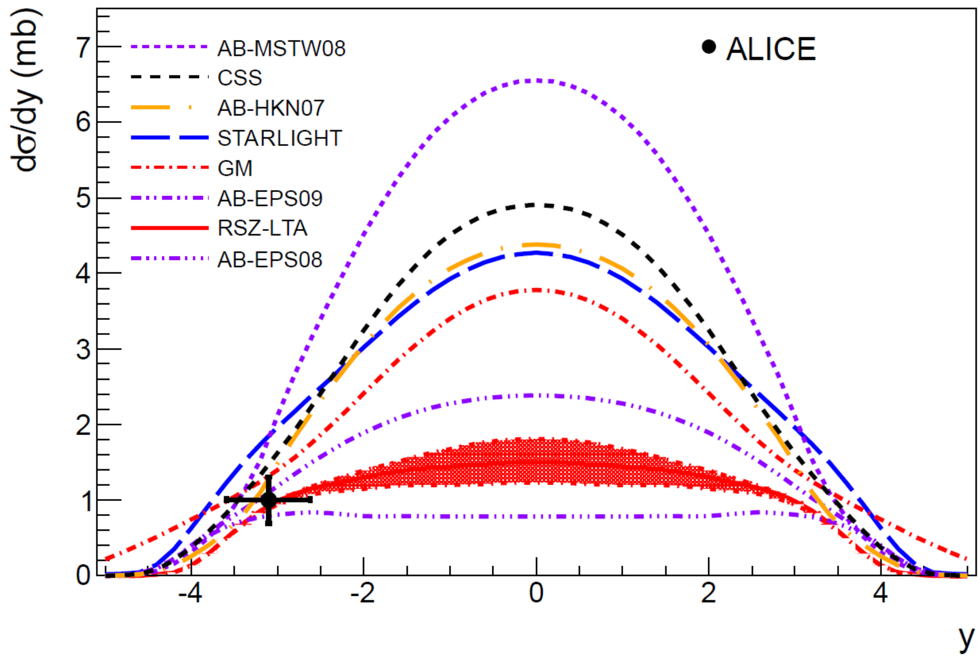

Figure 5.2: Rapidity distribution of the measured coherent differential cross section of J/ψ photoproduction in ultra-peripheral Pb-Pb collisions at $\sqrt{s_{NN}} = 2.76$ TeV. The error is the quadratic sum of the statistical and systematic errors. The theoretical predictions are also shown [19].

5.2 Charmonium and e^+e^- pair photoproduction at mid-rapidity in ultra-peripheral Pb-Pb collisions at $\sqrt{s_{NN}} = 2.76$ TeV

Results of charmonium and e^+e^- pair photoproduction at mid-rapidity in ultra-peripheral Pb-Pb collisions at $\sqrt{s_{NN}} = 2.76$ TeV [20] are presented in the following text.

This paper studies both coherent and incoherent J/ψ production at mid rapidity $|y| < 0.9$, thus probing gluon distribution functions at $x \approx 10^{-3}$. Moreover, two-photon production of dilepton pairs is studied, because when the coupling constant ($Z\sqrt{\alpha}$) is large, higher-order terms may become important in QED calculations. With energies provided by the LHC these effects can be evaluated.

The events analyzed in this paper were selected by the dedicated barrel ultra-peripheral collision trigger (BUPC) from the 2011 Pb-Pb run. This trigger selects events with two tracks in an otherwise empty detector by applying the following criteria:

1. At least two hits in the SPD detector.
2. The number of fired pads (N_{on}) in the TOF detector in the range $2 \leq N_{on} \leq 6$, with at least two of them with a difference in azimuth, $\Delta\phi$, in the range $150° \leq \Delta\phi \leq 180°$.
3. No hits in the V0A and no hits in the V0C detectors.

In total approximately $6.5 \cdot 10^6$ events were selected. This corresponds to an integrated luminosity $\mathscr{L}_{int} = 23.0^{+0.7}_{-1.2}$ μb^{-1}.

In the offline analysis the following selection criteria (number of events left after the selection) were applied to 6 507 692 events:

1. The number of reconstructed tracks $1 \leq N_{TRK} \leq 10$, where a track is defined with loose criteria (2 311 056).
2. A reconstructed primary vertex (1 972 231).
3. Only two good tracks passing tighter quality cuts (436 720).
4. At least one of the two good tracks selected in 3 with $p_t \geq 1$ GeV/c, this cut reduces the background (46 324).
5. The V0 trigger required no signal within a time window of 25 ns around the collision time (46 183).
6. The dE/dx for the two tracks is compatible with that of electrons or muons, it is worth noting that the TPC resolution does not allow to distinguish between muons and charged pions (45 518).

7. The two tracks have either the same or opposite charges, depending on the analysis (31 529).

8. Invariant mass $2.2 < M_{inv} < 6$ GeV$/c^2$ (4 542).

A first sample was enriched with coherent events by applying a $p_t < 300$ MeV$/c$ cut for dielectrons and $p_t < 200$ MeV$/c$ for dimuons, resulting in total number of 746 dielectron and 1301 dimuon coherent event candidates. A second sample was enriched with incoherent events by applying a $p_t > 300$ MeV$/c$ cut for dielectrons and $p_t > 200$ MeV$/c$ for dimuons, resulting in total number of 278 dielectron and 1748 dimuon incoherent event candidates.

The acceptance and efficiency of both coherent and incoherent J$/\psi$ event reconstruction were calculated from STARLIGHT generated events folded with the ALICE detector simulations. The average values for the product of acceptance and efficiency for J$/\psi \rightarrow e^+e^-(\mu^+\mu^-)$ were found to be 2.71 (4.57) % and 1.8 (3.19) % for coherent and incoherent J$/\psi$ respectively. The invariant mass distribution for all the events combined can be seen in Fig. 5.3

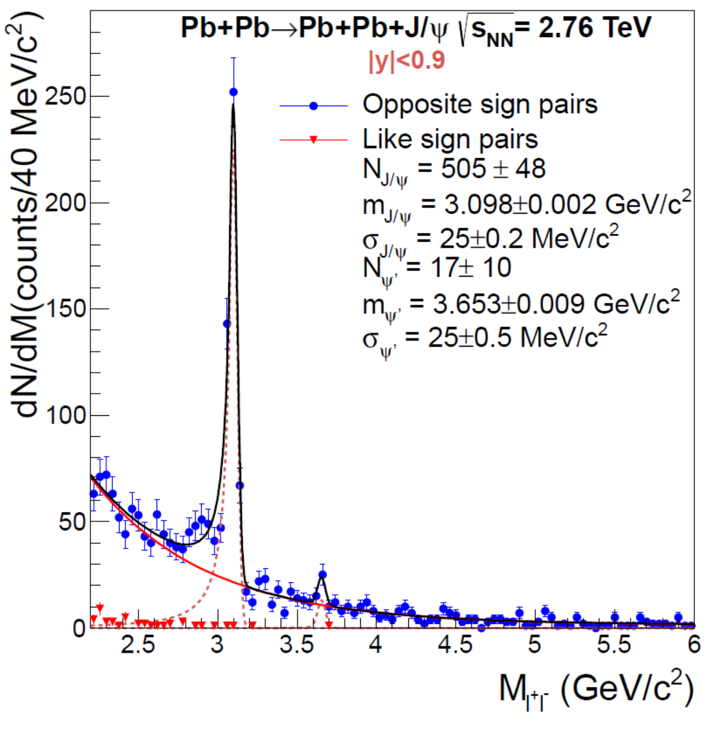

Figure 5.3: Invariant mass distribution for the selected dielectron and dimuon events [20].

The J$/\psi$ yield was obtained by fitting the invariant mass spectrum with an exponential function to describe the background and a Crystal Ball function to extract the signal. The Crystal Ball parameters (α_{CB}, n) were left free for the coherent sample, giving a good agreement with those obtained from simulations, and fixed to values obtained from simulations for the incoherent sample. The background in the incoherent sample was fitted by a combination of an exponential function and a fifth order polynomial.

The yield obtained from the fit of the coherent sample is $N_{yield} = 265 \pm 40(\mathrm{stat}) \pm 12(\mathrm{sys})$ for the $\mathrm{J}/\psi \to e^+e^-$ channel and $N_{yield} = 291 \pm 18(\mathrm{stat}) \pm 4(\mathrm{sys})$ for the $\mathrm{J}/\psi \to \mu^+\mu^-$ channel. From Eq. 5.2 the number of coherent J/ψs is calculated to be $N^{coh}_{\mathrm{J}/\psi}(e^+e^-) = 212 \pm 32(\mathrm{stat})^{+14}_{-13}(\mathrm{sys})$ and $N^{coh}_{\mathrm{J}/\psi}(\mu^+\mu^-) = 255 \pm 16(\mathrm{stat})^{+14}_{-13}(\mathrm{sys})$. Then the J/ψ differential cross section is calculated from Eq. 5.3, the rapidity interval bin size is $\Delta y = 1.8$, as $\mathrm{d}\sigma^{coh}_{\mathrm{J}/\psi}/\mathrm{d}y = (3.19 \pm 0.50(\mathrm{stat})^{+0.45}_{-0.31}(\mathrm{sys}))$ mb for electrons and $\mathrm{d}\sigma^{coh}_{\mathrm{J}/\psi}/\mathrm{d}y = (2.27 \pm 0.14(\mathrm{stat})^{+0.30}_{-0.20}(\mathrm{sys}))$ mb for muons. Because these results are statistically independent, the weighted average can be calculated, giving $\mathrm{d}\sigma^{coh}_{\mathrm{J}/\psi}/\mathrm{d}y = (2.38^{+0.34}_{-0.24}(\mathrm{stat}+\mathrm{sys}))$ mb.

The results for incoherent cross section are obtained in a similar way. The obtained yields are $N_{yield} = 61 \pm 14(\mathrm{stat})^{+16}_{-7}(\mathrm{sys})$ for the $\mathrm{J}/\psi \to e^+e^-$ channel and $N_{yield} = 91 \pm 15(\mathrm{stat})^{+7}_{-5}(\mathrm{sys})$ for the $\mathrm{J}/\psi \to \mu^+\mu^-$ channel. By applying the equivalent of Eq. 5.2 for incoherent events we obtain $N^{incoh}_{\mathrm{J}/\psi} = 39 \pm 9(\mathrm{stat})^{+10}_{-5}(\mathrm{sys})$ with corresponding $\mathrm{d}\sigma^{incoh}_{\mathrm{J}/\psi}/\mathrm{d}y = (0.87 \pm 0.20(\mathrm{stat})^{+0.26}_{-0.14}(\mathrm{sys}))$ mb for the dielectron decay and $N^{incoh}_{\mathrm{J}/\psi} = 81 \pm 13(\mathrm{stat})^{+8}_{-6}(\mathrm{sys})$ with corresponding $\mathrm{d}\sigma^{incoh}_{\mathrm{J}/\psi}/\mathrm{d}y = (1.03 \pm 0.17(\mathrm{stat})^{+0.15}_{-0.12}(\mathrm{sys}))$ mb for the dimuon decay.

The $N_{\gamma\gamma}$ yield was obtained by fitting the invariant mass distribution in intervals $2.2 < M_{inv} < 2.6$ GeV/c^2 ($N^{e^+e^-}_{\gamma\gamma} = 186 \pm 13(\mathrm{stat}) \pm 4(\mathrm{sys})$) and $3.7 < M_{inv} < 10$ GeV/c^2 ($N^{e^+e^-}_{\gamma\gamma} = 93 \pm 10(\mathrm{stat}) \pm 4(\mathrm{sys})$), to avoid contamination from the J/ψ peak. The integrated luminosity for this analysis was $\mathscr{L}_{int} = 21.7^{+0.7}_{-1.1}$ μb^{-1} and the cut number 4 on p_t was removed. The resulting cross sections are $\mathrm{d}\sigma^{e^+e^-}_{\gamma\gamma}/\mathrm{d}y = (154 \pm 11(\mathrm{stat})^{+17}_{-11}(\mathrm{sys}))$ μb for the lower invariant mass interval and $\mathrm{d}\sigma^{e^+e^-}_{\gamma\gamma}/\mathrm{d}y = (91 \pm 10(\mathrm{stat})^{+11}_{-8}(\mathrm{sys}))$ μb for the higher invariant mass interval. The cross section for the $\gamma\gamma \to \mu^+\mu^-$ process was not studied due to possible contamination with pions. Summary of all contributions to the systematic error for every calculated cross section can be seen in Tab. 5.2.

In Fig. 5.4 a) the differential cross section of coherent J/ψ photoproduction is compared with calculations from six different models. The presented results are in good agreement with models which incorporate nuclear gluon shadowing.

In Fig. 5.4 b) the differential cross section of incoherent J/ψ photoproduction is compared with calculations from three different models. None of these models is in agreement with the obtained results, but STARLIGHT predicts a correct incoherent to coherent ratio.

If the statistical and systematic errors are added in quadrature the measurement of the $\gamma\gamma$ cross section is compatible with the STARLIGHT prediction within 1.0 and 1.5 sigma for the high and low invariant mass intervals respectively. This implies that models predicting a strong contribution of higher-order terms (not the case of STARLIGHT) to the cross section are not favored.

Source	Coherent	Incoherent	$\gamma\gamma$ (low)	$\gamma\gamma$ (high)
Luminosity	${}^{+5\ \%}_{-3\ \%}$	${}^{+5\ \%}_{-3\ \%}$	${}^{+5\ \%}_{-3\ \%}$	${}^{+5\ \%}_{-3\ \%}$
Trigger dead time	± 2.5 %	± 2.5 %	± 2.5 %	± 2.5 %
Signal extraction	${}^{+7\ \%}_{-6\ \%} \left({}^{+6\ \%}_{-5\ \%}\right)$	${}^{+26.5\ \%}_{-12.5\ \%} \left({}^{+9\ \%}_{-8\ \%}\right)$	± 1 %	± 4 %
Trigger efficiency	${}^{+3.8\ \%}_{-9.0\ \%}$	${}^{+3.8\ \%}_{-9.0\ \%}$	${}^{+3.8\ \%}_{-9.0\ \%}$	${}^{+3.8\ \%}_{-9.0\ \%}$
(Acc$\times\varepsilon$)	± 2.5 %(± 1 %)	± 6.5 %(± 3.5 %)	± 0.3 %	± 0.5 %
$\gamma\gamma \to e^+e^-$ background	${}^{+4\ \%}_{-0\ \%}$	${}^{+4\ \%}_{-0\ \%}$	${}^{+4\ \%}_{-0\ \%}$	${}^{+4\ \%}_{-0\ \%}$
e/μ separation	± 2 %	± 2 %	± 1.7 %	± 4 %
Branching ratio	± 1 %	± 1 %	-	-
Neutron number cut	${}^{+2.5\ \%}_{-0\ \%}$	-	-	-
Hadronic J/ψ	-	${}^{+0\ \%}_{-5\ \%} \left({}^{+0\ \%}_{-3\ \%}\right)$	-	-
Total	${}^{+14.0\ \%}_{-9.6\ \%} \left({}^{+13.4\ \%}_{-8.8\ \%}\right)$	${}^{+29.4\ \%}_{-16.6\ \%} \left({}^{+14.5\ \%}_{-11.7\ \%}\right)$	${}^{+10.8\ \%}_{-7.0\ \%}$	${}^{+12.0\ \%}_{-8.8\ \%}$

Table 5.2: Summary of the contributions to the systematic error for the J/ψ and $\gamma\gamma$ cross section measurement for electrons (muons). The error for the J/ψ signal extraction includes the systematic error in the fit of the invariant mass spectrum and the systematic errors on f_D and f_I (f_C) [20].

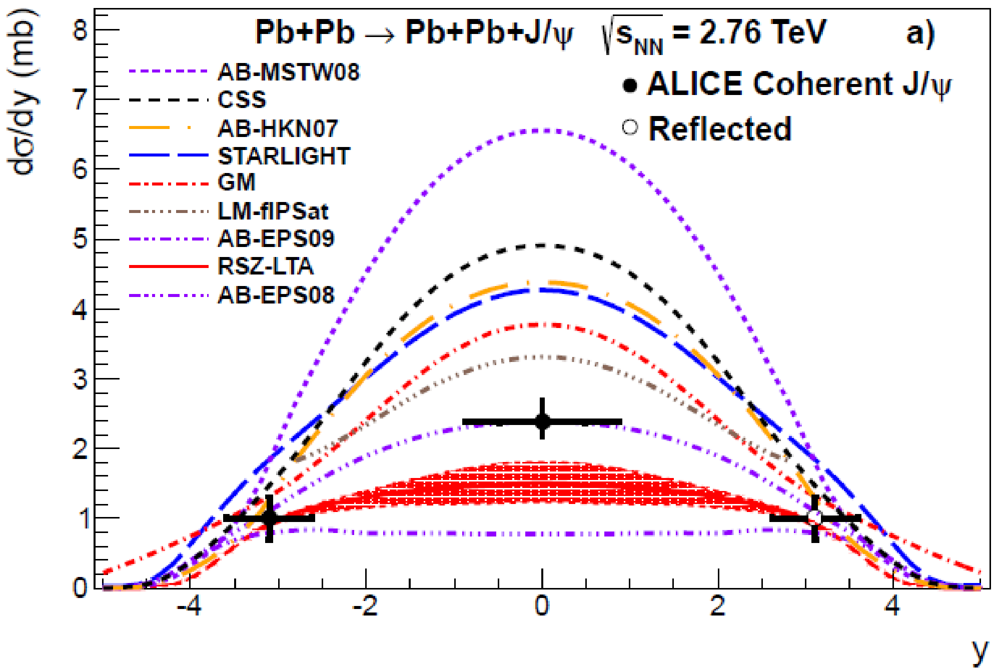

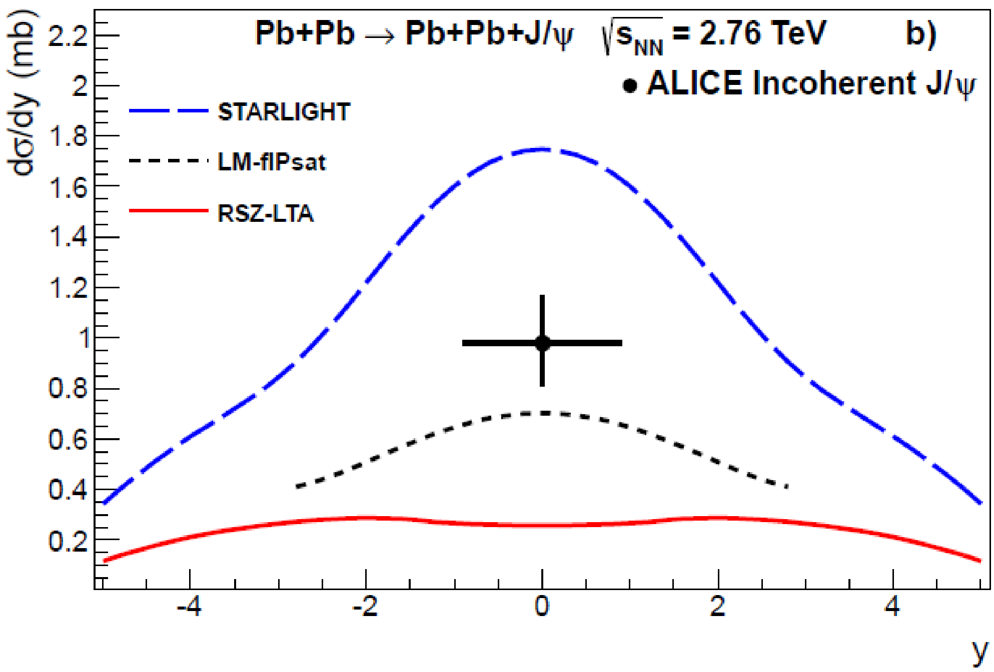

Figure 5.4: Measured differential cross section of J/ψ photoproduction in ultra-peripheral Pb-Pb collisions at $\sqrt{s_{NN}} = 2.76$ TeV at $-0.9 < y < 0.9$ for coherent a) and incoherent b) events. The error is the quadratic sum of the statistical and systematic errors. The theoretical calculations are also shown [20].

Chapter 6

Data analysis

The main focus of the experimental part of this thesis is to compare the performance of two models used for the signal extraction from the J/ψ invariant mass spectrum. After few definitions of basic statistical quantities at the beginning of the chapter, the results of testing the performance of both models on real and Monte Carlo data are presented.

6.1 Statistics

6.1.1 Expected value

The expected value of a random variable can be defined by the law of large numbers as the value to which the arithmetic mean converges after an infinite number of repetitions.

In other words, the expected value of a discrete random variable X can be defined as the probability-weighted average of all possible values

$$E[X] = \frac{\sum_i x_i p_i}{\sum_i p_i} = \sum_i x_i p_i, \tag{6.1}$$

where x_i are possible values of the random variable X and p_i are their associated probabilities. The sum of all the individual probabilities is equal to one.

For a continuous random variable X the expected value is defined as

$$E[X] = \int_{-\infty}^{\infty} x f(x)\,\mathrm{d}x, \tag{6.2}$$

where $f(x)$ is the probability density function (PDF). The expected value is also called the mean value or the mean.

6.1.2 Variance

The variance of a random variable X is the expected value of the squared deviation from the expected value of X

$$\mathrm{var}(X) = E[(X - E[X])^2]. \tag{6.3}$$

The standard deviation σ is computed from the variance as

$$\sigma_X = \sqrt{\mathrm{var}(X)}. \tag{6.4}$$

6.1.3 Covariance

The covariance of two random variables X and Y determines how much are they interdependent. It is defined as the expected value of the product of their deviations from their expected values

$$\mathrm{cov}(X,Y) = E[(X - E[X])(Y - E[Y])]. \tag{6.5}$$

When two random variables are independent, their covariance is zero. Covariance of a random variable X with itself is its variance

$$\mathrm{var}(X) = \mathrm{cov}(X,X). \tag{6.6}$$

The covariances of a set of random variables can be arranged into a covariance matrix, which is symmetrical. The i, j element of the covariance matrix is the covariance of the i^{th} and j^{th} variable.

6.1.4 Correlation

The correlation coefficient determines how much are two random variables linearly dependent. It is defined as

$$\mathrm{corr}(X,Y) = \frac{\mathrm{cov}(X,Y)}{\sigma_X \sigma_Y}. \tag{6.7}$$

As with the covariance, two independent variables have zero correlation. Note, that a correlation equal to zero implies only zero linear dependence, the variables can still be dependent, but in a more complicated manner. Unlike the covariance, the correlation can only have values from minus one to plus one. This makes correlations much more easier to compare than covariances, and therefore more widely used. When the correlation of two variables is equal to ± 1, they are perfectly linearly dependent (with positive or negative coefficient). The correlation of a set of variables can also form a correlation matrix similar to the covariance matrix.

6.1.5 χ^2 test

The χ^2 test serves for verifying the correct determination of the mean value and variance of a set of random variables. For n independent normally distributed variables x_i the χ^2 test is defined as

$$\chi^2 = \sum_{i=1}^{n} \frac{x_i - \mu_i}{\sigma_i^2}, \tag{6.8}$$

where μ_i are the mean values of the variables x_i and σ_i are their variances (square of the standard deviation). When expecting random fluctuations of the x_i variables around their mean values μ_i, each member of the χ^2 sum will be close to unity and the whole sum will be equal to the number of variables n. Hence if the μ_i and σ_i values are determined correctly, the term χ^2/n should be equal to one.

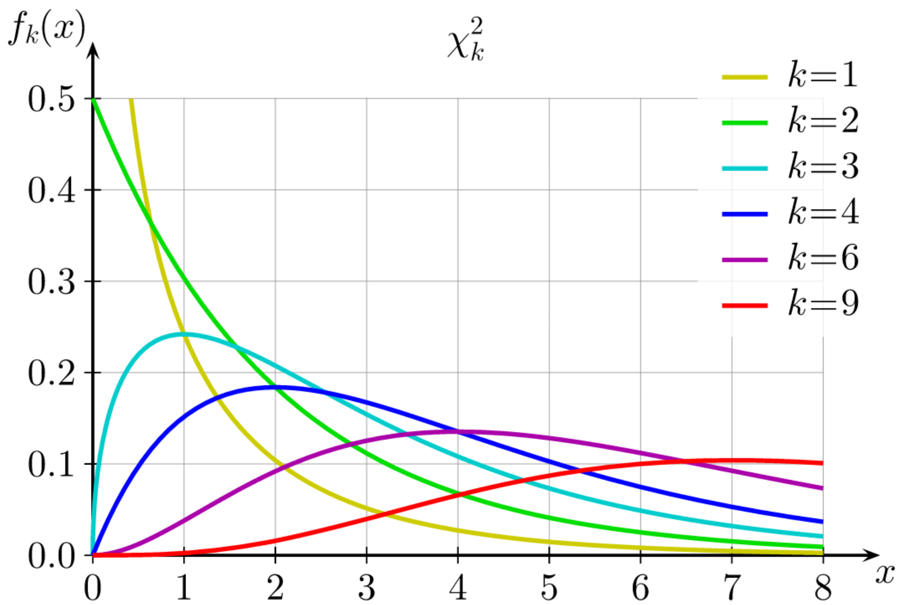

Figure 6.1: Graph of the χ^2 PDF with different number of degrees of freedom [21].

The χ^2 as defined above has the following probability density function

$$f_k(\chi^2) = \frac{1}{2^{k/2}\Gamma(k/2)} e^{-\chi^2/2} (\chi^2)^{k/2-1}, \tag{6.9}$$

where Γ is the gamma function and k is the number of degrees of freedom. When there are n measured variables, they are often somehow connected, therefore they are not truly independent. The number of degrees of freedom is equal to the number of variables minus the number of relations between them. A graph of the χ^2 PDF can be seen in Fig. 6.1. This PDF can be used to estimate that a measured value of χ^2 will be, with probability α, greater then $\chi^2_{k,\alpha}$, where $\chi^2_{k,\alpha}$ is defined as

$$\int_{\chi^2_{k,\alpha}}^{\infty} f(\chi^2)\,\mathrm{d}\chi^2 = \alpha. \tag{6.10}$$

6.2 Models for signal extraction

6.2.1 Crystal Ball model

The Crystal Ball function [22] is the most commonly used model to extract a signal from the J/ψ invariant mass distribution. The Crystal Ball function is composed of a Gaussian core with a power law and exponential tail, which is descried by the parameters α and n.

$$\begin{aligned} f(x;\alpha,n,\bar{x},\sigma) &= e^{-\frac{1}{2}\left(\frac{x-\bar{x}}{\sigma}\right)^2} && \text{for} \quad \frac{x-\bar{x}}{\sigma} > -\alpha \\ &= \left(\frac{n}{|\alpha|}\right)^n e^{-\frac{|\alpha|^2}{2}} \left(\frac{n}{|\alpha|} - |\alpha| - \frac{x-\bar{x}}{\sigma}\right)^{-n} && \text{for} \quad \frac{x-\bar{x}}{\sigma} \leq -\alpha \end{aligned} \tag{6.11}$$

The disadvantage of this model is the fact, that it contains terms involving a parameter to the power of a parameter. These terms are hard to fit numerically.

6.2.2 GaussExp model

GaussExp [23] is a newly proposed function, which is allegedly more appropriate to describe the J/ψ invariant mass peak. The GaussExp function is composed of a Gaussian core with an exponential tail, which is described by only one parameter k.

$$\begin{aligned} f(x;k,\bar{x},\sigma) &= e^{-\frac{1}{2}\left(\frac{x-\bar{x}}{\sigma}\right)^2} && \text{for} \quad \frac{x-\bar{x}}{\sigma} \geq -k \\ &= e^{\frac{k^2}{2}+k\left(\frac{x-\bar{x}}{\sigma}\right)} && \text{for} \quad \frac{x-\bar{x}}{\sigma} < -k \end{aligned} \tag{6.12}$$

This model is more simple and does not contain any of the undesirable terms.

6.3 Background model

To describe the dimuon continuum from the two-photon interactions in the forward-rapidity region, present in the invariant mass distribution for UPC, the following function was used [24].

$$\begin{aligned} f(x;\lambda,t,a_1,a_2,a_3) &= e^{\lambda x}[1+a_1(x-t)^2+a_2(x-t)^3+a_3(x-t)^4] \qquad &\text{for} \quad x \leq t \\ &= e^{\lambda x} \qquad &\text{for} \quad x > t \end{aligned} \tag{6.13}$$

This function is an exponential multiplied by a fourth order polynomial and from a given threshold smoothly continues as a simple exponential. Based on [24] the threshold was chosen to be $t = 4$ GeV/c^2.

6.4 Data

The presented analysis was performed on both Monte Carlo and real data.

The simulated data were Monte Carlo generated events of coherent J/ψ photoproduction and two-photon events creating a dimuon continuum as the background process. Diagrams for both of these processes can be seen in Fig. 3.3 and Fig. 3.4. The ALICE detector response was then simulated. The Monte Carlo data allow to benchmark the performance of both models by comparing the input values with the results obtained from signal extraction.

The real data were measured in Run 2 Pb-Pb ultra-peripheral collisions at $\sqrt{s_{NN}} = 5.02$ TeV with the ALICE muon spectrometer.

6.5 Results

All data analysis presented in this chapter was performed within the ROOT data analysis framework. The values of χ^2, the number of J/ψs (for the MC events compared with the input values), the fit errors and the correlation matrices were used to compare the performance of both models.

The number of entries for MC data, the fit range and the bin size for all data was selected the same as in [24], so that the results can be easily compared. A $p_t < 0.25$ GeV/c cut was applied to all data to suppress background effects. The mean value denoted $\bar{x}$ in Sec. 6.5.3 is denoted m_0 in this section, as its value is supposed to be the J/ψ invariant mass.

6.5.1 Pure background MC data

The dimuon continuum background MC data are fitted with the model from Eq. 6.13. In addition a scaling parameter N_{bck} is added before the model. The resulting fit, together with the correlation matrix, can be seen in Fig. 6.2.

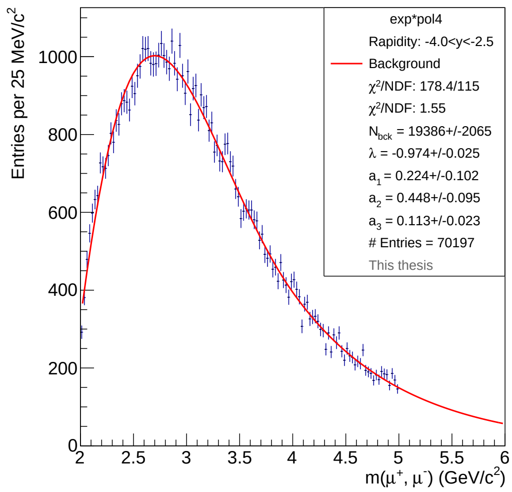

(a) Fit of simulated data.

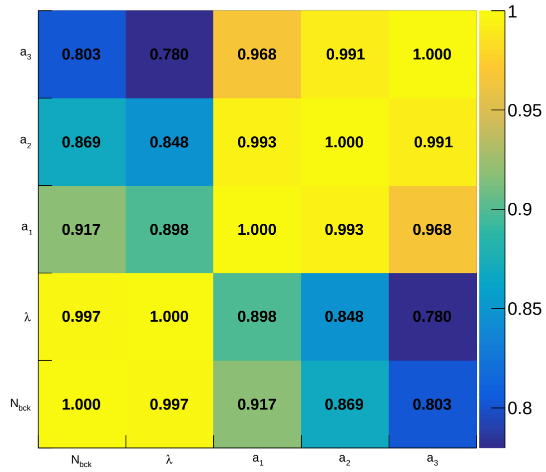

(b) Correlation matrix.

Figure 6.2: Fit results and correlation matrix for pure dimuon continuum MC data fit with the background model.

The correlation matrix shows a strong correlation between all parameters of the background model. The correlation is extremely strong between the normalizing parameter N_{bck} and the exponential parameter λ. It is also very strong between the a parameters.

The fit itself optically seems to be describing the background quite well, but the χ^2 value is not optimal. The obtained values of the fit parameters are important, because they are later used to fix the background in the signal extraction from real data. The fit parameter values are compatible with those in [24].

6.5.2 Pure J/ψ signal MC data

In this section the fit results for pure J/ψ signal, generated by the Monte Carlo, are presented. The results from the fits are later used in Sec. 6.5.3 and Sec. 6.5.4 to extract the signal from the invariant mass spectrum.

Crystal Ball

The fit of the pure J/ψ signal MC data with the Crystal Ball model and an additional scaling constant N_{cb}, together with the correlation matrix, can be seen in Fig. 6.3.

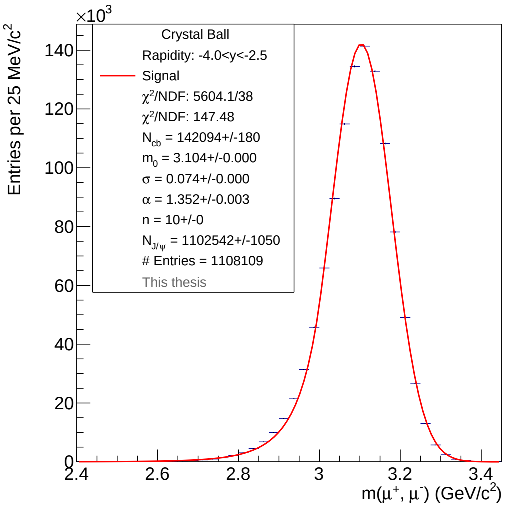

(a) Fit of simulated data.

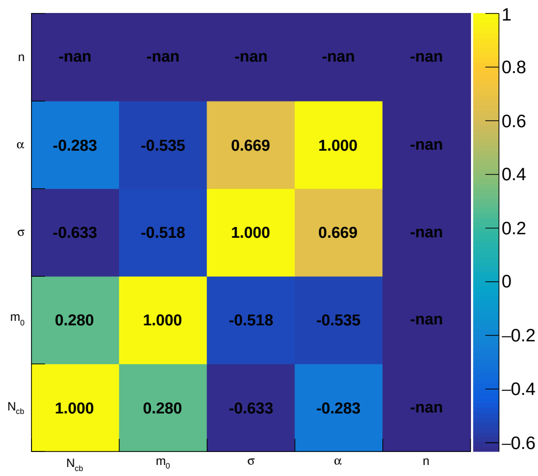

(b) Correlation matrix.

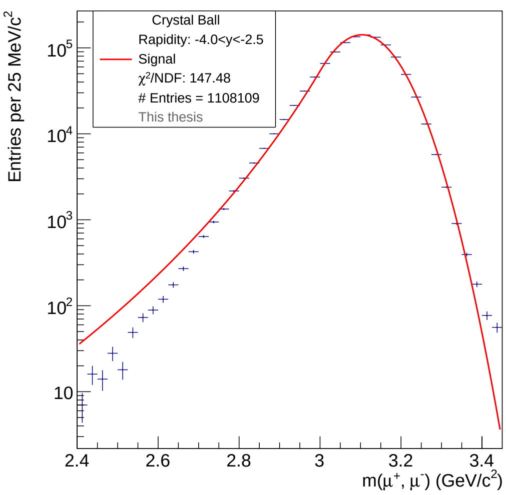

(c) Fit of simulated data with log scale.

Figure 6.3: Fit results and correlation matrix for pure J/ψ signal MC data fit with the Crystal Ball model. The n parameter is fixed to 10. The number of entries is $\approx 10^6$.

Even though the fit with linear scale seems to be fine, with logarithmic scale the fit is clearly not describing the data correctly. The χ^2 value is also extremely bad and the calculated number of J/ψs is off by almost 6 σ. The $\alpha = 1.352 \pm 0.003$ parameter is not consistent with the results in [24], where $\alpha = 1.301 \pm 0.003$. The n parameter was fixed

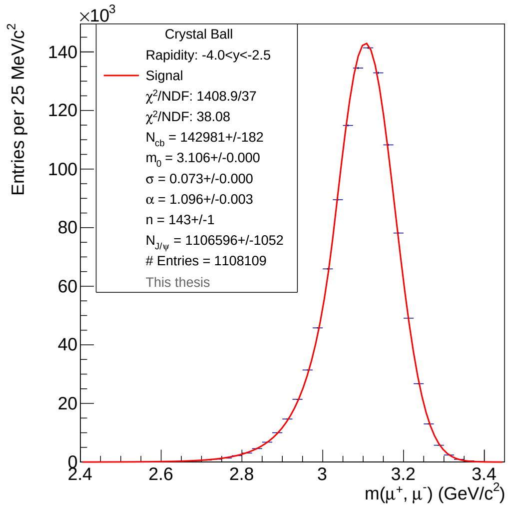

(a) Fit of simulated data.

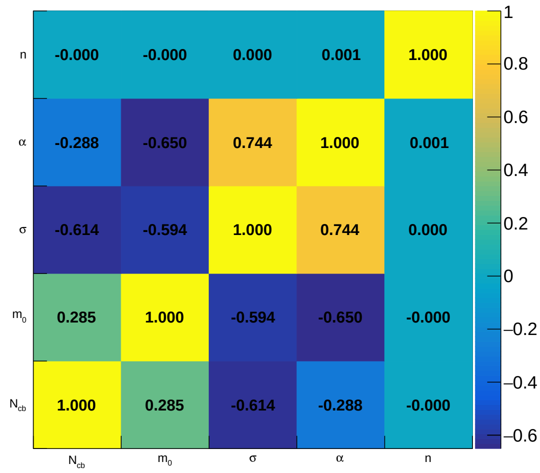

(b) Correlation matrix.

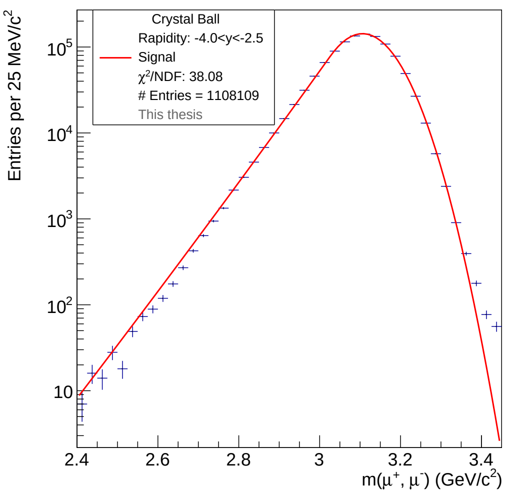

(c) Fit of simulated data with log scale.

Figure 6.4: Fit results and correlation matrix for pure J/ψ signal MC data fit with the Crystal Ball model.The n parameter is limited from above by 143. The number of entries is $\approx 10^6$.

to value 10, same as in the [24] paper, to have the same conditions. When the n parameter was left free, the fit is very unstable. For the same amount of entries as in the previous fit (same as in [24]) and with no limitations on the n parameter, the fit does not converge. When an upper limit is set for the n parameter, the fit always converges with the upper limit as the value of the n parameter. The highest possible limit, before the fit does not converge, is 143. Results of such fit can be seen in Fig. 6.4.

From the graph with logarithmic scale can be seen that the fit describes the data better now. The χ^2 value is better, but still very high. Also the number of J/ψs is closer to the correct value, but still off by almost 2 σ. The correlation matrix shows almost zero correlation of all parameters with the n parameter, suggesting it has no effect on the model.

The fit results are sensitive to the number of entries, which influences the relative precision of the fitted data points. When the number of entries is chosen significantly smaller (hence the error bars of the fitted data points are larger), the fit converges even without limitation for the n parameter Fig. 6.5.

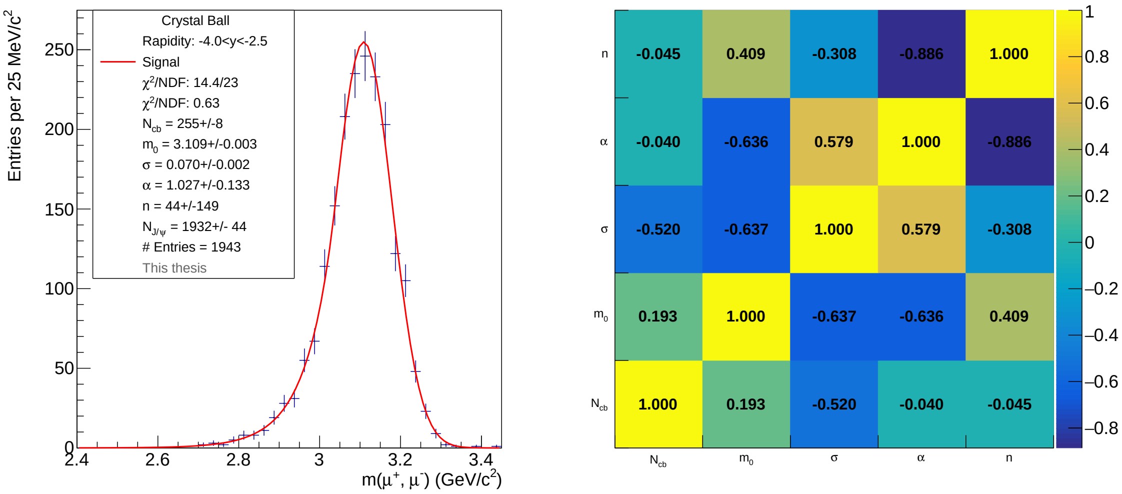

(a) Fit of simulated data.

(b) Correlation matrix.

Figure 6.5: Fit results and correlation matrix for pure J/ψ signal MC data fit with the Crystal Ball model. The n parameter is not limited. The number of entries is 1943.

The χ^2 value is very good and the calculated number of J/ψs is within 1 σ from the number of input entries. However, the parameter n has relative uncertainty over 300 % and is strongly anticorrelated with the α parameter, suggesting it might be unnecessary.

When a different low number of entries is chosen, the fit also converges without any limitations for n, but with different behavior in n. The results can be seen in Fig. 6.6.

Again the χ^2 value is good and the number of J/ψs is correct. But now, the relative uncertainty for the n parameter is significantly lower and it is strongly correlated with the α parameter.

For low values of entries (below 9000) it is also possible to get results where the fit does not converge, exactly the same as for the high amount of entries (10^6). Another possible results is that the fit converges, the value of the n parameter is close to 143 with less then 1 % error and it shows moderate correlation with all the other parameters.

However, for all the fits where the n parameter is not fixed to 10, the values of the α parameter are compatible with each other, but not with the one in [24]. The origin of the different results for low and high number of entries is the different size of error bars, the reason for the different behavior for low amount of entries is not fully understood.

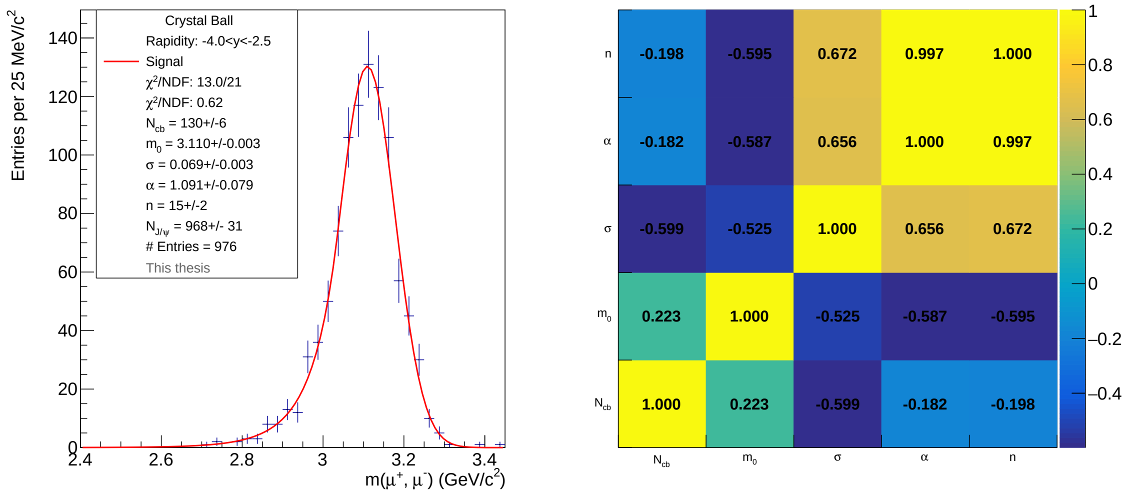

(a) Fit of simulated data.

(b) Correlation matrix.

Figure 6.6: Fit results and correlation matrix for pure J/ψ signal MC data fit with the Crystal Ball model. The n parameter is not limited. The number of entries is 976.

GaussExp

The fit of the pure J/ψ signal MC data with the GaussExp model and an additional scaling constant N_{ge}, together with the correlation matrix, can be seen in Fig. 6.7.

As with the Crystal Ball fit for high number of entries, the χ^2 value is high and the number of J/ψs is off by almost 2 σ. But the k parameter does not need any limits. The fit is stable and its behavior does not change significantly with the number of entries, therefore only one fit with lower number of entries is presented. The results are in Fig. 6.8. The fit has good χ^2 and the number of J/ψs is compatible with the input. Moreover, the value of the k parameter is compatible with that for high amount of entries.

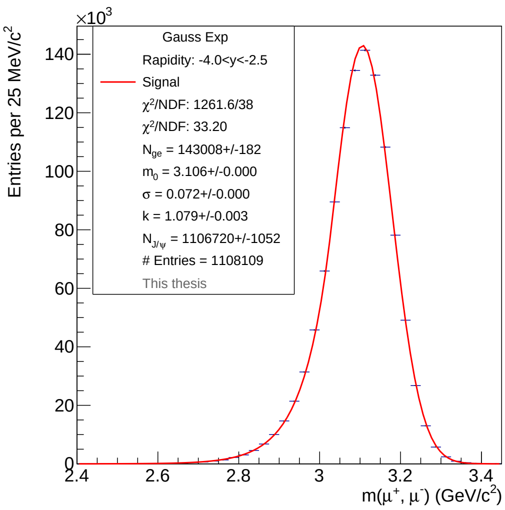

(a) Fit of simulated data.

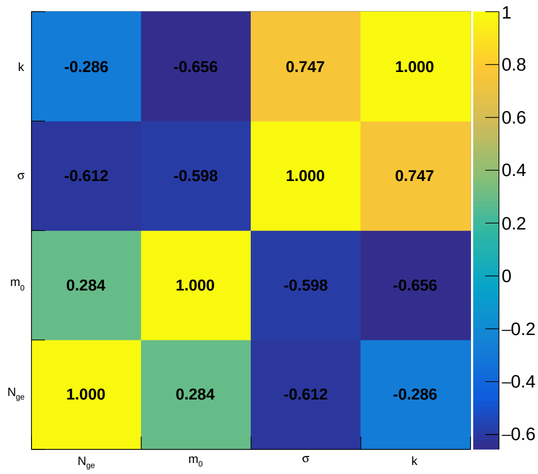

(b) Correlation matrix.

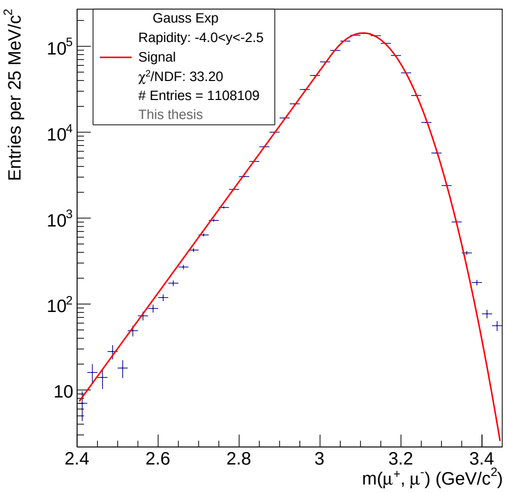

(c) Fit of simulated data with log scale.

Figure 6.7: Fit results and correlation matrix for pure J/ψ signal MC data fit with the GaussExp model. The k parameter is not limited. The number of entries is $\approx 10^6$.

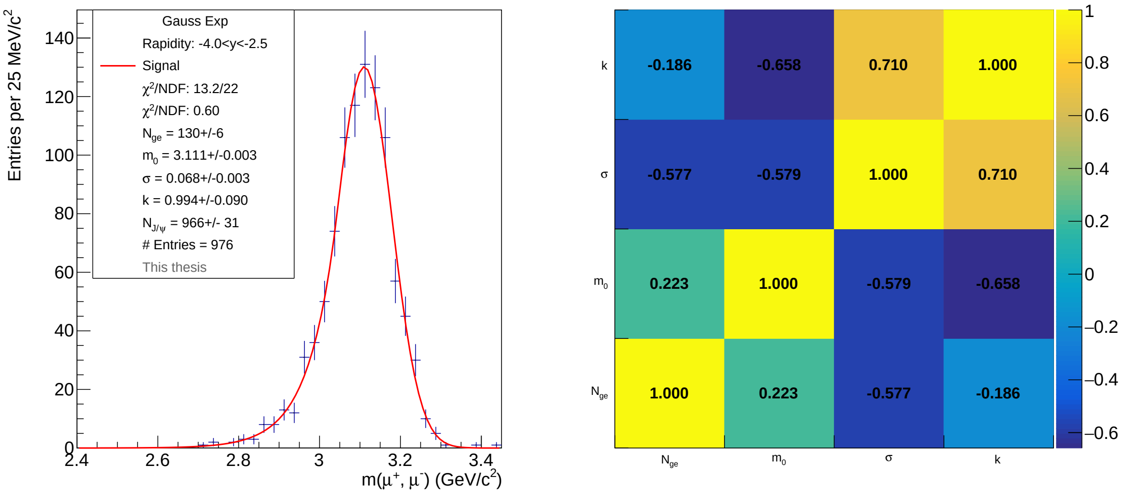

(a) Fit of simulated data. (b) Correlation matrix.

Figure 6.8: Fit results and correlation matrix for pure J/ψ signal MC data fit with the GaussExp model. The k parameter is not limited. The number of entries is 976.

6.5.3 Signal extraction from MC data

In this section both the pure J/ψ signal and the dimuon continuum MC data are combined and fitted with a combination of the signal extraction model and the background describing model. For each model a normalizing parameter is added. The values for the model parameters (both background and signal) are fixed to values obtained from previous MC fits. The only parameters left free are: m_0, σ, $N_{cb/ge}$, N_{bck}.

The number of entries for both background and signal was selected so that it is similar to the number of entries in the available real data.

Crystal Ball

The parameters for the background model were fixed to values from Fig. 6.2. The values of parameters for the Crystal Ball model together with the resulting χ^2 and $N_{\mathrm{J}/\psi}$ from the fit are summarized in Tab. 6.1.

Parameters in column a) are from Fig. 6.3, parameters in column b) are from Fig. 6.4, parameters in column c) are from Fig. 6.5, parameters in column d) are from Fig. 6.6 and parameters in column e) are from [24]. All the results for $N_{\mathrm{J}/\psi}$ are compatible with each other within 1 σ, but they are all more then one σ from the MC number of entries. The result in column c) has the best χ^2 value, but the $N_{\mathrm{J}/\psi}$ is more then 2 σ from the correct value. The best result for $N_{\mathrm{J}/\psi}$ has column a), but it has the worst χ^2 value. The fit with Crystal Ball parameters from column a) can be seen in Fig. 6.9.

	a)	b)	c)	d)	e)
α	1.352	1.096	1.027	1.091	1.3012
n	10	143	44	15	10
$N_{J/\psi}$	5057 ± 89	5084 ± 89	5122 ± 90	5130 ± 90	5073 ± 89
χ^2	1.41	1.24	1.21	1.23	1.36

Table 6.1: Fit results for combined signal and background MC data with the Crystal Ball model with different parameters α and n. The number of pure signal entries is 4936.

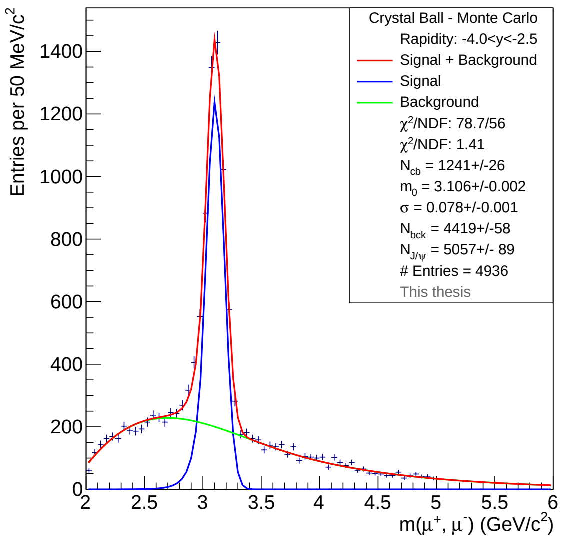

Figure 6.9: Fit of combined signal and background MC data with the Crystal Ball model. The Crystal Ball parameters are $\alpha = 1.352$ and $n = 10$. The number of J/ψ signal entries is 4936. The ratio of background to signal entries is 10 to 6.

Just by increasing the total number of entries, but with the same parameters as in Fig. 6.9 and with the same ratio of signal and background entries, the fit provides the correct number of J/ψs. The associated χ^2 is 1.67 and the fit can be seen in Fig. 6.10.

Results for fits where the α parameter of the Crystal Ball model and the λ parameter of the background model are left free can be seen in Fig. 6.11 and Fig. 6.12, for the lower and higher number of entries respectively. Values of the λ parameters are within one σ from the value predicted by the fit of pure background signal. Values of the α parameters are compatible with those obtained from pure signal fits where the n parameter was not fixed. Both fits have better value of χ^2, but they both provide worse estimation of the number of J/ψs than the fits with fixed parameters. Now even for the higher number of entries, the fit does not provide the number of J/ψs within one σ to the correct value.

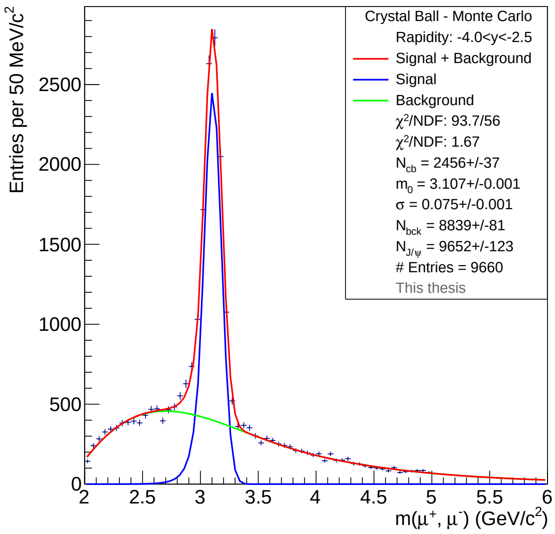

Figure 6.10: Fit of combined signal and background MC data with the Crystal Ball model. The Crystal Ball parameters are $\alpha = 1.352$ and $n = 10$. The number of J/ψ signal entries is 9660. The ratio of background to signal entries is 10 to 6.

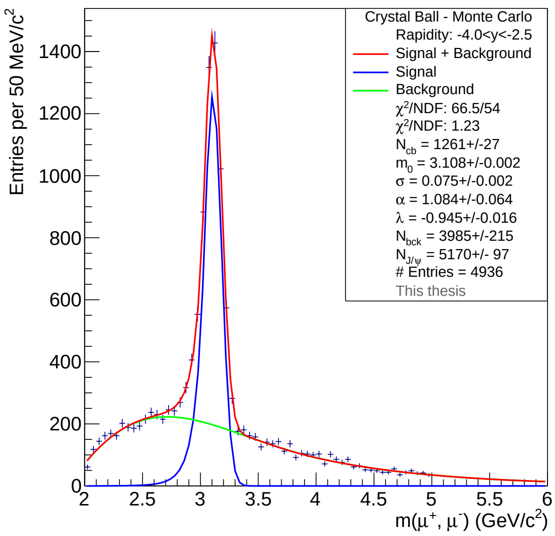

Figure 6.11: Fit of combined signal and background MC data with the Crystal Ball model. The Crystal Ball parameter $n = 10$, the α parameter and the background model parameter λ are left free. The number of J/ψ signal entries is 4936. The ratio of background to signal entries is 10 to 6.

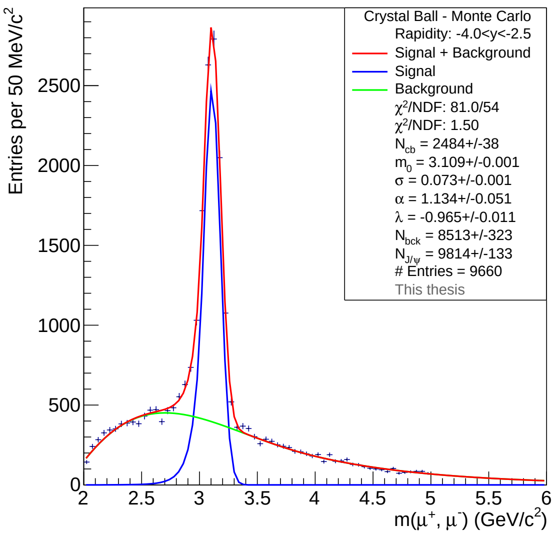

Figure 6.12: Fit of combined signal and background MC data with the Crystal Ball model. The Crystal Ball parameter $n = 10$, the α parameter and the background model parameter λ are left free. The number of J/ψ signal entries is 9660. The ratio of background to signal entries is 10 to 6.

GaussExp

The parameters for the background model were again fixed to values from Fig. 6.2. The results for the GaussExp model parameters (both from Fig. 6.7 and Fig. 6.8) were almost identical. Only the results for the parameter from Fig. 6.7 ($k = 1.079$) are presented. The fit for lower number of entries (similar to that in real data) is in Fig. 6.13.

As with the results for the Crystal Ball model, the number of J/ψs is off by more then one σ. The χ^2 value is similar to the Crystal Ball results which had good χ^2 value, but worse estimated number of J/ψs.

The results for the higher number of entries is in Fig. 6.14. The number of J/ψs is worse then the one predicted by the Crystal Ball model but still within one σ from the correct value. The χ^2 is better for the GaussExp model.

Results for fits where the k parameter of the GaussExp model and the λ parameter of the background model are left free can be seen in Fig. 6.15 and Fig. 6.16, for the lower and higher number of entries respectively. Values of the λ parameters are again within one σ from the value predicted by the fit of pure background signal. Values of the k parameters are compatible with all those previously obtained. For the lower number of entries within 1.5 σ, for the higher number of entries within 1 σ. Both fits have again better value of χ^2, but they both provide worse estimation of the number of J/ψs than the fits with fixed parameters. However, unlike the Crystal Ball model, the GussExp model still provides the correct number of J/ψs even for the higher number of entries.

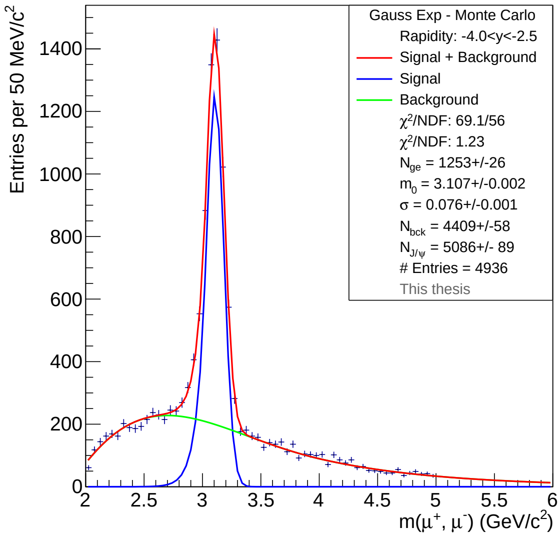

Figure 6.13: Fit of combined signal and background MC data with the GaussExp model. The GaussExp parameter is $k = 1.079$. The number of J/ψ signal entries is 4936. The ratio of background to signal entries is 10 to 6.

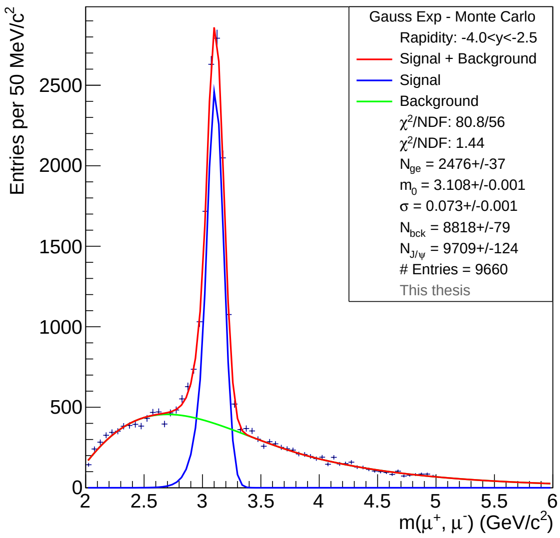

Figure 6.14: Fit of combined signal and background MC data with the GaussExp model. The GaussExp parameter is $k = 1.079$. The number of J/ψ signal entries is 9660. The ratio of background to signal entries is 10 to 6.

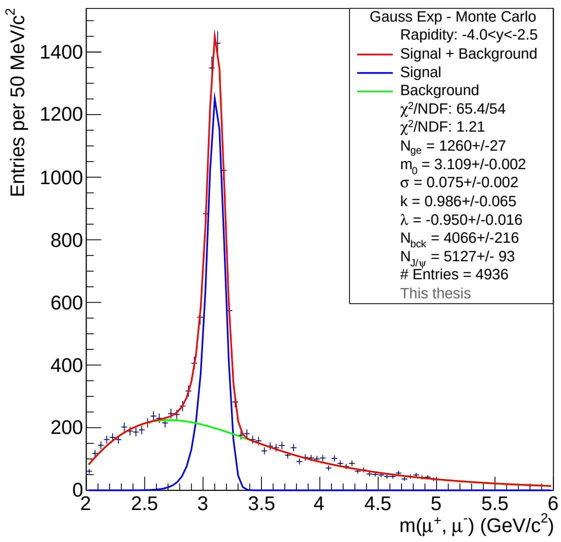

Figure 6.15: Fit of combined signal and background MC data with the GaussExp model. The GaussExp parameter k and the background model λ are left free. The number of J/ψ signal entries is 4936. The ratio of background to signal entries is 10 to 6.

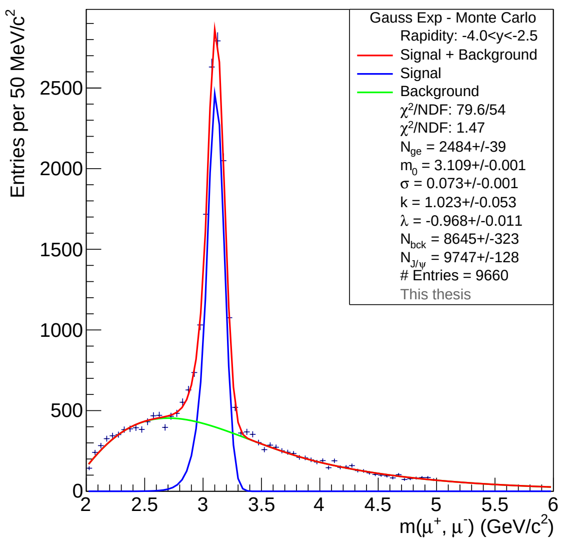

Figure 6.16: Fit of combined signal and background MC data with the GaussExp model. The GaussExp parameter k and the background model λ are left free. The number of J/ψ signal entries is 9660. The ratio of background to signal entries is 10 to 6.

It is worth mentioning, that all fits on Monte Carlo data produce slightly higher invariant mass of the J/ψ than is the PDG value $m_0 = 3096.900 \pm 0.006$ MeV [2].

6.5.4 Signal extraction from real data

Results of the signal extraction from Pb-Pb ultra-peripheral collisions at $\sqrt{s_{NN}} = 5.02$ TeV are presented in this section.

Crystal Ball

The results for the Crystal Ball model are in Fig. 6.17. The χ^2 value is 2.02, which is almost twice as much as in [24]. The $N_{\mathrm{J}/\psi}$ is however within one σ to the value stated in [24].

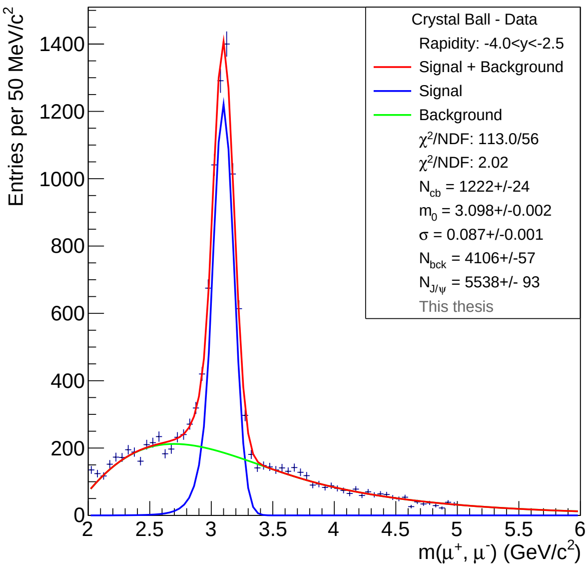

Figure 6.17: Fit of dimuon invariant mass distribution from Pb-Pb UPC at $\sqrt{s_{NN}} = 5.02$ TeV with the Crystal Ball model. The Crystal Ball parameters are $\alpha = 1.352$ and $n = 10$.

GaussExp

The results for the GaussExp model are in Fig. 6.18. The χ^2 value is 1.99, which is almost twice as much as in [24]. The $N_{\mathrm{J}/\psi}$ is however within one σ to the value stated in [24]. The results for the GaussExp model are compatible with those for the Crystal Ball model.

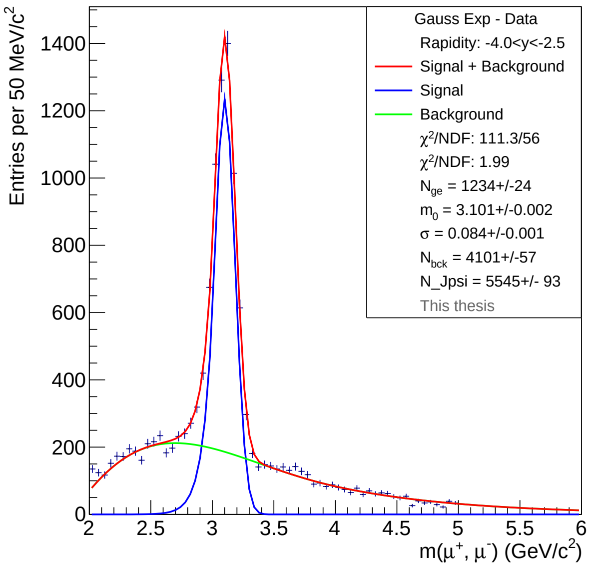

Figure 6.18: Fit of dimuon invariant mass distribution from Pb-Pb UPC at $\sqrt{s_{NN}} =$ 5.02 TeV with the GaussExp model. The GaussExp parameter is $k = 1.079$.

6.5.5 Sensitivity of the signal extraction results to variation of the fit parameters

In this section the fit results for both models are carried out with their parameters varying by one σ. This procedure can be used to estimate the systematic error of the signal extraction.

Background

In Tab. 6.2 are fit results for the background model with parameter values taken from Fig. 6.2. The used signal extraction model is the Crystal Ball model with parameter values taken from Fig. 6.3. Only the λ parameter is varied. The change in the number of J/ψs is only 0.1 σ. The χ^2 changes by 0.14.

Variation of the λ parameter has to be taken with care, because all the parameters in the background model are strongly correlated.

Crystal Ball

In Tab. 6.3 are fit results for the Crystal Ball model with parameter values taken from Fig. 6.3. Only the parameter α is varied, because the n parameter is fixed. The variation is only small in this case, therefore the effects on the number of J/ψs and χ^2 are negligible.

	lower	mid	upper
λ	-0.999	-0.974	-0.949
$N_{J/\psi}$	5054 ± 89	5057 ± 89	5063 ± 89
χ^2	1.52	1.41	1.38

Table 6.2: Fit results for combined signal and background MC data with the Crystal Ball parameters $\alpha = 1.352$ and $n = 10$. The background model has different parameters λ. The parameters are varied by one σ. The number of pure signal entries is 4936.

	lower	mid	upper
α	1.349	1.352	1.355
n	10	10	10
$N_{J/\psi}$	5058 ± 89	5057 ± 89	5056 ± 89
χ^2	1.40	1.41	1.41

Table 6.3: Fit results for combined signal and background MC data with the Crystal Ball model with different parameters α and n. The parameters are varied by one σ. The number of pure signal entries is 4936.

In Tab. 6.4 are fit results for parameter values taken from Fig. 6.6. Both parameters α and n are varied, but only one at a time. Because the σ is larger then in the previous case, the variation of the parameters has more significant results. The maximum difference in the number of J/ψs due to variation of the α parameter is approximately 0.7 σ. The maximum difference in the number of J/ψs due to variation of the n parameter is approximately 0.15 σ. The values of χ^2 are almost the same.

	lower	mid	upper	lower	mid	upper
α	1.012	1.091	1.170	1.091	1.091	1.091
n	15	15	15	13	15	17
$N_{J/\psi}$	5163 ± 90	5130 ± 90	5096 ± 90	5138 ± 91	5130 ± 90	5124 ± 89
χ^2	1.24	1.23	1.27	1.23	1.23	1.23

Table 6.4: Fit results for combined signal and background MC data with the Crystal Ball model with different parameters α and n. The parameters are varied by one σ. The number of pure signal entries is 4936.

GaussExp

In Tab. 6.5 are fit results for the GaussExp model with parameter values taken from Fig. 6.7 (left) and Fig. 6.8 (right). Variation in the left part is for data with small σ, and therefore change in both $N_{J/\psi}$ and χ^2 is negligible. The σ value is larger for the right part of the table and therefore the variation of the $N_{J/\psi}$ is approximately 0.7 σ. The variation in χ^2 is still small.

	lower	mid	upper	lower	mid	upper
k	1.076	1.079	1.082	0.904	0.994	1.084
$N_{J/\psi}$	5087 ± 89	5086 ± 89	5085 ± 89	5144 ± 91	5117 ± 90	5084 ± 89
χ^2	1.23	1.23	1.24	1.25	1.21	1.24

Table 6.5: Fit results for combined signal and background MC data with the GaussExp model with different parameters k. The parameters are varied by one σ. The number of pure signal entries is 4936.

Summary

The theoretical part of this thesis starts with a short introduction into particle physics and quantum chromodynamics, with focus on gluon saturation and nuclear shadowing. Afterwards, ultra-peripheral collisions (UPC) are introduced as a powerful tool to explore the gluon saturation. The ALICE experiment at the CERN LHC allowing the UPC measurement to be done is introduced in the following chapter. In the next chapter some of the previous UPC measurements made on ALICE are summarized.

The main aim of the experimental part of this thesis was to test the performance of models used for signal extraction of high energetic peaks in invariant mass distribution with radiation tails. The two tested models are a traditionally used Crystal Ball model and a newly proposed model called GaussExp. They were both tested on simulated Monte Carlo data of coherent J/ψ photoproduction together with a dimuon continuum produced in two-photon interactions. The models were compared based on values of χ^2, the extracted number of J/ψs, the fit errors and the correlation matrices. Tests on pure signal data as well as combination of background and signal data are presented. The behavior of the models under different fitting circumstances were studied.

Neither model describes the Monte Carlo shape when many events are considered. Therefore, in this case, the models would need to be improved. For statistics similar to that of real data both models have similar performance.

The fits of signal plus background Monte Carlo data systematically yield a larger number of J/ψs than the input value. Thus, it is important to be careful when studying real data. More studies are needed to see if such a bias is also present in real data.

The models were also tested on real data from Pb-Pb ultra-peripheral collisions at $\sqrt{s_{NN}} =$ 5.02 TeV measured with the ALICE muon spectrometer. The obtained results were compatible with results found in official ALICE analysis note [24].

The next steps will lead to inclusion of modified Crystal Ball and GaussExp models with radiation tails added also toward the higher end of the invariant mass spectra. Moreover, another model used within the ALICE collaboration will be implemented and its results compared with those obtained previously. Further studies of all models behavior will continue. In addition, a different fitting technique based on the maximum likelihood method, instead of the χ^2 method, will be tested.

Bibliography

[1] Wikipedia. Standard model, 2017. [Online; accessed 20-February-2017], Available at: `https://en.wikipedia.org/w/index.php?title=Standard_Model&oldid=764684583`.

[2] K. A. Olive et al. Review of Particle Physics. *Chin. Phys.*, C38:090001, 2014.

[3] A. Airapetian et al. Quark helicity distributions in the nucleon for up, down, and strange quarks from semi-inclusive deep-inelastic scattering. *Phys. Rev.*, D71: 012003, 2005.

[4] G.D. Coughlan and J.E. Dodd. *The ideas of particle physics and introduction for scientist*. Cambridge University Press, Trumpington Street, Cambridge CB2 1RP, 2 edition, 1991. ISBN 0521386772.

[5] Vardan Khachatryan et al. Constraints on parton distribution functions and extraction of the strong coupling constant from the inclusive jet cross section in pp collisions at $\sqrt{s} = 7$ TeV. *Eur. Phys. J.*, C75(6):288, 2015.

[6] S. Chekanov et al. A ZEUS next-to-leading-order QCD analysis of data on deep inelastic scattering. *Phys. Rev.*, D67:012007, 2003.

[7] H. Abramowicz et al. Combination of measurements of inclusive deep inelastic $e^{\pm}p$ scattering cross sections and QCD analysis of HERA data. *Eur. Phys. J.*, C75(12): 580, 2015.

[8] Nestor Armesto. Nuclear shadowing. *J. Phys.*, G32:R367–R394, 2006.

[9] A. Accardi et al. Electron Ion Collider: The Next QCD Frontier. *Eur. Phys. J.*, A52 (9):268, 2016.

[10] J. G. Contreras and J. D. Tapia Takaki. Ultra-peripheral heavy-ion collisions at the LHC. *Int. J. Mod. Phys.*, A30:1542012, 2015.

[11] David Horák. Exclusive production of rho in p-pb ultra-peripheral collisions. Master's thesis, Czech Technical University in Prague - Faculty of Nuclear Sciences and Physical Engineering, 2015.

[12] Jaroslav Adam. *Photoproduction of* J/ψ *in ultra-peripheral p-PB and Pb-Pb collisions with the ALICE detector at the LHC.* PhD thesis, Czech Technical University in Prague - Faculty of Nuclear Sciences and Physical Engineering, 2016.

[13] K. Aamodt et al. The ALICE experiment at the CERN LHC. *JINST*, 3:S08002, 2008.

[14] G. Herrera Corral. Diffractive Physics with ALICE at the LHC: the control of quantum collisions. *J. Phys. Conf. Ser.*, 624(1):012008, 2015.

[15] BIG SCIENCE CERN. The lhc in pictures, 2017. [Online; accessed 19-May-2017], Available at: `https://bigscience.web.cern.ch/bigscience/en/lhc/lhc2.html`.

[16] Arturo Tauro. ALICE Schematics. General Photo, [Online; accessed 29-June-2017], Available at: `http://cds.cern.ch/record/2263642`, May 2017.

[17] Betty Bezverkhny Abelev et al. Performance of the ALICE Experiment at the CERN LHC. *Int. J. Mod. Phys.*, A29:1430044, 2014.

[18] LHC MACHINE OUTREACH. Collisions, 2017. [Online; accessed 20-June-2017], Available at:
`https://lhc-machine-outreach.web.cern.ch/lhc-machine-outreach/collisions.htm`.

[19] Betty Abelev et al. Coherent J/ψ photoproduction in ultra-peripheral Pb-Pb collisions at $\sqrt{s_{NN}} = 2.76$ TeV. *Phys. Lett.*, B718:1273–1283, 2013.

[20] E. Abbas et al. Charmonium and e^+e^- pair photoproduction at mid-rapidity in ultra-peripheral Pb-Pb collisions at $\sqrt{s_{\mathrm{NN}}}$=2.76 TeV. *Eur. Phys. J.*, C73(11):2617, 2013.

[21] Wikipedia. Chi-squared distribution, 2017. [Online; accessed 26-June-2017], Available at:
`https://en.wikipedia.org/wiki/Chi-squared_distribution#/media/File:Chi-square_pdf.svg`.

[22] John Erthal Gaiser. *Charmonium Spectroscopy From Radiative Decays of the* J/ψ *and* ψ'. PhD thesis, SLAC, 1982. URL `http://www-public.slac.stanford.edu/sciDoc/docMeta.aspx?slacPubNumber=slac-r-255.html`.

[23] Souvik Das. A simple alternative to the Crystal Ball function. arXiv:1603.08591, 2016.

[24] E. Kryshen K. Graham, O.V. Baillie. Forward J/ψ photoproduction in ultra-peripheral Pb-Pb collisions at $\sqrt{s_{NN}} = 5.02$ TeV. February 2017. Draft of an ALICE analysis note.